ALMA MATER STUDIORUM - UNIVERSITÀ DI BOLOGNA

SCUOLA DI INGEGNERIA E ARCHITETTURA

DIPARTIMENTO di
INGEGNERIA DELL'ENERGIA ELETTRICA E DELL'INFORMAZIONE
"Guglielmo Marconi"
DEI

CORSO DI LAUREA MAGISTRALE IN TELECOMMUNICATIONS ENGINEERING

TESI DI LAUREA
in
Technologies and Applications of Wireless Power Transfer M

CHARACTERIZATION OF A 3D-PRINTED LOW-COST FLEXIBLE DIELECTRIC MATERIAL FOR THE REALIZATION OF INNOVATIVE WPT WEARABLE APPLICATIONS

CANDIDATO

Giulia Battistini

RELATORE

Chiar.ma Prof.ssa Alessandra Costanzo

CORRELATORI

Dott. Ing. Giacomo Paolini

Prof. Ing. Diego Masotti

Anno Accademico
2020/2021

Sessione *III*

SUMMARY

1. INTRODUCTION

Wireless and battery-free technologies are promising great advantages in the field of biomedical engineering for long term implantation and daily health monitoring, since they allow to realize lightweight, non-invasive, and millimeter-scale dimension devices. In particular, bio-integrated wearable sensors have recently become crucial for providing critical insights into the overall health status, to quantify human performance, and to establish a bi-directional communication between the sensors and external control machines [1].

The development of such novel sensing-monitoring devices, as will be here discussed, is strongly tied to the progress made in various emerging technologies such as biocompatible materials and flexible electronics, optical and electrochemical sensors, Wireless Power Transfer (WPT) both in Near Field (NF) and Far-Field (FF) communication systems and Energy Harvesting (EH) applications, big data and cloud computing [2].

One of the aims of wireless and battery-free technologies is to reduce as much as possible the use of wired cumbersome interfaces of sensors that couple to the skin via strap/tapes and that typically involve clinical experts. In fact, the most advanced interfaces used in neuroscience research and in medical systems still rely on physical tethers, such as electrical wires, optical-fiber cables or tubing, connecting the human body to an external supporting hardware able to record and collect the information [3]. However, such tether-based technologies face particular difficulties when interfacing those parts of the body which are highly mobile, since the forces exerted on the implant by the wires during natural motions, plugging and unplugging not only affect the accuracy of the measurement producing artifacts in the results, but also can cause soft tissue damage.

Moreover, these systems are bulky and generally cannot be used for long-term, continuous monitoring outside specialized facilities. This is the reason why wearable devices embedding miniaturized wireless electronic/sensing components intimately integrated with different curved surfaces of the body, not requiring wired, bulky hardware that, in many cases, significantly impede social behaviors, and natural movements, causing increased levels of anxiety and discomfort, have led to great social benefits, making the remote monitoring even in the healthcare sector possible and promoting a transformation of the sector from being hospital-centered to be personal, portable, and device-centered [2].

Even from the economical point of view, though these systems are typically narrow in scope and have, in most cases, low levels of clinical relevance/accuracy, the established commercial market for consumer health wearables is large and it is projected to grow in the following years, going in the direction of broad adoption especially for medical diagnostics and fitness monitoring. Actually, nowadays, several wearable sensors able to collect and communicate physiological indicators such as pulse rate, breath rate, respiration, temperature, activity monitoring, and able to recognize various biomarkers in human epidermis fluids, such as glucose, lactate, cholesterol etc., are already available on the market [4]. Some examples of bio-integrated wearable devices interfacing with the epidermis are shown in Fig. 1 (a-c), and some other wearable devices interfacing with other areas of the body are illustrated in Fig. 1 (d-f).

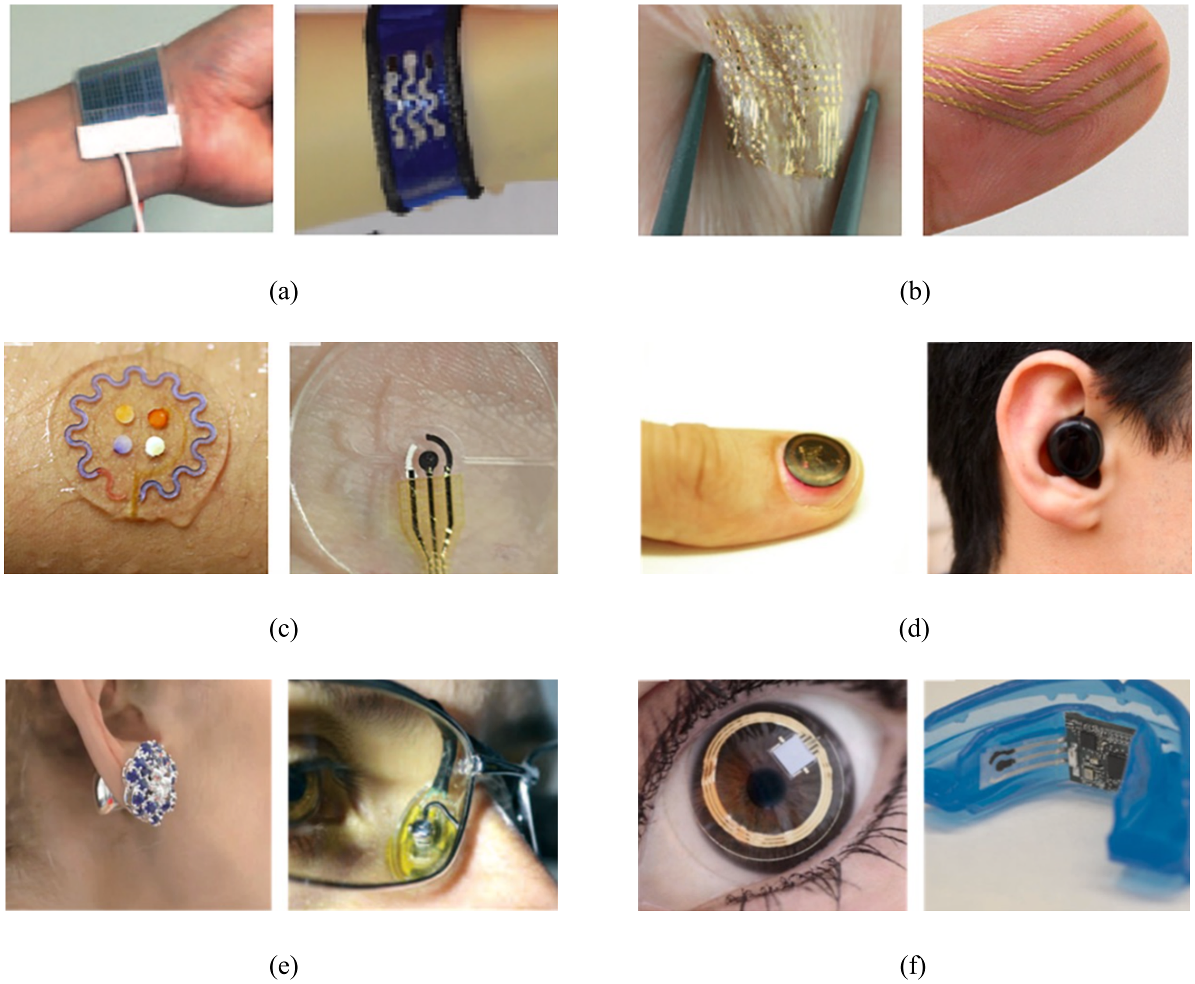
(a) (b) (c) (d) (e) (f)

Fig. 1. Pictures of different kind of bio-integrated wearable sensors commercially available on the market: (a) wearable sensors loosely interfaced to the skin on the wrist, (b) nano-mesh conductors that directly laminate onto the skin, (c) impermeable interfaces enabling the chemical monitoring and analysis of biofluids, (d) NFC enabled pulse oximeter devices mounted on a thumbnail and as ear-bud, (e) earring type pulse oximeter and eyeglasses with an integrated electrochemical sensor, (f) electrochemical biosensor in the form of contact lens or integrated on a mouthguard [1].

The integration of noninvasive wireless and battery-free sensors on the human body require, first of all, the selection of suitable flexible and irritation-free interfaces made of biocompatible materials able to adapt to the soft and curvilinear surfaces of human body while being robust during the natural movements. Thus, materials with mechanical properties close to those of tissue are desirable, namely elastic, highly breathable interfaces and robust to large strain deformations.

In particular when these materials are used for fabricating implantable devices such as neural implants, they must guarantee the safety of the subject from risks of tissue damage or allergic/toxic reactions over short (minutes to hours) or long-term (days to weeks) duration of continuous wear under different environmental conditions. At the moment, hermetic packages made of ceramics or titanium are state of the art to protect the implant electronics from moisture and ions but, being hard materials, forces due to movements can easily cause biological tissue damage [5].

Polymers have been found to be the most suitable material class when requirements such as little response to implantation, long-term stability in a hostile environment, high material flexibility and good electrical insulation of metallic conductors have to be combined in a single material.

A few examples of polymers frequently used in microelectronics for biomedical applications are hence briefly presented.

The Polyimide is generally used as insulation or passivation layer, providing protection for circuitry and metals from moisture absorption, corrosion, ion transport and physical damage, being characterized by high mechanical strength and superior chemical resistance. Also, processing polyimides is similar to conventional microelectronic processes, leading to low production costs and high repeatability.

The PDMS, commonly called "silicone", is the most widely used material for encapsulation and/or as substrate material in biomedical applications since 1970s. Among its properties there are physiological indifference, flexibility, excellent resistance to biodegradation and aging, high biocompatibility and permeability to gases and vapors. As substrate material, once the metal foil is placed on its surface, a second layer of PDMS is spin-coated on top and the overall structure can be etched by means of various manufacturing technologies.

On the other hand, Parylene C is the most widely adopted type of polymer as encapsulation material for biomedical microdevices but has resulted to be ill-suited as substrate for integrated microelectrodes due to not being sufficiently strong and robust. Recently, bilayers of parylene and PDMS have been used to encapsulate optogenetic stimulators because they can operate during immersion in physiological saline solution at 60° for at least 90 days without degradation in mechanical flexibility or functionality.

A last example is provided by Liquid Crystal Polymers (LCPs), which show high mechanical strength at high temperatures, extreme chemical resistance, low moisture absorption and permeability. Because of these excellent properties LCPs promise to become the new shooting stars in neural interfaces, but results from in vivo studies still have to be observed.

Furthermore, to boost the flexibility and stretchability of these structures, stretchable semiconductors are as well improving rapidly, particularly in Radiofrequency (RF) electronics, and are typically embedded into elastomeric layers [1]. This stretchability is made possible by means of the particular structural shape of the semiconductors: micro/nanofabrication processes define large-scale collections of semiconducting or conducting nanomembranes/ribbons/wires from the most sophisticated sources of thin-film or wafer-scale materials. In Fig. 2 are illustrated some examples of material engineering for stretchable electronics and bio-integrated wearable sensors, where the structural shapes can respond to applied strains through specific bending processes in a way that provides large levels of stretchability while avoiding significant strains in the active materials. For instance, the "wavy" ribbons/nanomembranes shown in Fig. 2 (a-d) when organized into a mesh-like architecture can create arc-shaped non coplanar configurations that increase the stretchability of the device of more than 100%, the Filamentary Serpentine (FS) structures similarly bonded to underlying elastomer substrates, Fig. 2 (e-f), exhibit considerable endurance to stress-strain curves matched to those of biological tissue (i.e., skin) and the repeated geometrical shapes create two-dimensional array structures that release in sequence as the applied strain increases. This same design strategy has been adopted in mechanically assembled 3D structures such as the helical coils shown in Fig. 2 (g-h) where the deformation-induced stress distributes uniformly along the structure avoiding the stress concentration at the arc regions of the corresponding 2D serpentine traces and, thus, enabling higher elastic stretchability. These conductor configurations can be used in structured antennas and interconnects to provide reliable operations for strains that exceed those set by natural biological motions.

An insight of the design architecture of a wireless battery-free wearable and flexible device such as the one depicted in Fig. 2 (h), able to monitor many different vital signals such as Electrocardiogram (ECG), Electromyogram (ECM), Electroencephalogram (EEC) and other measurements related to motion, is shown in Fig. 3, where the electrical components for wireless communication, recharging, and sensors are interconnected by means of 3D helical microstructures enabling the flexibility and stretchability of the device, then, the overall active and passive components and interconnections are encapsulated within two layers of elastomer [6].

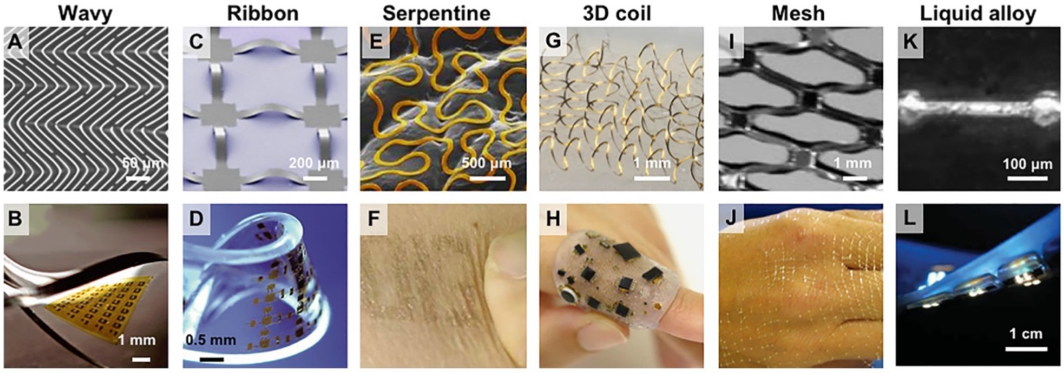

Fig. 2. Designs of materials enabling stretchability of conductors and semiconductors: (a) "wavy" Si ribbons/nanomembranes on PDMS, (b) twisted Si-CMOS circuit in a "Wavy" layout, (c) mesh geometry of stretchable silicon nanomembrane, (d) deformed complex structure, (e) serpentine metal traces on a skin replica, (f) skin-interfaced serpentine metal traces, (g) 3D helical coils bonded to a silicon substrate, (h) device deformed on a finger, (i) mesh-shape plastic film with organic transistors, (j) conductive network mounted on a hand, (k) microchannel filled with liquid metal alloy, (l) array of LEDs connected by liquid metal on deformable substrates [1].

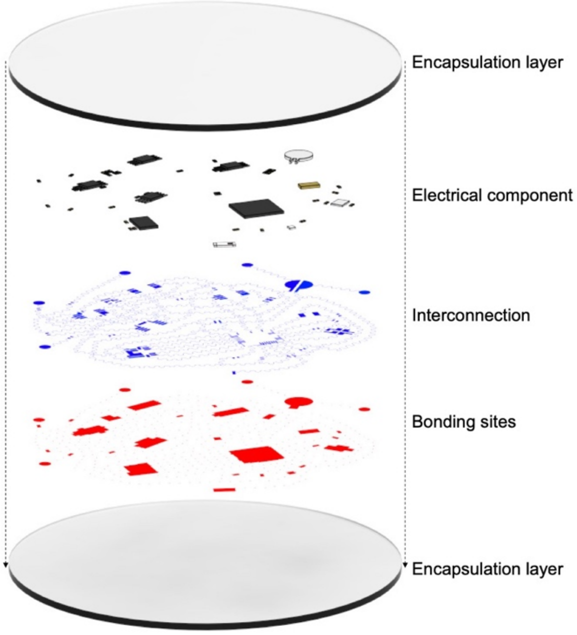

Fig. 3. Architectural structure of a wireless and battery-free wearable, flexible device for vital signals monitoring [6].

Furthermore, three-dimensional (3D) printing technology (also called "additive manufacturing") is an innovative manufacturing process enabling the rapid, cost effective and environmentally friendly large scale production of biocompatible, stretchable and flexible materials, which can be applied in a wide range of research areas [7].

In particular 3D printing technology is becoming increasingly attractive in the production of microwave devices and in the antennas design and fabrication, with the aim of making them lightweight, inexpensive, and easily integrable. The greatest advantage of printing technology with respect to standard microfabrication technologies is the lower number of fabrication steps and its bottom-up manufacturing approach, where the material is deposited layer by layer, thus, making additive manufacturing simple, environmental friendly (no material is wasted in the manufacturing process), and cost-efficient approach compared to conventional microfabrication techniques [4].

Fused Deposition Modelling (FDM) and Stereolithography Apparatus (SLA) methods are the most used 3D printing techniques for fabricating microwave devices. FDM creates three-dimensional structures by heating and extruding a thin filament of thermoplastic material such as Polylactic Acid (PLA), Acrylonitrile Butadiene Styrene (ABS), Polycarbonate (PC) and NinjaFlex, whereas SLA creates 3D structures with a liquid photopolymer resin that is cured and solidified by an ultraviolet laser.

The main drawback of these 3D-printed materials, as will be extensively discussed in this thesis, is their very high dielectric loss which strongly impairs the performances of the fabricated RF devices. For instance, in [7], the authors propose a 3D-printed Substrate Integrated Waveguide (SIW) realized in PLA where the substrate has been perforated in such a way to obtain a non-uniform honeycomb shape which allows to minimize the insertion losses caused by the dielectric properties of the 3D printing materials, while maintaining its mechanical strength. This means that the design freedom provided by 3D-printing technologies, where the desired 3D models are previously virtually designed by means of Computer-Aided Design (CAD) tools, allows to overcome the issue related to the typically high dielectric losses of the thermoplastic filaments or resin material.

Even specialty engineered materials companies such as Rogers Corporation and Fortify have recently announced a collaborative agreement culminated in a novel approach to produce Gradient Refractive Index (GRIN) dielectric lenses operating in the Ka-band providing better antenna gain/efficiency and wider beam-steering angle capabilities for electronically steerable antenna arrays [8]. In this case, the new Rogers Corp's ceramic-filled UV-curable polymer has been adopted, designed for use with photopolymer 3D-printing processes like SLA and Digital Light Processing (DLP) printing.

Another remarkable example of 3D printed wearable antenna meant to be exploited in the increasingly attractive field of massive Internet of Things (IoT) and Body Area Network (BAN) has been recently proposed in [9], where the authors realized a 3D printed antenna on a removable fingernail for on-body communications at microwave and millimeter waves, as shown in Fig. 4. In this case Aerosol Jet technology, a fine feature material deposition solution, has been used with nanoparticle conductive silver ink to directly print the microstrip patch antenna and the corresponding transmission line on an ABS removable fingernail substrate, using an Optomec machine. The antenna simulated and measured performances have been found to be in good agreement, showing a radiation efficiency of 80% on-body and 70% off-body.

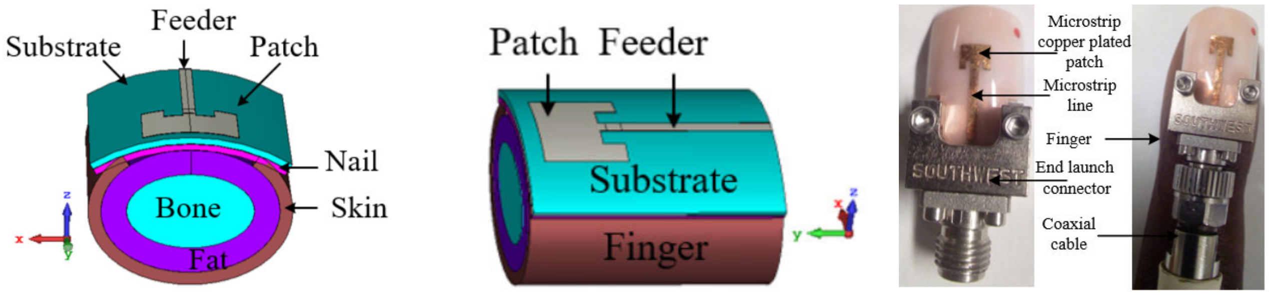

(a) (b) (c)

Fig. 4. (a) Cross and (b) longitudinal sections of the human finger model of the 3D printed antenna on a removable fingernail, and (c) realized antenna prototype [9].

As previously mentioned, the ever-increasing demand for thin, soft, lightweight construction in the types of skin-interfaced wearable systems also creates challenges and associated research opportunities, in power supply and in designs for power efficient operation [1].

In particular, energy storage systems, in the form of batteries and supercapacitors, comprise the majority of integrated power sources in bio-integrated sensors for wearable applications. However, batteries with sufficient storage capacity for many practical applications are space-consuming and heavy, typically occupying up to 90% of the volume of implantable devices and 60% of their weight [3]. Reducing the masses and sizes of the batteries, or completely eliminating them, provides significant advantages, especially for devices fabricated on thin polymeric substrates.

A first example of a stretchable lithium-ion battery for epidermal applications has been presented in [10] and exploits optimized microstructures and stretchable current collector architectures realized with the 2D serpentine-based traces abovementioned and illustrated in Fig. 2 (e), encapsulated on layers of silicon elastomer, as shown in Fig. 5.

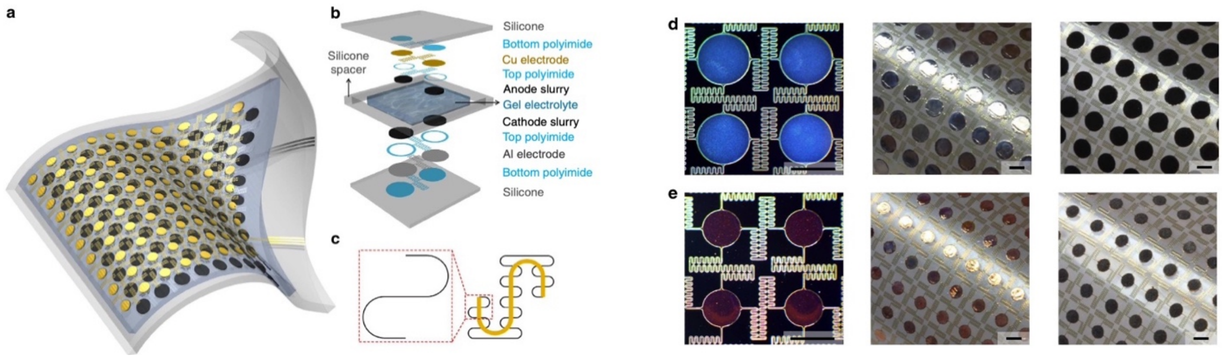

Fig. 5. (a) Stretchable batteries with serpentine interconnects, (b) exploded view of the layers of battery structure, (c) illustration of the serpentine geometry used for interconnects, (d) Al electrode pads and interconnects, (e) Cu electrode pads and interconnects [10].

Although lithium-based batteries are of widespread interest, they are not indicated for bio-integrated applications due to toxic components. Less toxic and environmentally friendly battery systems such as textile-based sodium batteries have been lately proposed exhibiting high flexibility, good rate capability, cycle stability and good integrability on necklaces, bracelets, or other types of skin-interfaced applications. Besides these inorganic materials systems, a kind of battery relying on enzymatic reactions to generate electricity also called “biobatteries” can be considered a further option in biocompatible power sources.

Alternatively, supercapacitors can provide numerous advantages over batteries, such as fast charging/ discharging, high power density and enhanced operational durability [1].

Conversely, in many practical cases such as implanted devices or in skin mounted systems where the process of establishing physical contacts can be mechanically destructive, the ability to charge the battery wirelessly can be valuable, especially because any other approach involving physical contact may cause electrical shock to surrounding materials. Moreover, wireless power transmission can enable devices with lightweight, miniaturized form factors and unlimited operational lifetimes.

Wireless power can be supplied from many different sources, as illustrated in Fig. 6. Obviously, the choice of power source must meet the system-dependent power-consumption requirements, for instance sensors power consumption typically ranges from 1 μW to 100 mW, which is much less than that of other consumer electronics such as smartphones. Among the different options there is the power that can be derived from internal biological sources (such as kinetic energy harvested from skeletal and visceral motions, chemical energy from bloody sugar and thermal energy from body heat), which provides typically very low output power and cannot be considered always reliable due to intermittency and physiological load of power derived from the biological processes, or external power sources such as RF radiation, magnetic resonant coupling, ultrasonic, photovoltaics, thermoelectrics, piezoelectrics, and triboelectrics [3]. The energy harvested by means of these different power sources is then rectified through a power conversion process which converts it into electric direct current (dc) voltage or current which may be stored or directly consumed by the attached load/application, Fig. 6 (b).

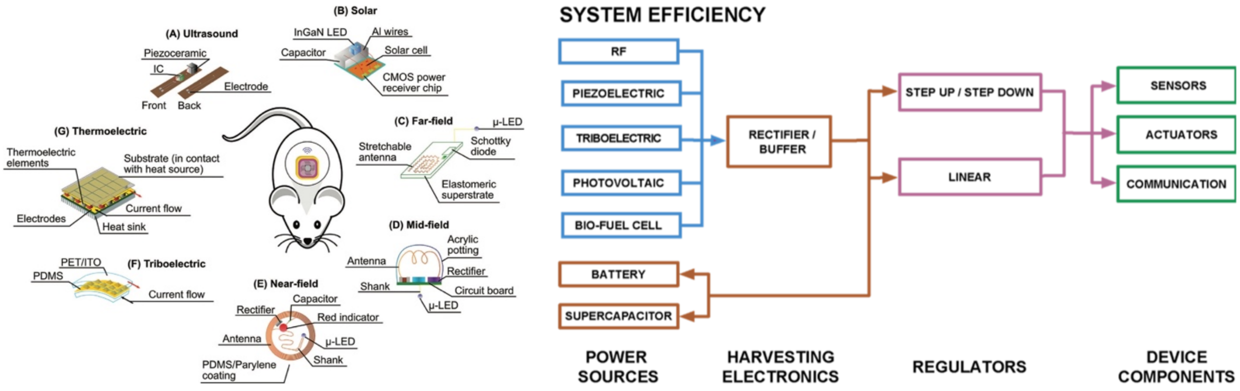

Fig. 6. (a) Different strategies for supplying power to wireless and battery-free implantable devices [11], and (b) rectification process to convert different types of harvested energy into dc power to activate IoT devices [1].

The great advantage of external power sources over internal biological sources is the fact that the device doesn’t need to establish a direct contact with the subject in order to provide a permanent reliable power supply for continuous vital signal monitoring or fully implantable systems. An estimate of the amount of available power provided by the abovementioned external power sources is here reported: ultrasonics may harvest ~0.1-0.2 mW, photovoltaics from 45 to 7 mW, whereas electromagnetic far-field radiation from 3 to 5 mW, and near to mid field and magnetic resonant coupling typically from 5 to 10 mW.

On the contrary, disadvantages of internal power harvesting, as stated, is mainly due to the intermittent nature of the latter, which provides limited amount of available power resulting to be insufficient for microcontrollers even when used together with capacitors or other energy storage components. In particular, the available power scavenged from biofuel cells is in the order of few µW and the peak power made available from triboelectric sources is in the order of 0.2-0.3 mW.

Just because of the significant amount of power that can be delivered by means of electromagnetic radiation and near-field coupling, RF WPT and EH are becoming the most versatile and scalable resources to operate bio-integrated and battery-free sensors, wearables, biomedical implants, Radiofrequency Identification (RFID) and so on. This is also possible thanks to the fact that ambient RF radiation is a ubiquitous power source in urban areas because of the dense deployment of Wi-Fi access points and cellular base stations [12].

Unlike passive EH, which exploits the environmental RF sources to avoid the use of batteries for remote ultra-low power wireless sensors and wearable devices, WPT technology is designed to be a stable and dedicated wireless power supply, meaning that the RF source is intended to provide a certain amount of power, at a specific known distance and position, with a known power intensity, polarization, and frequency. Thus, the receiving antenna will be straightforwardly designed according to this information in order to operate at a single frequency, with high directivity and being linearly polarized.

The design of the receiving antenna in an EH system is, instead, much more demanding, due to the fact that all the data related to the transmitting source, i.e., the frequency, the distance and direction of arrival, the power intensity and the field polarization, is not known, which means that the receiving antenna needs to be wideband/multiband, with low directivity and circularly polarized in order to be able to capture whatever kind of energy source present in the surrounding environment.
WPT can be classified in far-field and near-field power transmission, where the former makes use of radiating techniques, not requiring any interaction between the transmitting and receiving antennas, and the latter makes use of non-radiating techniques, such as inductive or capacitive coupling, which presupposes a strong interaction and coupling between transmitter and receiver. The distinction between FF and NF is defined by the distance between transmitter and receiver: if the distance is smaller or comparable to the wavelength of the EM wave, it is considered to be NF, otherwise if the distance is larger than the wavelength or if the source has an overall dimension or aperture which is larger than the wavelength, it is considered FF region (Fig. 7).

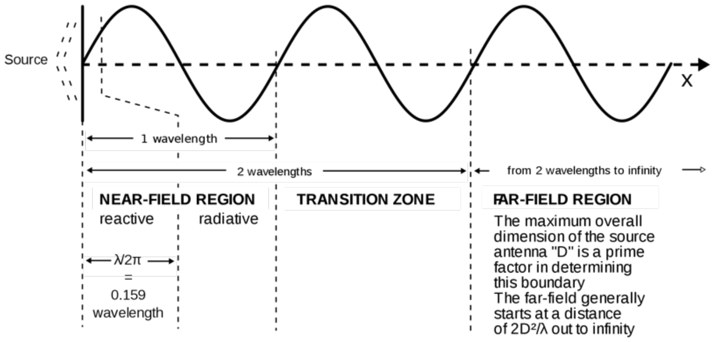

Fig. 7. Distinction between field regions for antennas: near-field and far-field regions [13].

Although WPT FF systems allow the transmission of power at high frequencies (at several hundred MHz or several GHz) over long distances, providing uniform and continuous power delivery from reduced size devices, it has the disadvantage of its strong dependance of the efficiency (often very low) on the angle between transmitting and receiving antennas, which occurs because of the tradeoff between angular acceptance and antenna gain. In fact, being the transmitting-receiving antennas at a considerable distance (resulting in high free space losses) and being the transmission at higher frequencies (1-4 GHz) affected by interference caused by environmental obstructions, high gain is often required to cast sufficient power [3].
Another critical constraint in FF WPT is related to the limitations in the amount of power that can be delivered without causing adverse biological effects. In particular, a crucial indicator of the energy absorbed by a biological system exposed to an EM field at RF or at microwaves is the Specific Absorption Rate (SAR), which measures the rate at which the EM energy is absorbed by human body. In particular, SAR is directly related to the body temperature increase caused by the radiation exposure and energy absorption. Thus, high SAR levels (up to about 6.2 W/kg) due to strong power absorption by moisture and biological tissues at RF frequencies, should be avoided since it may lead to levels of heating that can alter essential biological activities [3].

An example of skin-interfaced power harvester based on FF RF technology is proposed in [14], where the functional components exploit ultrathin active and passive elements configured for soft, elastic and stretchable properties in such a way to guarantee a robust operation under significant levels of mechanical deformation. As illustrated in Fig. 8 (b) and (c), a receiving loop antenna connected to an impedance matcher are combined together via soft-contact lamination technique to a voltage doubler attached to a small-scale LED acting as a load just for functional purposes. In particular, the structure consists of stacked ultrathin layers of metals, polymers, and semiconducting materials in open-mesh serpentine layout to ensure soft, elastic, and stretchable mechanical properties for skin-mounted applications (Fig. 8 (e)). The antenna consists of circular serpentine metallic mesh structure, whereas the impedance matcher is an LC resonator where the capacitor uses a parallel plate design with serpentine layout on a Parylene-C material substrate (Fig. 8 (f)) and the voltage doubler consists of PIN diodes with single-crystalline nanomembranes of silicon as semiconductor. All the different thin film components are then printed on water soluble tapes and then assembled on a PDMS membrane, as shown in Fig. 8 (c) and (d).

Finally, this epidermal flexible RF wireless power transfer system allows to receive and rectify sufficient power for operating the many different components needed in epidermal technologies such as radio, sensors, memory devices and low power microprocessors.

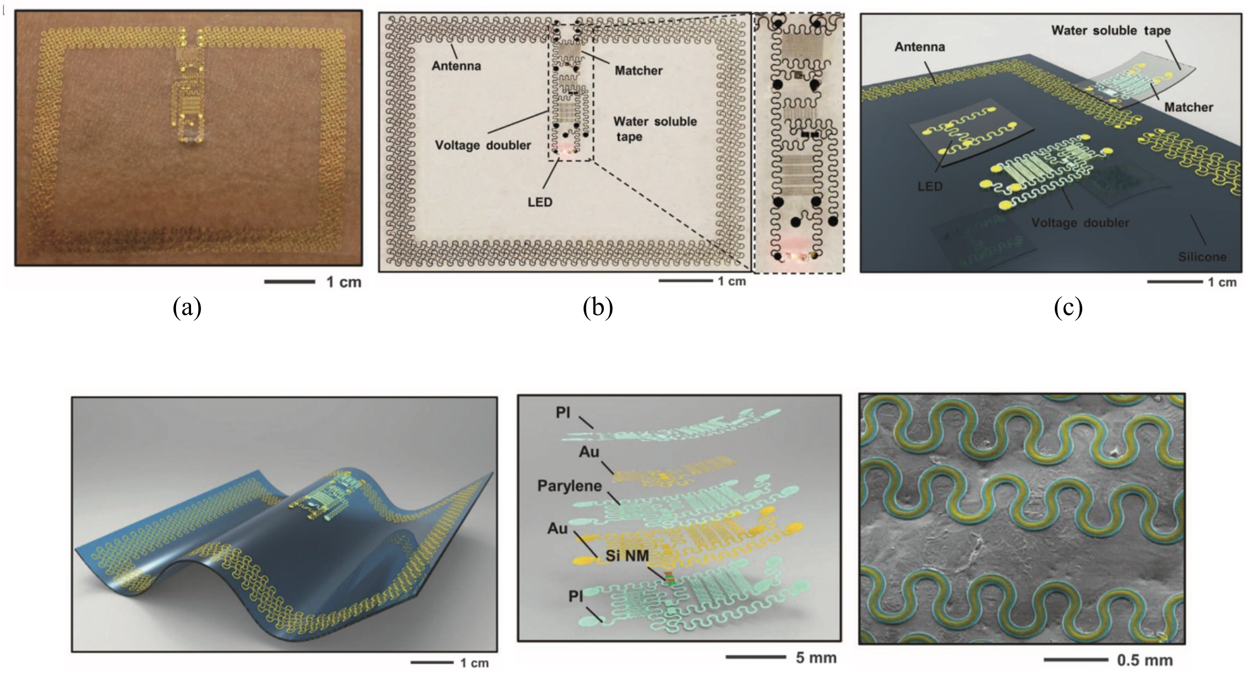

(a) (b) (c)

(d) (e) (f)

Fig. 8. (a) Schematic and implementation of an epidermal RF system for WPT application, (b) device assembly of different thin film components in an integrated functional system, (c) exploded view of a voltage doubler and (d) parallel plate capacitors in serpentine geometries on a skin replica [14].

Instead, NF WPT exploits non-radiative EM energy (within ~$\lambda/2\pi$ from the transmitter) and relies on inductive or capacitive coupling between transmitting and receiving coils or electrodes at low frequencies. In particular, inductive links (exploiting magnetic field) are established between co-located (resonant) coils/wires, whereas capacitive links (exploiting electric field) are established between co-located (resonant) electrodes/metallic plates. In this case, unlike FF WPT, the interaction between transmitter and receiver is crucial, thus, being in the reactive field region, the power delivered to the field by the transmitter coil/plate returns back in case of receiver coil/plate absence and strongly depends on the position of the latter. In fact, in the reactive field region, power decreases rapidly, as $1/r^3$ (where r is the distance between transmitter and receiver), which is why the distance between the coils or the electrodes must be limited in order to focus the power, preventing operation at distances larger than ~1 m, without additional passive hardware.

However, the WPT NF system efficiency not only depends on the variable link distance, but also on the link misalignment, the orientation angle, the dimension of the coils/plates and the variable loading resistance, thus, transmitting and receiving resonators must be correctly tuned in order to have high quality factor (Q-factor) and to create strong resonant coupling. In particular, power transfer efficiency of magnetic resonant coupling is determined by the coupling coefficient *k*, between the primary (transmitting) and secondary (receiving) coils, as well as by their Q-factor. Both of these two quantities decrease with the coil size, leading to very low power transfer efficiency for devices with size below 10 mm^2, whereas *k* rapidly decreases with distance and lateral misalignment between the two coils [3].

One of the advantages of NF WPT non-radiative nature, is that magnetic resonant coupling, with frequencies ranging from ~100 kHz to ~200 MHz, is relatively insensitive to changes in dielectric environments and to the presence of obstacles, meaning that successful power transfer is possible even in cases where the line of sight between the two resonators is completely obstructed, in complex surroundings. Near-Field Communication (NFC) technologies are often deployed at 13.56 MHz, originally designed for RFID tags, authentication and wireless payments and now universally exploited in smartphones and tablets enabling high efficiency power transfer and data communication [1]. Moreover, low frequencies used in implantable/wearable applications involve reduced tissue absorption and therefore offer large penetration depths with minimal adverse biological effects, albeit with the requirement for larger receiving coils. This feature minimizes safety concerns during long term operation and has consequently facilitated its implementation in a wide range of wireless, battery-free, fully implantable devices for localized tissue oximetry, bioresorbable monitoring of intracranial pressure and temperature, for optogenetic stimulation in the central and peripheral nervous systems and for pharmacological modulation [3].

To provide an example of NF WPT application for battery-free, fully implantable devices, in [15] a miniaturized, soft, wireless and fully implantable optoelectronic system is presented.

Optogenetic is a biological technique that allows rapid, temporally specific control of neuronal activity by targeted expression and activation of light-sensitive proteins. In order to achieve the optogenetic modulation of the spinal cord and peripheral nervous system, in recent years there have been many improvements in the research for technologies that combine thin, mechanically soft neural interfaces with fully implantable, stretchable wireless radio power and control system, to overcome the limitations due to cumbersome tethered fiber-optic cables or Light Emitting Diode (LED) arrays, which impede natural movements and damage the surrounding neural tissue. Thus, in [15], a miniaturized, wireless optoelectronic system is proposed. It is composed of a stretchable wideband antenna able to harvest RF power through capacitive coupling between adjacent serpentine traces at the central operating frequency of 2.34 GHz, thus, reducing the antenna dimensions to 3 x 3 mm and its weight, Fig. 9 (d). The receiving antenna is then connected to a rectifier that converts the RF energy harvested into dc output to power the LEDs, as illustrated in Fig. 9 (a). The antenna and the LEDs are connected with serpentine electrical interconnects, as shown in Fig. 9 (e), and the overall circuit is encapsulated by polyimide and silicone elastomer, providing a soft, stretchable, biocompatible device that can be implanted underneath muscle for optogenetic stimulation of peripheral nerve, see Fig. 9 (b) and (c). From experimental results, it has been demonstrated that the strain doesn’t alter the efficiency of the capacitive coupling, even though it deforms the metallized traces increasing the size of the gap between them and causes a shift in the central resonant frequency that results to be small if compared to the large antenna bandwidth. Also, measures of the SAR levels have been carried out and have been found to be below safety guidelines.

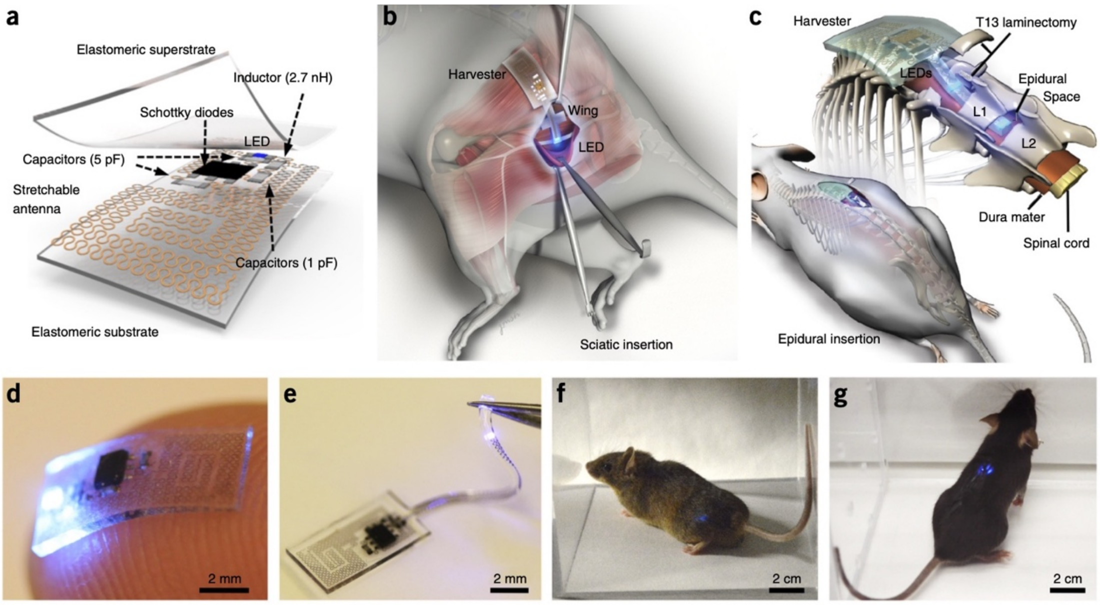

Fig. 9. (a) Exploded view schematic of the energy harvester components of the miniaturized, fully implantable, soft optoelectronic system for wireless optogenetics, (b,c) anatomical locations of the implanted device in a mice, (d) active device on the tip of finger, (e) highlight of the stretchable, soft interconnect of the device to a LED, (f,g) mice with wireless device implanted [15].

When dealing with WPT and EH the issue of optimizing the system efficiency is critical. Depending on the type of application and sensors, the power levels required for system operation may be high, as in the case of wireless recharging of vehicles, optoelectronic methods with high optical output, etc., or low, as in the case of smart watches, distributed sensors, etc..

Nevertheless, each system requires specific device engineering depending on the body location, sensor type and communication method, accounting for losses throughout the overall system and maximizing the efficiency of each stage component.

When intermittent power sources are considered, for example triboelectric, piezoelectric, biochemical, photovoltaic sources, some additional components such as buffers, batteries, or supercapacitors, are needed in order to provide constant and sustained power to the wireless device.

Otherwise, when RF power sources are exploited, the power obtained by the rectification process is typically sufficient for driving sensors and to enable wireless data communication, but a careful design of the transmitting and receiving antennas (in the case of FF WPT) or coils (in the case of NF WPT) is always necessary. In particular, in a FF WPT link, the transmitting and receiving antennas will be designed in such a way to have high gain and high directivity in order to overcome the losses due to the long distance propagation either in a free-space scenario or in a scenario full of obstacles, where scattering, transmission and diffraction can occur, whereas, in a NF WPT link, as mentioned, the efficiency must be ensured by properly designing the coils, but also the interaction between them and thus, their mutual coupling.

The efficiency of transmission-reception stage in the case of WPT or just in the reception stage, as concerning EH, is crucial because the power at the input of the rectifier must be sufficient in order to activate the diodes, meaning that the voltage at their input must be greater than their threshold voltage. Then, depending on the choice of the proper rectification scheme, the Power Conversion Efficiency (PCE) of the overall rectenna (rectifying antenna) system, must be maximized, also depending on the kind of load to which the power will be delivered.

However, since wireless communication often represents the most significant draw of power in battery-free devices and sensors, especially for operation over long distances and at high data-rates, low power protocols have been deployed lately.

In addition, a recent concept of RF WPT which allows to improve the overall system efficiency is the Simultaneous Wireless Information and Power Transfer (SWIPT), which provides the simultaneous transmission of data and power via the same EM wave. In particular, there are two popular SWIPT schemes: power splitting (PS) or time switching (TS). The former scheme consists of conveying power and data by means of the same modulated signal, whereas the latter switches between the data and power transmission modes over time. It is demonstrated that the PS SWIPT scheme has a better tradeoff between data rate and harvested power [16].

An interesting example of wireless and fully wearable device designed for human breath monitoring and adopting the SWIPT concept, has been proposed in [17]. Here, a Self-Injection Locked Oscillator (SILO) whose input and output ports are aperture-coupled to a dual polarized patch antenna and a passive receiver, consisting of a cascade connection of a peak detector and a full-wave RF-to-dc rectifier, generates a carrier at 5.8 GHz. This signal is then frequency-modulated by chest displacement caused by breathing and is backscattered to the SILO, so that the SILO output signal is simultaneously demodulated by the detector, and dc-converted to provide energy for the wireless communication of the received vital signals by means of an integrated Bluetooth module. The overall system block diagram is reported in Fig. 10 (a). Whereas, in Fig. 10 (b) and (c) the voltage source V_{IN} and the voltage of the detected signal V_{DET} can be appreciated for a simulation period of 30 seconds. In this case, for every period (1 second) of the modulating signal, it is possible to notice two peaks, one for the inhalation and one for the exhalation, highlighted in figure to demonstrate that the adopted topology is able to detect the breath rate at 1 Hz.

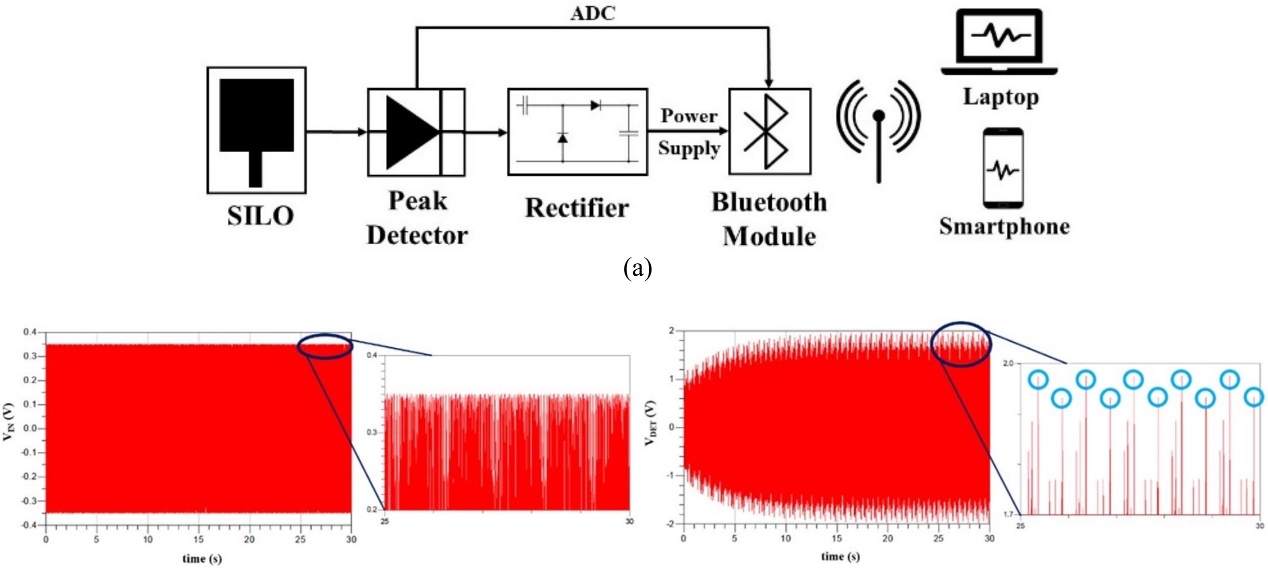

(a)

(b)

(c)

Fig. 10. (a) System block diagram of the overall SWIPT system for wireless breath monitoring, (b) simulated behavior of the source input voltage V_{IN} *and (c) of the* V_{DET} *for a transient simulation of 30 seconds [17].*

This insight in the recent developments concerning materials, design, and technologies for realizing functional interfaces in the context of biocompatibility, flexibility, wireless data communication and wireless power transfer, paves the way to the research activity presented within this thesis.

In fact, the aim of this thesis is to demonstrate that 3D-printing technologies can be considered significantly attractive in the production of microwave devices and in the antennas design and fabrication, with the intention of making them lightweight, inexpensive and easily integrable, replacing the use of stiff, difficult to process, and very expensive materials traditionally used as substrates for the production of wireless, battery-free wearable sensors and devices for vital signals monitoring. In particular, in this work a 3D-printed, low-cost, lossy, flexible resin material, namely the Flexible80A, is characterized and successively used for designing a wearable FF WPT device consisting of a patch antenna connected to a rectifier. In particular, 3D-printing innovative manufacturing techniques which allow to reduce the insertion losses and, thus, provide excellent radiation performances comparable to those of traditional rigid substrates.

The Flexible80A is a 3D-printable photopolymer resin material distributed by Formlabs (Somerville, MA, USA), that can be treated to be flexible; in particular, post-curing for Flexible80A previews its heating at 60°C for ten minutes, guaranteeing a gain in tensile strength of +140%.
The 3D-printer used for the additive manufacturing of this resin material is the Formlabs Form 3, depicted in Fig. 11, which makes use of an innovative printing technique called Low Force Stereolithography (LFS), which balances speed, surface quality and reliability while maintaining a precise, dense laser spot to ensure accurate, repeatable prints. Lower print forces allow for light-touch support structures that tear away with ease. Inside the Form 3 is a redesigned optics engine, the Light Processing Unit (LPU), which contains a system of lenses and mirrors. Within the LPU, a galvanometer positions the high-density laser beam in the Y direction, passes it through a spatial filter, and directs it to a fold mirror and parabolic mirror to consistently deliver the beam perpendicular to the build plane. The additive manufacturing is then followed by the post-processing, consisting of curing the Formlabs material sample in order to maximize its mechanical properties, as mentioned, (in the case of the Flexible80A resin, the post-curing allows to enhance the material flexibility), and washing it with Isopropyl Alcohol (IPA) to get perfectly clean surfaces. The accuracy of Form 3 is 25 micron for XY resolution and 25-300 microns (user selectable) in the Z, using an 85-micron laser (250 mW laser power), but it can also depend on the print performance of the individual resin [18].

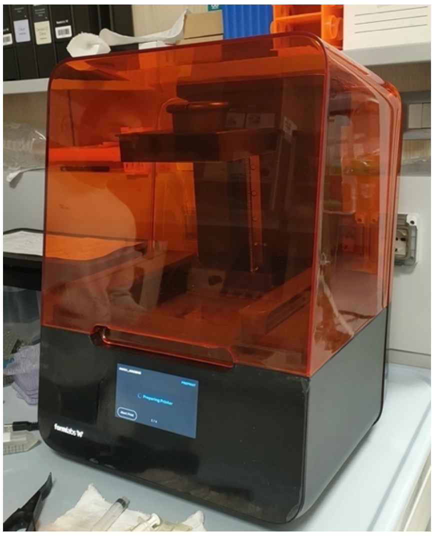

Fig. 11. Picture of the 3D-printer Formlabs Form 3.

To the authors' knowledge, the Flexible80A material has not been used before as a substrate for microwave circuits and its electromagnetic characteristics are not available in any frequency band. Therefore, as accurately presented in Chapter 3, a Flexible80A material sample has been used to characterize its EM properties, namely its loss tangent and electric relative permittivity, on the frequency band 0 ÷ 10 GHz by means of the T-resonator method.

Since from this EM characterization the Flexible80A has resulted to be a very lossy material, in Chapter 4 different new micromachining techniques, made feasible by the design freedom enabled by additive manufacturing, have been investigated in order to reduce the impact of its losses in terms of both propagation and radiation performances; in particular, Grounded Coplanar Waveguide (GCPW) technology has been compared to the traditional microstrip technology (an overview of transmission line theory concerning propagation in planar structures is reported in Chapter 2), revealing to be more suitable for enhancing the propagation performance in lossy substrates. In addition, different types of dielectric etchings performed in the gaps between the transmission line and the coplanar ground, have been investigated to produce further benefits to the wave propagation.
Finally, in Chapter 5, taking into account the analysis on the reduction of the substrate losses presented in previous chapters, a miniaturized 2.45-GHz rectenna on Flexible80A for wearable WPT applications has been designed, simulated and measured, proving that the design freedom enabled by 3D-printing allows the use of low-cost dielectric material, even with poor EM properties, to realize wearable nodes that can be activated wirelessly. In detail, a section is dedicated to the design process of a miniaturized patch antenna realized on Flexible80A and operating at 2.45 GHz which accounts for the abovementioned innovating 3D-printing techniques allowing to enhance its radiation efficiency; then a section discusses the hot topic of the receiving antenna equivalent circuit representation as it has been addressed by many authors in literature, and the position adopted in this thesis, and the final sections concern the rectenna design and optimization, with the presentation of the simulated results, finally validated by the carried out measurements.

This thesis work has been carried out within the framework of the PRIN 2017 “WPT4WID” (Wireless Power Transfer for Wearable and Implantable Devices) project of national interest funded by the Italian Ministry of Education, University and Research (MIUR).

Moreover, it has led to the submission of two works submitted at two international conferences, i.e., the 2022 IEEE International Microwave Biomedical Conference (IMBioC 2022) [19] and the 2022 IEEE Wireless Power Week Conference (WPW 2022) [20].

2. ELECTROMAGNETIC GUIDED PROPAGATION: AN OVERVIEW OF TRANSMISSION LINES

Transverse Electromagnetic (TEM) solutions of the Maxwell's equations can exist only if the dielectric material in between the two perfect conductors is homogeneous [21]. Most of the times are considered cylindrical structures those whose configuration is similar to the one of the actual transmission lines, but they can't guide TEM modes since the homogeneity condition is not verified. These guides can be called quasi-TEM (q-TEM).
The structural resemblance of TEM and q-TEM transmission modes allows, even if under certain limiting hypothesis, to apply to q-TEM structures the transmission line's circuital concepts.
This is possible since q-TEM modes, at sufficiently low frequencies, have properties comparable to the TEM modes: cut off frequency equal to 0, transversal field distribution approximating a static distribution, and axial components of the field intensity small with respect to the transversal ones. Thus, it is possible to define voltages and currents at any transversal section and to apply the circuital description even to q-TEM structures.
The q-TEM propagation along conductors on an inhomogeneous lossless dielectric material can be approximatively described, in terms of voltages and currents, by a system of Telegrapher's equations identical to the ones valid for TEM propagation in a lossless homogeneous medium:

$$\begin{aligned} \frac{\boldsymbol{dV}}{\boldsymbol{dz}} &= -\boldsymbol{j\omega L_0 I}(\boldsymbol{z}) \\ \frac{\boldsymbol{dI}}{\boldsymbol{dz}} &= -\boldsymbol{j\omega C V}(\boldsymbol{z}) \end{aligned} \tag{1}$$

where L_0 and C are the inductance and capacitance matrices respectively.
The solutions of (1) are of the kind:

$$\begin{aligned} \boldsymbol{V}(\boldsymbol{z}) &= \boldsymbol{V_0}\, \boldsymbol{e^{-\gamma z}} \\ \boldsymbol{I}(\boldsymbol{z}) &= \boldsymbol{I_0}\, \boldsymbol{e^{-\gamma z}} \end{aligned} \tag{2}$$

where V_0 and I_0 are constants to determine and, assuming a lossless structure:

$$\boldsymbol{\gamma} = \boldsymbol{j\beta} = \pm \boldsymbol{j}\frac{\boldsymbol{\omega}}{\boldsymbol{v_p}} \tag{3}$$

where v_p is the phase velocity and ω is the angular frequency.
Therefore, a transmission line with *m* conductors on inhomogeneous dielectric is able to guide *m* q-TEM modes linearly independent with different propagation constants. In fact, since the dielectric is not homogeneous, the energy driven by a generic mode is distributed differently in the various

dielectric regions, which have different phase velocities. But, since the mode velocity must be unique, the actual propagation velocity is a weighted average of the velocity in the different regions.
In a lossless homogeneous medium, the TEM propagation is characterized by phase velocity and wave impedance:

$$\boldsymbol{v_p} = \frac{\mathbf{1}}{\sqrt{\boldsymbol{\mu\varepsilon}}} = \frac{\mathbf{1}}{\sqrt{\boldsymbol{\mu_0\varepsilon_0\varepsilon_r}}} = \frac{\boldsymbol{v_0}}{\sqrt{\boldsymbol{\varepsilon_r}}}$$

$$\boldsymbol{\eta} = \sqrt{\frac{\boldsymbol{\mu}}{\boldsymbol{\varepsilon}}} = \sqrt{\frac{\boldsymbol{\mu_0}}{\boldsymbol{\varepsilon_0\varepsilon_r}}} = \frac{\boldsymbol{\eta_0}}{\sqrt{\boldsymbol{\varepsilon_r}}} \tag{4}$$

where it has been assumed the medium having magnetic permeability $\mu = \mu_0$, relative permittivity ε_r, and v_0 speed of light in free space.
The generic (i-th) q-TEM mode of a m-wires line with inhomogeneous dielectric has phase velocity:

$$\boldsymbol{v_{pi}} = \frac{\boldsymbol{v_0}}{\sqrt{\boldsymbol{\varepsilon_{i,eff}}}} \tag{5}$$

which defines the quantity:

$$\boldsymbol{\varepsilon_{i,eff}} = \left(\frac{\boldsymbol{v_0}}{\boldsymbol{v_{pi}}}\right)^{\mathbf{2}} \tag{6}$$

called **Effective Relative Permittivity** of the q-TEM mode.
The phase velocity of the q-TEM mode coincides with the TEM one propagating in a homogeneous medium with relative dielectric permittivity $\varepsilon_{i,eff}$.
Similarly, an effective wave impedance of the q-TEM mode can be defined:

$$\boldsymbol{\eta_{i,eff}} = \sqrt{\frac{\boldsymbol{\mu_0}}{\boldsymbol{\varepsilon_0\varepsilon_{i,eff}}}} = \frac{\boldsymbol{\eta_0}}{\sqrt{\boldsymbol{\varepsilon_{i,eff}}}} \tag{7}$$

The characteristic impedance matrix of the homogeneous line is defined as:

$$\boldsymbol{Z_{ci}} = \frac{\eta_{i,eff}}{\mu_0}\boldsymbol{L_0} = \boldsymbol{v_{pi}L_0} \tag{8}$$

Now, in order to take into account the losses, a perturbative analysis can be used to calculate the attenuation constants due to little losses in the conductors and in the dielectric, $\alpha_{mi} \simeq \Delta\beta_i$ and α_{ci}, respectively. Thus,

$$\boldsymbol{\gamma_i = j\frac{\omega}{v_{pi}} + \alpha_{di} + \alpha_{mi} + j\Delta\beta_i} \tag{9}$$

where $j\frac{\omega}{v_{pi}}$ represents the β_0 expression for the *i*-th q-TEM mode.

Considering an ordinary transmission line with inhomogeneous dielectric (*m*=1*)*, the matrices L_0, C_0 and C become scalars:

$$\boldsymbol{L_0} = \frac{\mu_0\varepsilon_0}{C_0} \tag{10}$$

thus (C_0 calculated in the air), the phase velocity of the only q-TEM mode can be expressed as:

$$\boldsymbol{v_p} = \frac{1}{\sqrt{L_0C_0}} = \sqrt{\frac{C_0}{\mu_0\varepsilon_0 C}} = \boldsymbol{v_0}\sqrt{\frac{C_0}{C}} \tag{11}$$

from which follows:

$$\boldsymbol{\varepsilon_{eff}} = \boldsymbol{\frac{C}{C_0}} \tag{12}$$

Expression (13) gives an immediate physical interpretation of the effective permittivity concept. The phase constant can be written as:

$$\boldsymbol{\beta} = \pm\frac{\omega}{v_p} = \pm\frac{\omega}{v_0}\sqrt{\frac{C_0}{C}} \tag{13}$$

And the characteristic line impedance :

$$Z_c = \frac{1}{v_p C} = \sqrt{\frac{L_0}{C}} = \frac{1}{v_0\sqrt{CC_0}} \tag{14}$$

The inner resistance and inductance for unit length of imperfect conductors can be found as:

$$R = 2\alpha_m Z_c \tag{15}$$

$$L_i = \frac{2}{\omega}\Delta\beta Z_c = \frac{R}{\omega} \tag{16}$$

Moreover, in case the dielectric has an electrical conductivity small but finite, it gives origin to the attenuation constant contribution α_d, which can be interpreted, in the circuital description of the line, introducing a transversal conductance for unite length, *G*, defined as:

$$G = 2\alpha_d Y_c \tag{17}$$

And the propagation constant becomes:

$$\boldsymbol{\gamma = j\omega\sqrt{L_0 C} + \alpha_d + \alpha_m + j\Delta\beta} \tag{18}$$

with $\Delta\beta = \alpha_m$.

A transmission line stores electric and magnetic energy, and for an alternating signal at a certain position on the line, energy is converted from one form to the other as time progresses. As such, a line has a circuit form that combines inductors L (for the magnetic energy), capacitors C (for the electric energy), and resistors R (modeling losses), whose values depend on the line geometry and material properties.

The transmission lines considered in this chapter are restricted to just two parallel conductors, (see Fig. 12 (a)), with a distance between the two lines being substantially smaller than the wavelengths of the signals on the line. The conductors of a transmission line confine and guide an EM field, which contains and transports the energy.

The Telegrapher's equations for a transmission line modeled as subsections of *RLGC* elements was derived. Very good accuracy is obtained if the length of a subsection is no more than $\lambda/20$. The full transmission line model is the cascade of many transmission line subsections.

Fig. 12 (b) shows the circuital description of an infinitesimal piece *dz* of transmission line on a dielectric inhomogeneous medium with losses:

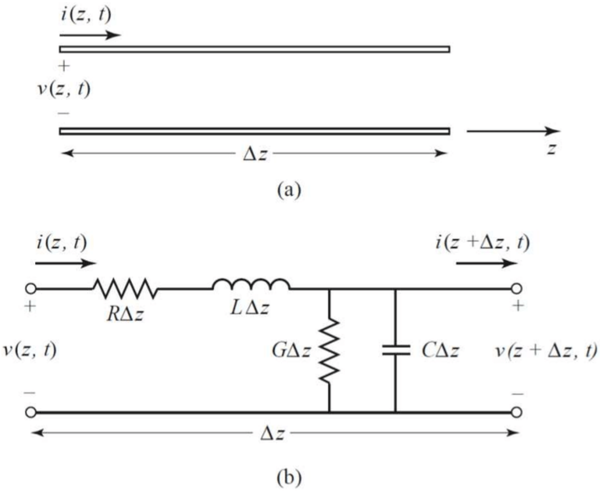

Fig. 12. Infinitesimal piece of transmission line (a), and circuital RLCG representation of an infinitesimal piece of transmission line dz on a dielectric inhomogeneous medium with losses [22].

The quantities *R, L, C*, and *G*, constant with respect to *z*, are called primary parameters of the line.

R, resistance for unit length, is due to the finite conductivity c_m of the conductors and is null if they're perfect ($c_m = \infty$). L, inductance for unit length, describes the ability to store magnetic energy and is mostly a function of geometry, as most materials used with transmission lines have μr = 1 (so no more magnetic energy is stored than in a vacuum); in a lossless case has value L_0, whereas, if the conductors are not perfect, $L = L_0 + L_i$, being L_i a contribution due to the conductors inner field. *C*, the capacity for unit length, describes the ability to store electrical energy and is mostly due to the properties of the dielectric, and *G*, transversal conductance per unit length, is due to the dielectric losses, if the latter has conductivity c_d different from 0, if it is perfect, then $c_d = 0\ and\ G = 0.$

The impedance of the line for unit length can be written as:

$$\boldsymbol{Z_s = R + j\omega L} \tag{19}$$

and the admittance for unit length:

$$\boldsymbol{Y_p = G + j\omega C} \tag{20}$$

Thus, the Telegrapher's equations become:

$$\boldsymbol{\frac{dV}{dz} = -Z_s I}$$

$$\boldsymbol{\frac{dI}{dz} = -Y_p V} \tag{21}$$

from which, in order to have not obvious solutions, the propagation constant must be:

$$\boldsymbol{\gamma = \pm\sqrt{Z_s Y_p},} \tag{22}$$

and since:

$$\boldsymbol{\gamma = \alpha + j\beta = \pm\sqrt{Z_s Y_p} == \pm\sqrt{(R + j\omega L)(G + j\omega C)}} \tag{23}$$

It can be obtained:

$$\alpha = \pm\frac{1}{\sqrt{2}}\sqrt{\sqrt{(R^2+\omega^2L^2)(G^2+\omega^2C^2)}-(\omega^2LC-RG)} \qquad (24)$$

$$\beta = \pm\frac{1}{\sqrt{2}}\sqrt{\sqrt{(R^2+\omega^2L^2)(G^2+\omega^2C^2)}-(\omega^2LC-RG)} \qquad (25)$$

where α and β are respectively the attenuation and phase constants. The term "constant" enhances the fact that γ, α, β are independent from z.
The quantity

$$Z_c = \frac{Z_s}{\sqrt{Z_sY_p}} = \sqrt{\frac{Z_s}{Y_p}} = \sqrt{\frac{R+j\omega L}{G+j\omega C}} \qquad (26)$$

is called **Characteristic line impedance**.
α, β, Z_c are also called secondary line parameters.

Among the different types of waveguides which can be found in literature, this discussion will focus on planar technology transmission lines and antennas. In fact, planar technology allows to realize low profile, light-weight and easily integrable antennas and transmission lines on dielectric substrates which act as supports. Planar technology is particularly exploited at microwave and millimeter wave frequencies on printed or integrated circuits. At higher frequencies, particularly into the millimeter wavelength ranges (above 30 GHz), losses (including radiation) increase significantly, the transmission line characteristics vary greatly with frequency (phenomenon of frequency dispersion), the field directions cannot be confined to the transverse plane, and fabrication tolerances become exceedingly difficult to meet as the required substrate thickness becomes very thin. With monolithic ICs, fabrication tolerances are much finer than with hybrid MICs and the options available for both microstrip and other transmission structures are extended [23].

There are two major categories of planar transmission lines that can be sorted according to the uniformity of the medium surrounding the transmission line conductors. When the embedding medium is uniform, the transmission line structures are referred to as homogeneous. If there are two or more regions with different permittivity the transmission line is called inhomogeneous. The most important planar transmission line structures are shown in Fig. 13. The main difference between the two sets of configurations (homogeneous and inhomogeneous) is the frequency-dependent variation of the EM field distributions with inhomogeneous lines. With inhomogeneous lines, the EM fields are not confined entirely to the transverse plane even if the conductors are perfect. However, they are largely confined to the transverse plane and so these lines are called quasi-TEM lines.

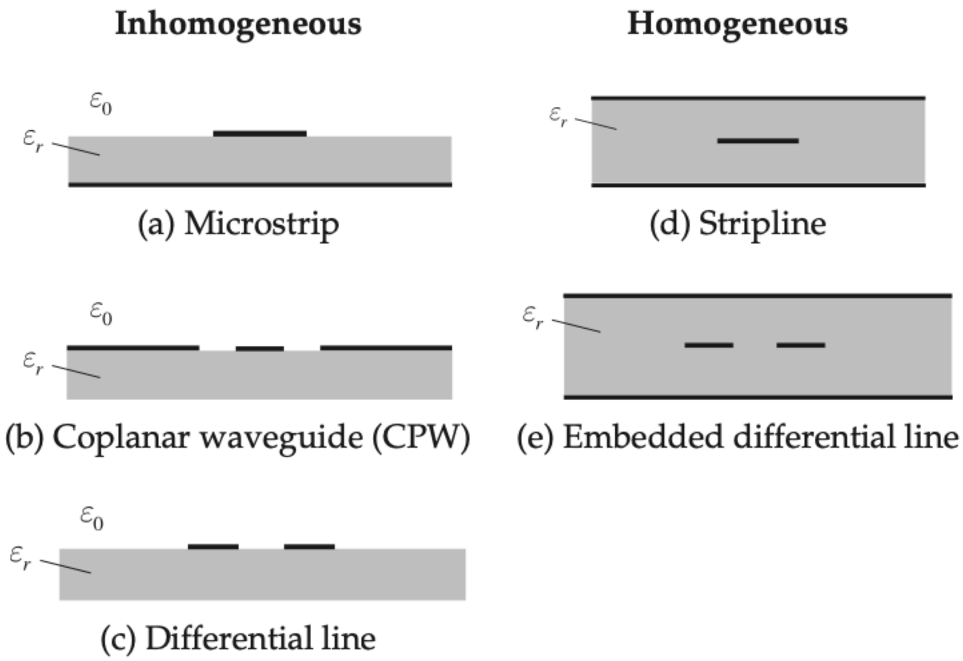

Fig. 13. Transversal section of different planar transmission line tipologies [23].

2.1. MICROSTRIP

The simplest transmission line to realize is the microstrip: the thin conductor film (thickness *t*) is deposited on the dielectric substrate (height h and relative permittivity ε_r) forming a fully laminated layer and the extra metallization is then mechanically removed (through a milling machine) or chemically "etched". Depending on the dielectric material chosen as substrate and the geometrical shape of the metallization, a radiative or guided behavior of the wave can be easily predicted. If the following conditions are verified, then the wave is guided between the signal conductor and the ground at the bottom of the dielectric substrate, and the theory of microstrip transmission line is valid:

$$\begin{gathered} \boldsymbol{w} \ll \boldsymbol{\lambda} \\ \boldsymbol{h} \ll \boldsymbol{\lambda} \end{gathered} \tag{27}$$

where λ is the wavelength in the dielectric medium evaluated as $\frac{\lambda_0}{\sqrt{\varepsilon_r}}$, and λ_0 is the wavelength in the air.

If (27) is violated, the guided behavior of the wave is not guaranteed anymore, and the structure can be exploited for its radiating properties.

The width of the microstrip also determines the characteristic impedance Z_c of the line and Fig. 14 (a) shows how the characteristic impedance decreases for increasing values of *w* or for thinner substrates, for different relative permittivity constants. Fig. 14 (b) shows, instead, the variation of the effective dielectric permittivity for increasing values of the line width or decreasing substrate height, where it can be seen that ε_{eff} increases for wide strips. This is because more of the EM field is in the substrate.

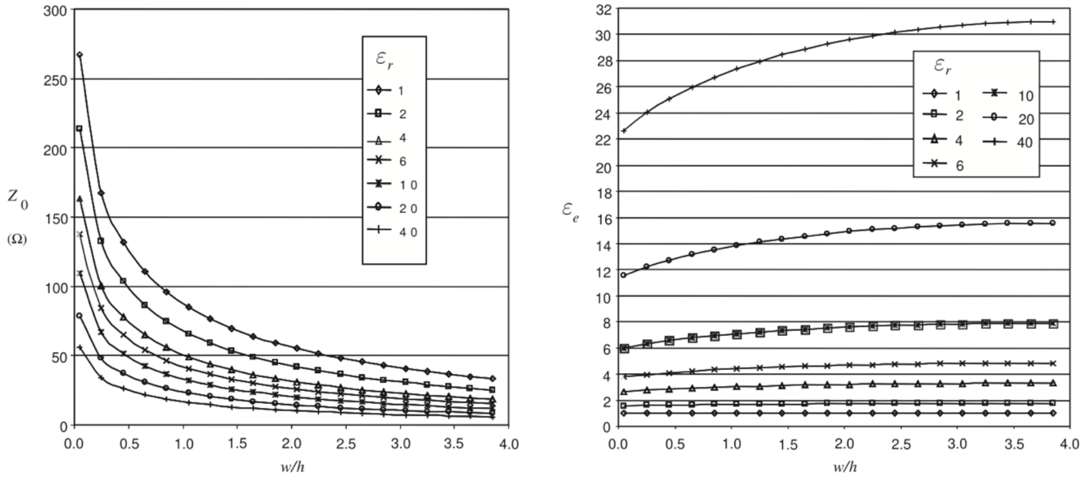

(a)

(b)

Fig. 14. (a) Behavior of a microstrip characteristic impedance with respect to w/h (where w is the line width and h is the substrate height) for different relative permittivities, and (b) variation of the effective permittivity with respect to w/h for different relative permittivities [23].

As previously mentioned, the microstrip transmission line is an inhomogeneous structure, since the EM field is highly affected by the presence of two different dielectrics, the dielectric substrate with relative permittivity ε_r and the air with permittivity ε_0. The phenomenon which leads to having part of the field propagating in the air is called **Fringing Effect** and it is strongly frequency dependent, see Fig. 15. According to the transmission lines theory, the TEM wave needs a homogeneous structure to propagate, thus, the microstrip line guides a hybrid mode having all the six field components. However, if a range of frequency below microwaves is considered, the field longitudinal components are much smaller than the transversal ones, this is why the propagating mode can be approximated to the q-TEM mode [24].

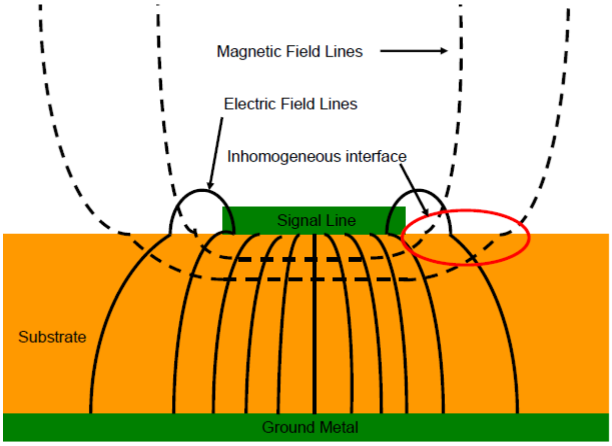

Fig. 15. Transversal section view of a microstrip line with EM field lines [25].

The microstrip study consists in finding the parameters characterizing the transmission line, in particular the phase propagation constant and the characteristic line impedance.
Without going into further detail, it is sufficient to evaluate the secondary parameters of the line β and Z_c simply using the capacitance per unit length C_0 if the structure is in the air and C in the case with the dielectric substrate. Then, the equations (13) and (14) from Chapter 2 are reported:

$$\boldsymbol{\beta = \omega\sqrt{LC} = \omega\sqrt{L_0 C\frac{C_0}{C_0}} = \frac{\omega}{c}\sqrt{\frac{C}{C_0}}} \tag{28}$$

$$\boldsymbol{Z_c = \sqrt{\frac{L_0}{C}} = \frac{1}{c\sqrt{CC_0}}} \tag{29}$$

Where c is the speed of light and it has been considered L=L_0 since the microstrip can be seen as a homogeneous structure as regards the magnetic permittivity; thus, it has the same inductance per unit length value a TEM line would have.

Moreover, (12) from Chapter 2 is here reported to better explain the effective relative permittivity meaning:

$$\boldsymbol{\varepsilon_{eff} = \frac{C}{C_0}} \tag{30}$$

This parameter describes how the electric field distributes between the air and the dielectric and, as shown in Fig. 14 (b), it strongly depends on the conductor width w and has always a value in the range:

$$\boldsymbol{1 < \varepsilon_{eff} < \varepsilon_r} \tag{31}$$

Where the limiting values are:

- for $w \rightarrow \infty$, is like having two parallel plates of conductors, i.e., the field is completely contained within the substrate material, thus, $\varepsilon_{eff} = \varepsilon_r$.

- For $w \to 0$, the microstrip becomes like a wire on the dielectric substrate, and therefore the field still distributes between the air and the dielectric. This is why the effective permittivity can be calculated as the average between the dielectric constant of the air and the substrate one:

$$\varepsilon_{eff} = \frac{\varepsilon_0 + \varepsilon_r}{2} \tag{32}$$

In particular, from literature, the approximated analytical expression which allows to evaluate ε_{eff} is:

$$\varepsilon_{eff} = \frac{\varepsilon_r + 1}{2} + \frac{\varepsilon_r + 1}{2} \cdot \frac{1}{\sqrt{1 + \frac{12h}{w}}} \tag{33}$$

So now the expressions for $\beta \ and \ Z_c$ can be rewritten as:

$$\beta = \omega\sqrt{LC} = \omega\sqrt{L_0 C \frac{C_0}{C_0}} = \frac{\omega}{c}\sqrt{\frac{C}{C_0}} = \frac{\omega}{c}\sqrt{\varepsilon_{eff}} \tag{34}$$

$$Z_c = \sqrt{\frac{L_0}{C}} = \frac{1}{c\sqrt{CC_0}} = \frac{1}{cC_0\sqrt{\varepsilon_{eff}}} \tag{35}$$

2.2. COPLANAR WAVEGUIDE

Coplanar waveguides (CPW) offer several advantages over microstrips for monolithic or hybrid microwave integrated circuits (MIC), [26]. However, their use is not so widespread due to their complex layout. A coplanar waveguide consists of a strip of thin metallic film deposited on the surface of a dielectric substrate and separated by a narrow gap from two ground conductors running adjacent and parallel to the same surface on either side, see Fig. 16 (a).

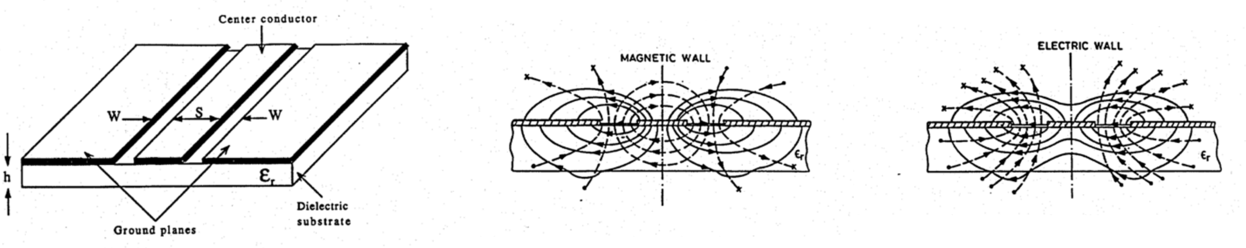

(a) (b) (c)

Fig. 16. (a) Coplanar waveguide and EM field lines (continuous lines are the electric field lines and dashed lines are the magnetic field lines); (b) shows the q-TEM or coplanar mode, (c) shows the non-TEM mode or coupled slotline mode [27].

The coplanar waveguide basically supports two modes of propagation: one is a quasi-TEM mode, where the fields in the two slots are 180° out of phase, the other is a non-TEM mode, where the fields are in phase, [27]. In CPW microwave circuits, the desired mode is the q-TEM one due to its low radiation properties, see Fig. 16 (b) and (c) respectively. The two ground planes must be maintained at the same potential to prevent the unwanted mode propagating. One of the main advantages of the CPW is that all the conductors lie on the same plane, and therefore, there is no need for via holes which makes it easy to connect shunt or series lumped elements.

Another important characteristic of CPWs is that the line impedance and phase velocity are less dependent on the substrate height than on the aspect ratio (slot width/center conductor width). This is because the field is mainly concentrated in the slots rather than in the substrate, as occurs in the microstrip case.

The dimensions of the center strip, the gap, the thickness, and permittivity of the dielectric substrate determined the effective dielectric constant (ε_{eff}), characteristic impedance (Z_0) and the attenuation (α) of the line. The gap in the coplanar waveguide is usually very small relative to the thickness of the dielectric and supports electric fields which are almost equally divided between the air and dielectric [28], [23].

In particular, the effective relative permittivity of CPW is:

$$\boldsymbol{\varepsilon_{eff} = \frac{1}{2}(\varepsilon_r + 1)\{\tanh\left[1.785\log\left(\frac{h}{s}\right) + 1.75\right] + \left(\frac{ks}{h}\right)[0.04 - 0.7k + 0.01(1 - 0.1\varepsilon_r)(0.25 + k)]\}} \tag{36}$$

which is accurate to 1.5% for *h*/*s* ≥ 1.

In (36),

$$\boldsymbol{k = \frac{w}{w + 2s}} \tag{37}$$

where *w* is the conductor transmission line strip and *s* is the width of the gap between the transmission line conductor and the coplanar ground.

The characteristic impedance of CPW is

$$\boldsymbol{Z_0 = \frac{30\pi\, K'(k)}{\sqrt{\varepsilon_{eff}}K(k)}} \tag{38}$$

where

$$\boldsymbol{k' = \sqrt{(1 - k^2)}} \quad \textbf{and} \quad \textbf{K'(k) = K(k')} \tag{39}$$

K(k) and *K'(k)* are elliptic integrals, but the ratio, which is all that is required, is much simpler:

$$\boldsymbol{\frac{K(k)}{K'(k)} \approx \frac{1}{\pi} ln\left(2 * \frac{1 + \sqrt{k}}{1 - \sqrt{k}}\right) \quad if\ \ 0 \le k \le 0.707}$$

$$\boldsymbol{\frac{K'(k)}{K(k)} \approx \frac{1}{\pi} ln\left(2 * \frac{1 + \sqrt{k'}}{1 - \sqrt{k'}}\right) \quad if\ \ 0.707 < k \le 1} \tag{40}$$

Note that with CPW, Z_0 is determined by the ratio of the center strip width *w* to the gap width *s*. This makes the design of a CPW line with a particular Z_0 non unique, because an infinite range of *w* and *s* values will result in a specific Z_0 requirement. This provides additional design flexibility.

As previously mentioned, the loss of a CPW is primarily due to dielectric, radiative, and conductor losses. Dielectric loss is lower in CPW line than in a microstrip line as the electric field lines are evenly divided between the air and the dielectric, whereas with a microstrip line most of the field is concentrated in the dielectric. Also, radiation loss with CPW is much lower than with microstrip as the field lines with a CPW line are much more tightly confined. In practice, when *s/h* is near to or greater than 1, the structure partially turns into a microstrip transmission line, and it is of no use as a CPW line.

Coplanar waveguides can be easily classified as follows:

- Conventional CPW
- Conductor Backed CPW or Grounded CPW (GCPW)
- Micromachined CPW

Up to this point the Conventional CPW has been discussed. The Grounded CPW has an additional ground plane at the bottom surface of the substrate. This lower ground plane not only provides mechanical support to the substrate but also acts as a heat sink for circuits with active devices. The Micromachined CPWs are of two types, namely, the microshield line and the CPW suspended by a silicon dioxide membrane above a micromachined groove.

Since the structures discussed in this thesis make use of the Grounded Coplanar Waveguide, due to the fact that for the realization of wearable devices a back conductor is needed in order to avoid or reduce as much as possible the back radiation, let's further examine this kind of CPW.

2.3. GROUNDED COPLANAR WAVEGUIDE

GCPW circuits, also known as conductor-backed coplanar waveguide circuits, increase the amount of ground around a circuit compared to microstrip, by placing ground planes on the bottom of the dielectric material and on the top, on the same plane and on either side of signal transmission line, Fig. 17 (a).
GCPW circuit structures achieve electrical stability by literally surrounding a signal line with ground planes [29].
As well as Microstrip technology, GCPW circuits operate by means of a dominant q-TEM mode but, with their enhanced ground structures, are capable of wider effective bandwidth and wider impedance ranges than Microstrips.

As regards the EM field, in GCPW circuits it is mainly concentrated in the gaps between the coplanar ground planes and the signal transmission line, as shown in Fig. 17 (b), whereas it is weaker between the signal line and the bottom ground plane. Since a great deal of a GCPW's EM field energy propagates through the air around the circuitry, with its low dielectric constant of 1, rather than through conductive metal or dielectric material with much higher dielectric constant, the end result is a low net dielectric constant for the GCPW circuit board.

Moreover, due to the larger amount of metallization present in GCPW structures, they suffer greater conductor-losses than microstrip, but reduced radiation losses compared to the latter's.
In addition to this, the neighboring ground planes for the GCPW can significantly benefit in the suppression of spurious modes.

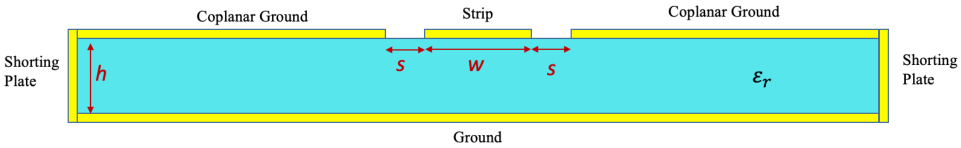

(a)

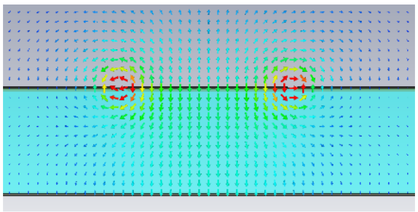

(b)

Fig. 17. (a) Transversal section of a GCPW and (b) same transversal section with electric field lines.

The equations of Z_0 and ε_{eff} are here reported [30]:

$$Z_0 = \frac{60\pi}{\sqrt{\varepsilon_{eff})}} \frac{1.0}{\frac{K(k_1)}{K(k'_1)} + \frac{K(k)}{K(k')}} \tag{41}$$

Where *k* and *k'* are given by expressions (37) and (39) respectively and

$$k_1 = \frac{tanh\left(\frac{\pi w}{4h}\right)}{tanh\left(\frac{\pi(w+2s)}{4h}\right)} \tag{42}$$

$$k'_1 = \sqrt{1 - {k'_1}^2} \tag{43}$$

$$\varepsilon_{eff} = \frac{1.0 + \varepsilon_r \frac{K(k_1)}{K(k'_1)} + \frac{K(k')}{K(k)}}{1.0 + \frac{K(k_1)}{K(k'_1)} + \frac{K(k')}{K(k')}} \tag{44}$$

To avoid microstrip line modes propagating, it is recommended that *h* >> (*w*+2*s*), which means that the substrate height influences the characteristic line impedance and the propagating properties. In fact, the thinner the substrate, the more the field couples with the back conductor and all the benefits of the GCPW are lost.

3. CHARACTERIZATION OF LOW-COST 3D-PRINTABLE AND FLEXIBLE MATERIAL: THE FLEXIBLE80A

In this chapter a low-cost resin 3D printable material distributed by Formlabs (Somerville, MA, USA) that can be treated to be flexible, the Flexible 80A, has been selected and characterized from the EM properties point of view. The aim is to use this substrate material for designing flexible, lightweight, battery-free, millimeter scale, non-invasive, wearable RFID tags to be used for continuous health monitoring.

3.1. T-RESONATOR METHOD

Analytical techniques for material characterization has been presented in the past, based on resonant techniques [31], in particular using the microstrip T-resonator topology considered in [32], which consists of a microstrip line connected to a quarter wavelength open stub, whose length can be calculated as:

$$L_{stub} = \frac{n \cdot c}{4 * f_n * \sqrt{\varepsilon_{eff}}} \tag{45}$$

Where n is the order of the resonance (n=1, 3, 5, …, odd numbers since it is an open stub), c is the speed of light, f_n is the frequency (in Hz) and ε_{eff} is the effective permittivity of the material. The stub length is thus designed in order to have the main resonance at a particular frequency of choice and the dielectric constant is based on an estimated value, which may be obtained by literature.

The goal is to characterize the dielectric permittivity and the loss tangent of the material considered in a particular frequency range. This is done through an iterative procedure which consists of comparing the absolute value of the transmission coefficient S_{12} of an open stub measured with a Vector Network Analyzer (VNA), with the simulated S_{12} of the same stub designed on an electromagnetic simulator of choice; in the present case, CST Microwave Studio (CST MS) has been used. In particular, several simulations are performed changing the electrical permittivity and the loss tangent, until the $|S_{12}|$ curve obtained by the simulation overlaps the measured one.

3.2. EXPERIMENTAL RESULTS OF THE FLEXIBLE80A CHARACTERIZATION

To begin with, a microstrip T-resonator has been created on a sample of Flexible80A with thickness 0.65 mm and dimensions 71.6 x 71.6 mm^2, using 31.8-µm-thick adhesive copper, for both the ground plane and the microstrip circuit. The stub has been designed in order to have the main resonance at 868 MHz, thus, from expression (45), L_{stub}= 58.4 mm.

A first guess value of $\varepsilon_{eff} = 2.19$ has been chosen, resulting in an initial relative dielectric constant ε_r of 2.67, whereas the 50-Ω microstrip line width w_m=1.75 mm has been obtained through the Macros Tool in CST. The measured and simulated structures are shown in Fig. 18 (a) and (b) respectively, where in the former, the color is given by open stub structure on the top layer and the ground copper at the bottom of the structure, since the Flexible80A material is transparent.

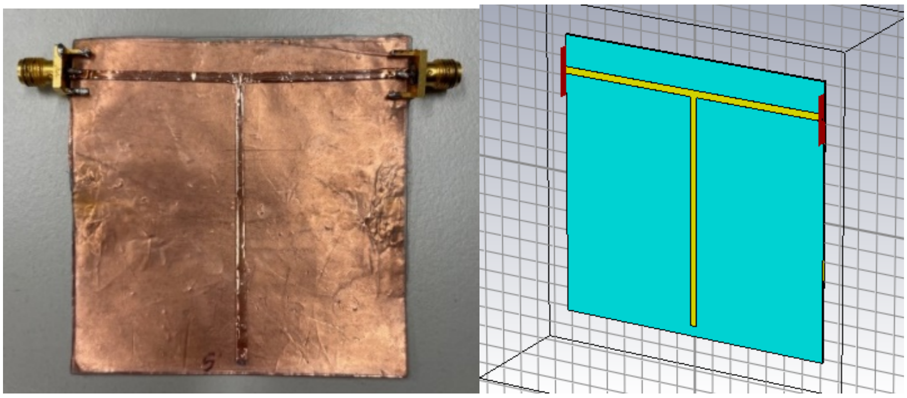
(a) (b)

Fig. 18. (a) T-resonator open ended stub, realized with copper tape on a Flexible80A sample, and (b) same structure reproduced and simulated on CST MS.

The stub has been measured in the frequency range 0 ÷ 6 GHz, thus, the material characterization has been carried out within the same frequency range, covering sufficient higher order harmonics for future nonlinear design of the entire wireless wearable system in the selected UHF band.

The User Dispersion Model option of CST MS has been used in order to give an overall indication of the ε_r and $tan\delta$ for a certain number of frequencies included within the abovementioned frequency range, giving particular interest to the stub resonance frequencies of the measured $|S_{12}|$ curve, shown in Fig. 19. The values of ε_r and $tan\delta$ have been changed until the main resonance frequencies of the simulated stub were matching the ones in the measured $|S_{12}|$ curve.

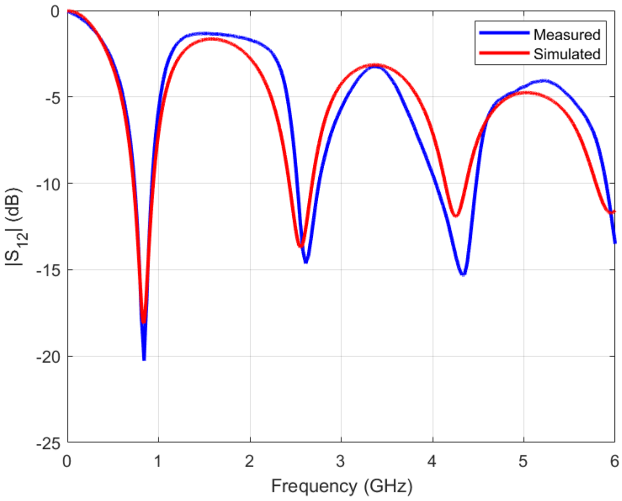

Fig. 19. Comparison between the measured and simulated $|S_{12}|$ curves of the designed T-Resonator.

In particular, it can be observed that for increasing values of ε_r the curve moves towards the left and vice versa, whereas increasing the value of $tan\delta$, the curve moves downwards, since the losses increase.

Fig. 19 shows the comparison between the $|S_{12}|$ curves of the measured and simulated T-Resonator, demonstrating that the final characterization obtained is sufficiently accurate in the frequency range 0 ÷ 6 GHz.

TABLE Ireports the dielectric properties obtained as final Flexible80A characterization, where the electrical conductivity is computed as follows: since $tan\delta = \frac{\sigma}{\omega\varepsilon}$ $, then\ \sigma = tan\delta\ \omega\ \varepsilon_0\ \varepsilon_r,$ where $\varepsilon_0 = 8.85 \cdot 10^{-12}$.

In particular, as can be noted in TABLE I, the dispersion phenomena are negligible in the frequency range of interest, and the final selected parameters at 868 MHz are ε_r = 2.67 and $\tan(\delta)$ = 0.11, which allow to reach almost overlapping |*S₁₂*| measured and simulated behavior over frequency.

TABLE I. FLEXIBLE80A MATERIAL CHARACTERIZATION IN TERMS OF ε_r, $tan\delta$ AND σ IN THE FREQUENCY RANGE 0 ÷ 6 GHz

Frequency	$\boldsymbol{\varepsilon_r}$	$\boldsymbol{tan\delta}$	$\boldsymbol{\sigma}$
0.5 GHz	2.98	0.13	$1.71 \cdot 10^{-3}$
0.868 GHz	**2.67**	**0.11**	$\mathbf{2.34 \cdot 10^{-3}}$
1.4 GHz	2.77	0.086	$2.95 \cdot 10^{-3}$
2 GHz	2.77	0.086	$4.22 \cdot 10^{-3}$
2.641 GHz	2.67	0.086	$5.36 \cdot 10^{-3}$
3 GHz	2.66	0.081	$5.3 \cdot 10^{-3}$
3.5 GHz	2.66	0.075	$6.18 \cdot 10^{-3}$
4 GHz	2.66	0.079	$7.44 \cdot 10^{-3}$
4.4 GHz	2.66	0.079	$8.18 \cdot 10^{-3}$
5 GHz	2.65	0.08	$9.38 \cdot 10^{-3}$
5.5 GHz	2.657	0.08	0.0103
6 GHz	2.66	0.08	0.0113
6.5 GHz	2.66	0.08	0.0122
7 GHz	2.67	0.079	0.013
7.5 GHz	2.68	0.0788	0.014
8 GHz	2.69	0.077	0.01466
8.5 GHz	2.7	0.0758	0.0154
9 GHz	2.73	0.073	0.0158
9.5 GHz	2.75	0.07	0.0161
10 GHz	2.78	0.066	0.0162

3.3. EXPERIMENTAL EVALUATION OF FLEXIBLE80A PROPAGATION PERFORMANCES

In order to validate the loss tangent characterization in the frequency range considered, it has been realized, with copper tape of thickness *t* = 31.8 µm, on a 0.65 mm-thick Flexible80A sample, four microstrip lines with different width corresponding to different characteristic impedances: 50 Ω, 40 Ω, 30 Ω, and 70 Ω. Each of them has been measured with a VNA in the frequency range 0 ÷ 6 GHz and then they have been reproduced and simulated on CST MS, where the substrate material has been characterized as previously described.

In Fig. 20 (a-d), the graphs comparing the $|S_{12}|$ curves of the simulated and measured microstrip lines are reported. As can be seen from these figures, the characterization can be considered to be accurate in the frequency range 0 ÷ 6 GHz. The sharp drop in the $|S_{12}|$ measured curves that can be seen in the graphs may be related to an imperfection of the substrate sample.

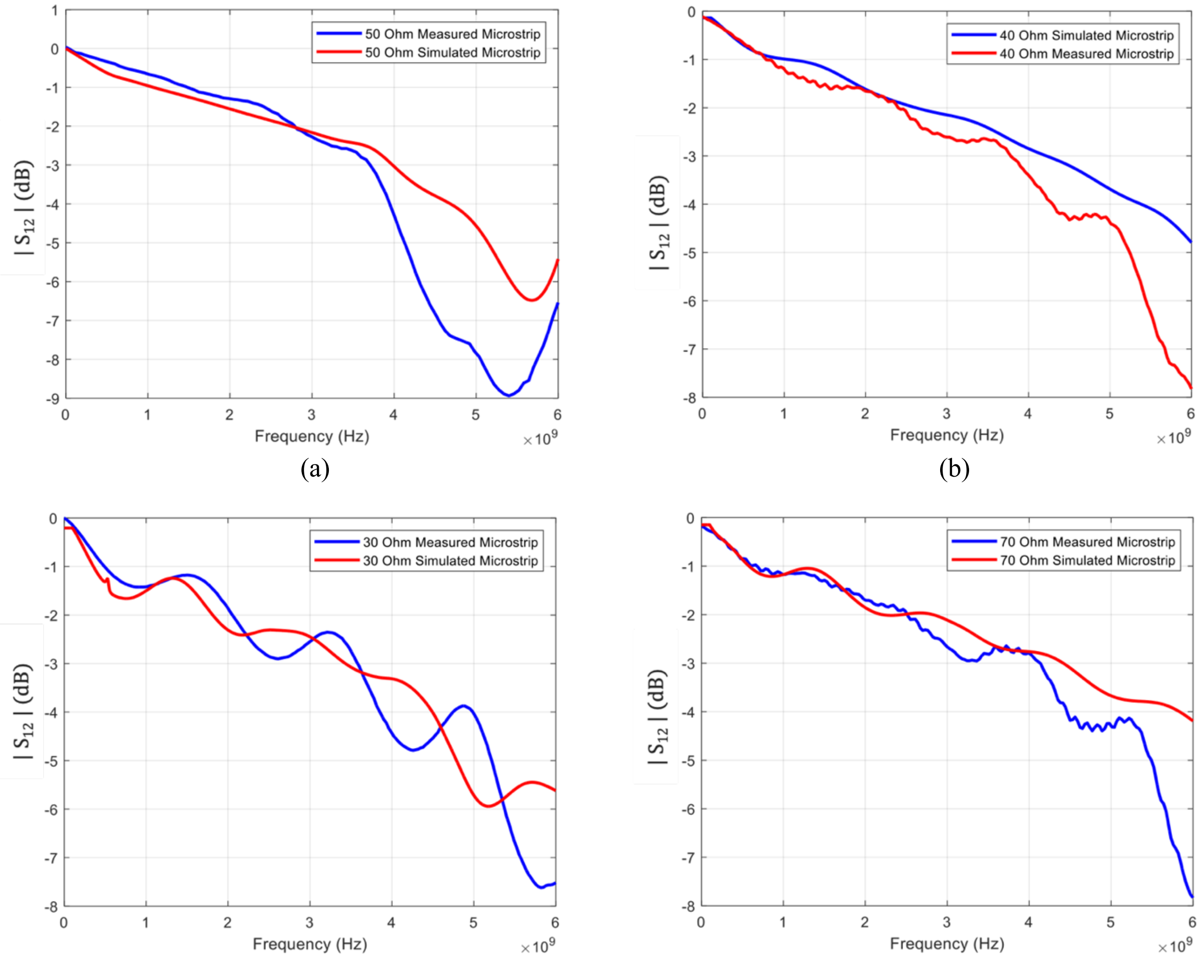

(a) (b)

(c) (d)

Fig. 20. Comparison between measured and simulated $|S_{12}|$ *curves of the (a) 50-Ω microstrip lines, (b) 40-Ω microstrip lines, (c) 30-Ω microstrip lines, (d) 70-Ω microstrip lines on Flexible80A.*

Since the substrate has resulted to be particularly lossy even at low frequencies, some techniques which would allow to improve the propagation performances have been investigated.

To begin with, microstrip and GCPW technologies have been compared. In particular, it has been observed that the GCPW technology allows to reduce the losses related to the wave propagation in the lossy medium with respect to the microstrip technology. This is because the quasi-TEM propagation takes place between the hot wire and the coplanar grounds mostly on the same plane, so that the field is partly in the air and partly in the substrate, whereas in the microstrip technology the field stays prevalently in the substrate.
Thus, a microstrip line and a GCPW both realized with 31.8 μm-thick copper adherent to a Flexible80A substrate sample of 0.93 mm of thickness have been measured, and what can be observed in Fig. 21 is that the coplanar technology reduces the losses of around 0.6 dB for lower frequencies (868 MHz) and almost exceeds 2 dB at highest measured frequency.

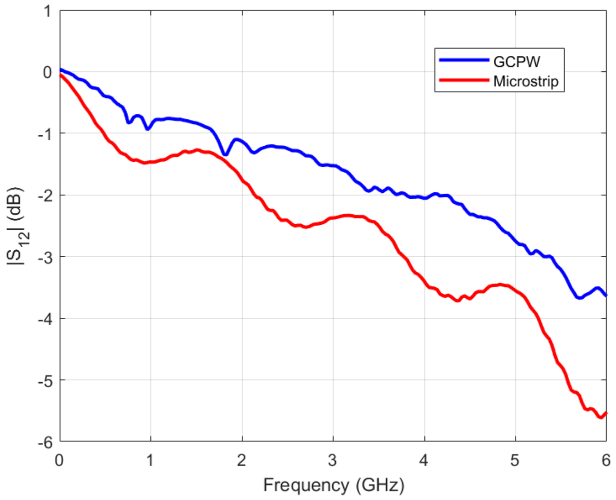

Fig. 21. Comparison between $|S_{12}|$ *curves of a measured microstrip line and a GCPW realized with copper tape on a sample of Flexible80A substrate.*

4. 3D-PRINTING TECHNIQUES FOR ENHANCING THE PROPAGATION CHARACTERISTIC OF THE FLEXIBLE SUBSTRATE

As previously mentioned and demonstrated in the previous chapter, the GCPW technology allows to reduce the substrate losses because of the ground very close and on the same plane of the hot wire, so that the field penetrates less the substrate and undergoes lower attenuation.
In order not to get rid of the advantages of this low-cost 3D-printable substrate, suitable techniques have been investigated based on 3-D printing to improve its propagation performance, drawing inspiration from sophisticated micromachining techniques [33].

Therefore, the substrate has been dug in the gaps in between the microstrip line and the coplanar ground, so that the q-TEM electric field is mainly located in the air rather than in the dielectric, reducing the losses due to the propagation in the lossy material.
Moreover, the full wave simulation of customized structures allows to optimize the shape of the etchings, based on the accurate analysis of the q-TEM electric field distribution: the optimal shape is chosen with the manifold goal of ensuring that the majority of the electric field intensity is immersed as much as possible in the air rather than in the dielectric, while maintaining the mechanical strength of the entire structure in view of its exploitation for wearable applications.
Specifically, the performance of a GCPW has been initially analyzed without etchings, with rectangular etchings, or with rounded trapezoidal shape etchings, as shown in
Fig. *22* (a), (b), (c), respectively.

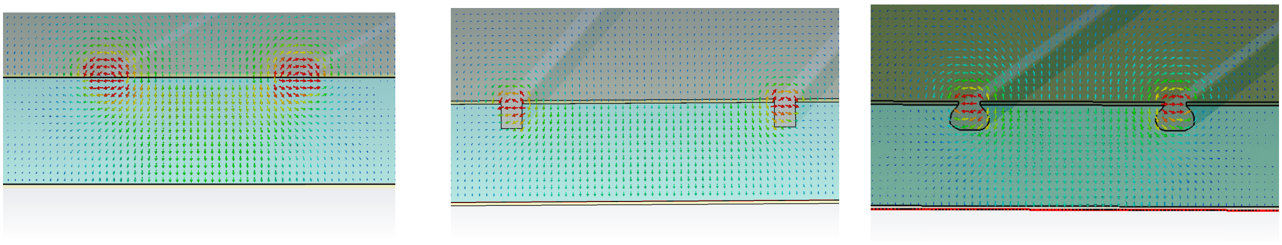
(a) (b) (c)

Fig. 22. Transversal sections of the simulated GCPW (a) without etchings, (b) with rectangular etchings, and (c) rounded trapezoidal etchings. The arrows represent the electric field intensity from the feeding line to the ground planes (coplanaron the top and at the bottom of the substrate); colours represent the electric field intensity (decreasing from red to blue): it is stronger between the line and the coplanar ground (red arrows) and weaker between the line and the bottom ground.

In Fig. 23, the $|S_{12}|$ curves of the simulated structures are compared, and it can be appreciated that, in general, substrate etchings allow to reduce the dielectric losses affecting the wave propagation; in particular, it results that the rectangular shape is the most advantageous at higher frequencies.

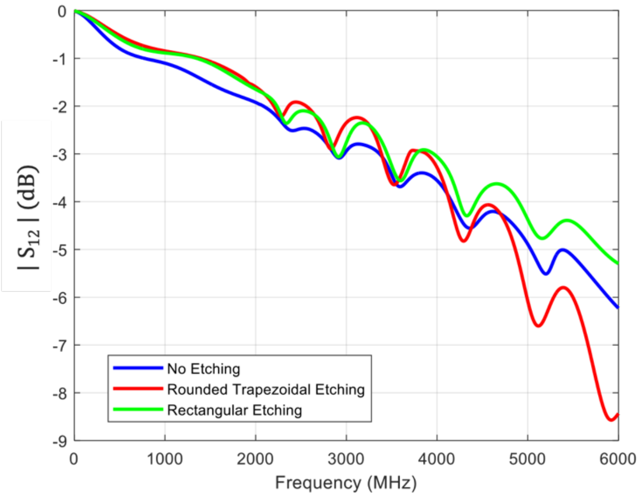

Fig. 23. Comparison between |S_{12}| curves of the simulated GCPW without etchings, with rectangular etchings, and with rounded trapezoidal shape etchings.

The results obtained until now show that the edge of the GCPW is the region where the current and the EM field are mainly concentrated; thus, removing the material under the edges can further reduce the dielectric losses, since very little field would penetrate the substrate.

In first place, a GCPW with triangular substrate etchings has been simulated, removing part of the substrate below the edges of both the line and the coplanar ground, Fig. 24 (a) and (b), and trapezoidal shape etchings with edge suspended, Fig. 24 (c).

The |S_{12}| curves obtained by simulating these structures are shown in Fig. 25 and are compared to the GCPW without etchings.

The best performance is obtained by the trapezoidal shape etchings with suspended edges shown in Fig. 24 (c), because of the removal of a larger part of substrate where the electric field intensity is stronger. In addition, it can be appreciated that GCPW with edge suspended leads to far better performance even compared to the structures previously simulated (
Fig. *22*).

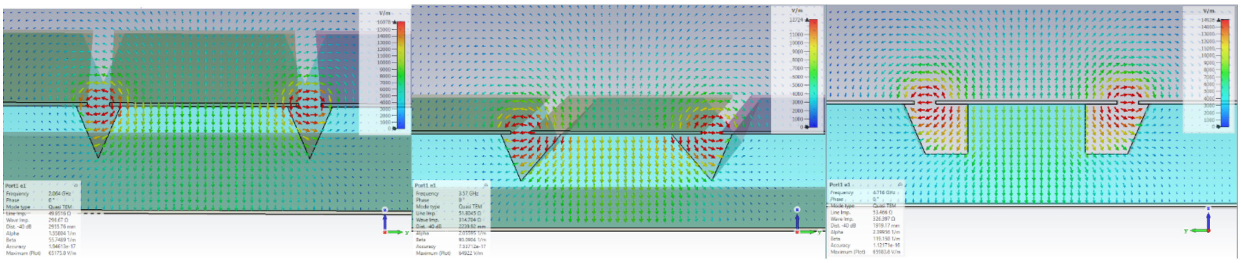
(a) (b) (c)

Fig. 24. Different simulated shapes of edge suspended GCPW with slots performed in the aperture between the signal line and the coplanar ground: (a) isosceles triangle, (b) triangle with enlarged basis toward the signal line center, and (c) and trapezoidal shape.

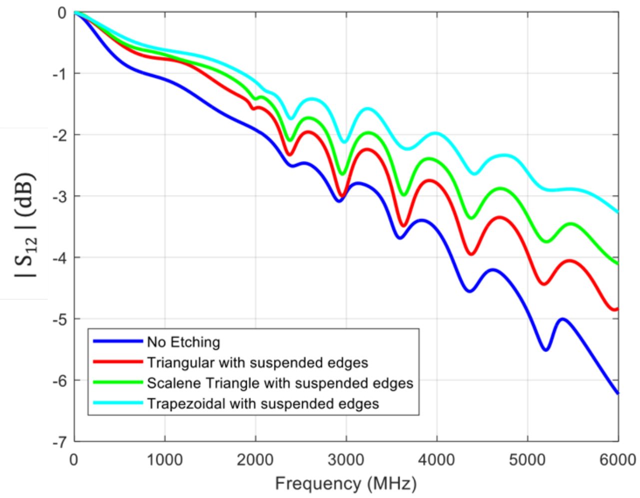

Fig. 25. |S_{12}| curves corresponding to the edge suspended GCPW with different etching shapes shown in Fig. 24, compared to the |S_{12}| curve of the simple GCPW without etchings.

Since the field penetrating the substrate is still strong below the signal line, increasing the substrate thickness from 0.93 mm to 5 mm, allows to reduce the influence of the ground at the bottom of the structure.

The new dimensions of the signal line and the gap which correspond to a characteristic impedance of 50 Ω with a substrate thickness of 5 mm are: w_m = 3.1 mm (microstrip width), G_p= 0.2 mm (gap width between the signal line and the coplanar ground).

In order to compare the effects of the substrate thickness, new shapes of the etchings have been designed and simulated with the aim of finding the optimum shape, providing the best performance; the new simulated structures on a substrate with thickness of 5 mm are shown in Fig. 26.

The comparison between the |S_{12}| curves of the GCPWs with increased substrate thickness (h_s = 5 mm) and the curve of the best etching shape layout obtained by the previous analysis (h_s = 0.93 mm) is shown in Fig. 27 (a), whereas in Fig. 27 (b) and (c) are reported the phase of the S_{12} curves, and the |S_{11}| curves of the simulated structures illustrated in Fig. 26.

Observing Fig. 27 (a) it can be noticed that there are no great differences with respect to the previous results and that the structure showing the best performance is the one with trapezoidal shape etchings and a hole below the hot conductor (Fig. 26 (c)), because the substrate has been etched exactly where the q-TEM electric field is stronger.

Another interesting observation is that the substrate layer kept below the copper edge allows to have higher robustness to the structure without affecting the overall performance.

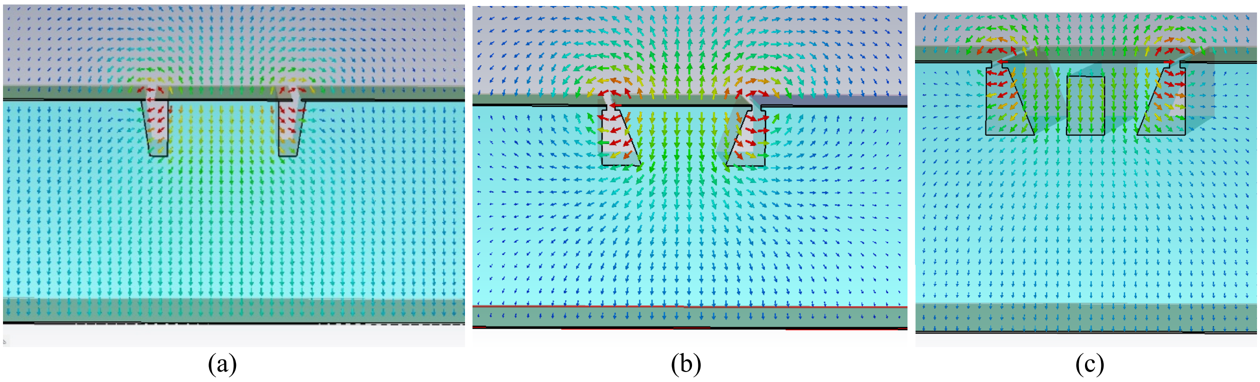

(a) (b) (c)

Fig. 26. Transversal section of the analyzed structures with substrate thickness of 5 mm: (a) trapezoidal-shape etchings; (b) trapezoidal etching shape with reinforced signal line edges, i.e., a thin substrate layer is kept below the signal line to

have a more robust structure; (c) the same structure of (b) but with an additional substrate hole just below the signal line.

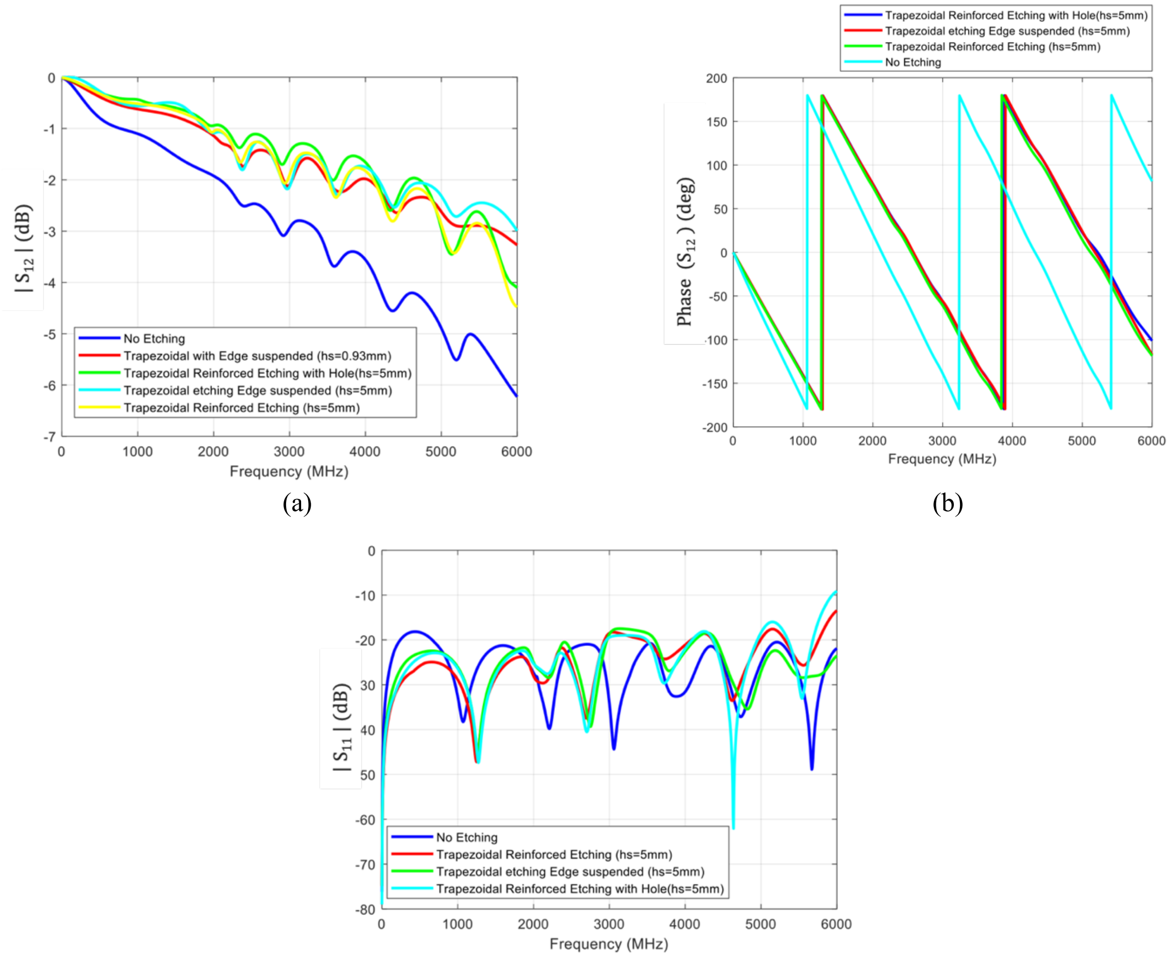

(a) (b)

(c)

Fig. 27. Comparison of (a) the |S_{12}| curves obtained by simulating the structure without any type of material removal, the structure in Fig. 24 (c) providing the best result with h_s = 0.93 mm, the one in Fig. 26 (a), the one in Fig. 26 (b) and the one in Fig. 26 (c); (b) phase of the S_{12} and |S_{11}| curves corresponding respectively to structures in Fig. 26 and the GCPW without etchings.

After removing the ground plane from below the structure, as depicted in Fig. 28, it is possible to notice how much it affects the CPW propagation.
As can be noticed from Fig. 29, the presence of the shielding ground below the structure doesn't affect too much the line performances; in fact, in the frequency range 0 ÷ 2 GHz the performance is essentially the same, then there is a slight improvement in between 2 ÷ 4 GHz, whereas there is a far worse behavior in the frequency range 4 ÷ 6 GHz.

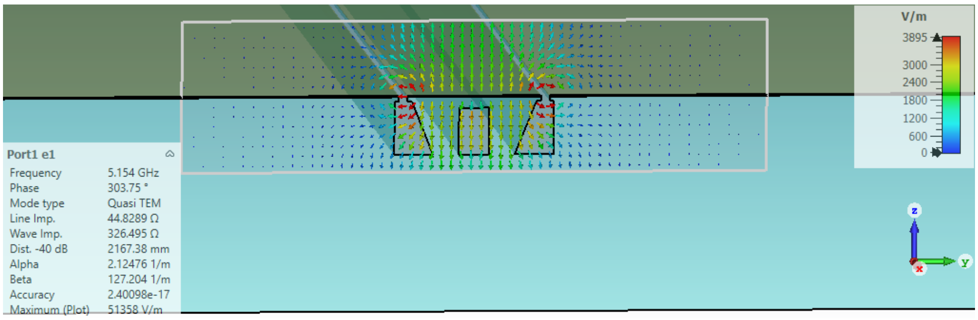

Port1 e1
Frequency 5.154 GHz
Phase 303.75 °
Mode type Quasi TEM
Line Imp. 44.8289 Ω
Wave Imp. 326.495 Ω
Dist. -40 dB 2167.38 mm
Alpha 2.12476 1/m
Beta 127.204 1/m
Accuracy 2.40098e-17
Maximum (Plot) 51358 V/m

Fig. 28. Transversal section of a CPW with trapezoidal reinforced etchings and hole below the hot conductor (without the presence of ground plane).

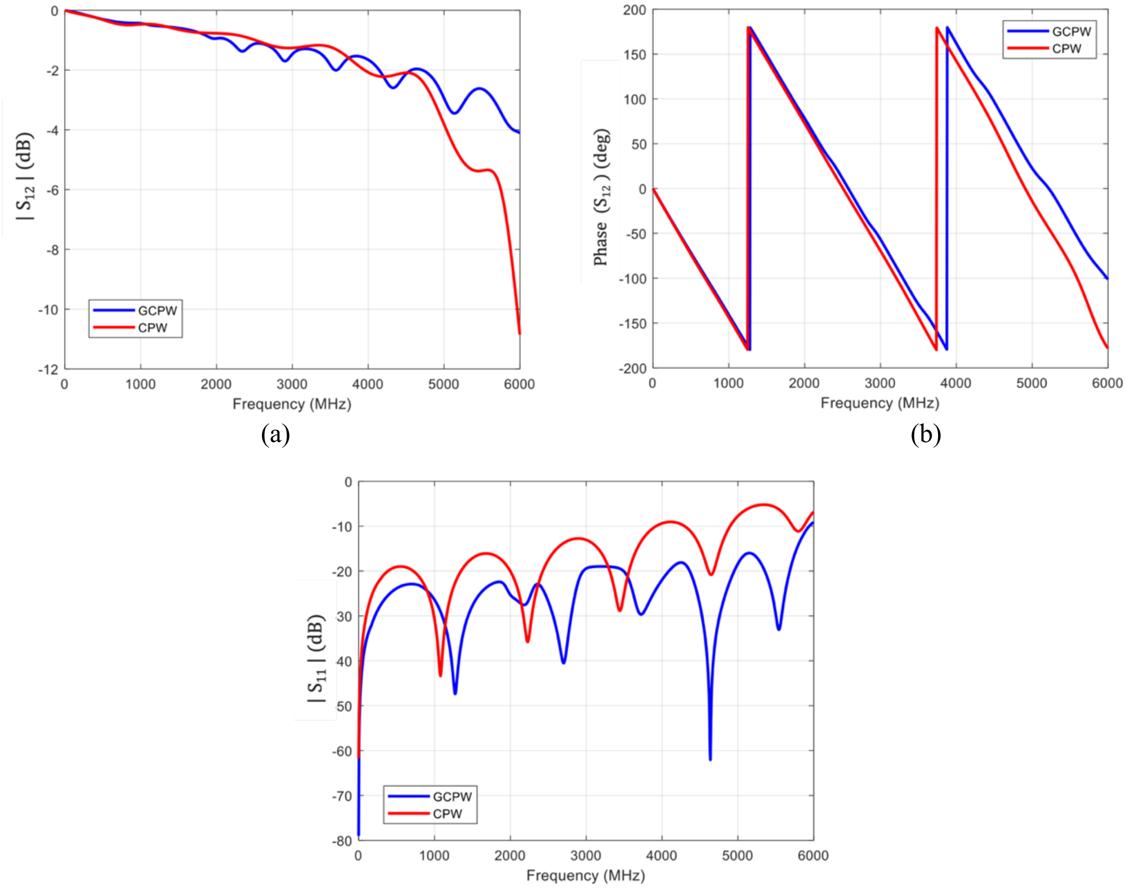

(a) (b)

(c)

Fig. 29. Comparison between the (a)|S_{12}|, (b) phase of S_{12}, (c) |S_{11}| curves of the GCPW illustrated in Fig. 26 (c), and the same structure to which the ground has been removed.

In order to have etching dimensions compatible with the real resolution of the 3D printer used for producing this substrate, the Formlabs Form 3, the dimensions of the substrate etchings have been modified in order to be compliant with it and a piece of Flexible80A with 5 mm of thickness and dimensions 100 x 100 mm^2 has been printed in order to measure the GCPW with and without etchings and compare the measurement to the simulations.

In Fig. 30 are shown the CST layout of the GCPW with rectangular and reinforced etchings in the gaps adjacent to the hot conductor and the same structure realized on Flexible80A and copper tape of thickness 32 µm.

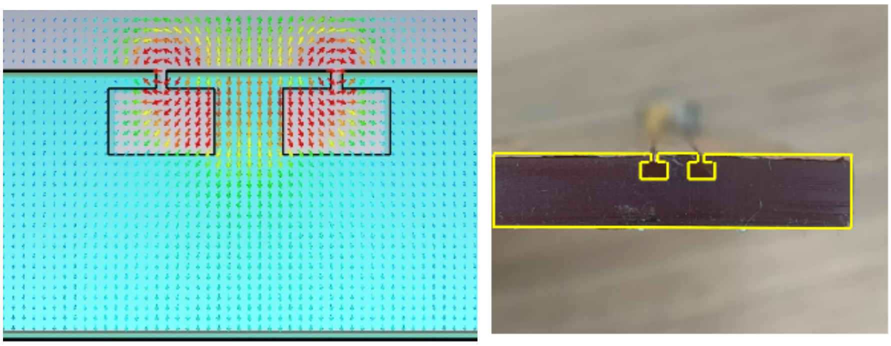

(a) (b)

Fig. 30. (a) CST layout and (b) realized prototype of the GCPW realized with rectangular etchings.

Fig. 31 shows the comparison between the measured and simulated magnitude of the $|S_{12}|$ parameters of the two different GCPWs, one without etchings in the gaps between the line and the coplanar ground, the other with rectangular shape etchings.

Both simulations and measurements demonstrate that the rectangular excavations provide great benefits reducing the losses especially at higher frequencies.

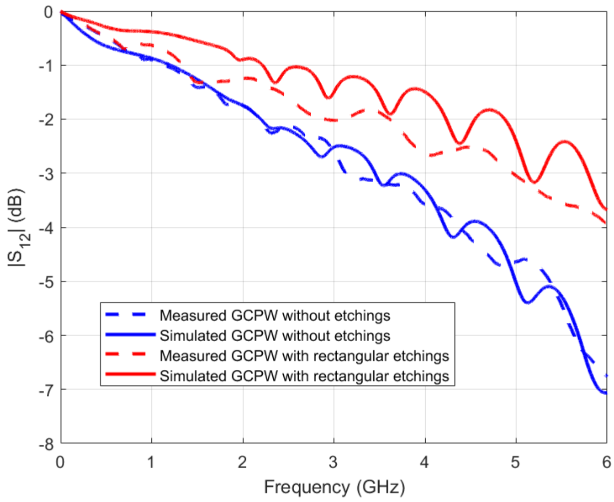

Fig. 31. Comparison between the measured and simulated $|S_{12}|$ curves of the GCPWs with and without substrate rectangular etchings.

5. DESIGN OF A WEARABLE PLANAR RECTENNA ON FLEXIBLE80A FOR WPT APPLICATIONS

Taking into account the analysis on the reduction of the substrate losses presented up to this point, a miniaturized 2.45-GHz rectenna on Flexible80A has been designed, simulated and then realized, proving that the design freedom enabled by 3D-printing allows to use low-cost dielectric material, even with poor EM properties, to realize wearable nodes that can be activated wirelessly.

To begin with, within this chapter, the process which has led to the final antenna topology is illustrated and motivated. Being the antenna meant to be wearable, a planar patch antenna has been chosen with ground below the dielectric substrate in order to have a directional radiation pattern, thus protecting the skin from radiation and avoiding the alteration of the patch performance due to skin conductivity.

The main goal in doing this, was the maximization of the antenna performance, namely in terms of realized gain and radiation efficiency, taking advantage of the design freedom provided by 3D-printing: in fact, the etching techniques discussed in the previous chapter have been considered to customize the substrate, as well as the choice of using a GCPW technology for the feeding transmission line, in order to reduce as much as possible the influence of dielectric losses in the antenna performance, being the Flexible80A a particularly lossy substrate. Moreover, in order to minimize the antenna dimensions, a shorting plate of copper has been used to connect the top side of the patch to the ground plane placed at the bottom of the structure. This technique allows to significantly reduce the patch dimensions (about 50%).

To follow, the designed patch antenna has been used for the realization of a wearable planar rectenna for WPT applications. Even in this case, with the aim of overcoming the dielectric losses, two rectenna designs are compared: one adopting a hybrid matching network composed of distributed components in GCPW technology and a lumped component (a capacitor) between the designed antenna and the rectifier, the other realizing a direct conjugate matching between the two, by varying the antenna input port impedance.

The simulations of the patch antenna have been carried out on CST Microwave Studio by means of an Electromagnetic analysis in the frequency range 0÷2 GHz if operating at 868 MHz and in the range 1÷4 GHz if operating at 2.45 GHz. The definitive antenna design has been simulated up to 10 GHz in order to know its EM behavior even at higher harmonics and then exported as a touchstone file on ADS Keysight where the overall rectenna has been simulated and optimized by means of a nonlinear Harmonic Balance analysis up to the 8th order harmonic.

Finally, the rectenna (with the antenna conjugate-matched to the rectifier) has been realized on a 3D-printed sample of Flexible80A with adhesive copper as conductor material and measured to validate the results obtained from simulations.

5.1. PATCH ANTENNA DESIGN

5.1.1. MICROSTRIP PATCH ANTENNA ON FLEXIBLE80A

To have a first rough idea of the radiation performances that can be achieved designing an antenna resonating at 868 MHz on this kind of lossy substrate, the simplest kind of antenna topology has been simulated: a microstrip patch antenna, as illustrated in Fig. 32.

The substrate material has been defined on CST at the operating frequency of by means of the EM properties obtained with the material characterization previously described, thus with $\varepsilon_r = 2.7$ and $tan\delta = 0.11$.

From patch antenna theory is acknowledged that the higher the substrate, the more the fringing effect of the electric field is emphasized, thus enhancing the radiating behavior of the planar structure. Therefore, the substrate thickness has been selected in order to be high enough to use the planar structure as a radiating antenna but also in order to maintain the flexibility enabled by this particular substrate material.

The patch dimensions have been calculated in order to have it resonating at the operating frequency of 868 MHz, using the well-known formula for rectangular patches:

$$\mathbf{L} = \frac{\boldsymbol{\lambda_0}}{\mathbf{2}\sqrt{\boldsymbol{\varepsilon_r}}} \tag{46}$$

where L is the length of the patch which, in this case, being the patch squared, is equal to the patch width W, λ_0 is the free space wavelength corresponding to 868 MHz, and ε_r is the relative dielectric permittivity of the substrate. Since, because of the fringing effect, the patch has two radiating slots of dimension ΔL in correspondence of the radiating sides, the effective length of the patch reported in TABLE II is slightly larger than the one obtained from expression (46), thus:

$$\mathbf{L} = \frac{\boldsymbol{\lambda_0}}{\mathbf{0.48}\sqrt{\boldsymbol{\varepsilon_r}}} \tag{47}$$

The feeding transmission line width (w_m) has been calculated in order to have the typical 50 Ω characteristic impedance, e.g., w_m=5.2 mm.

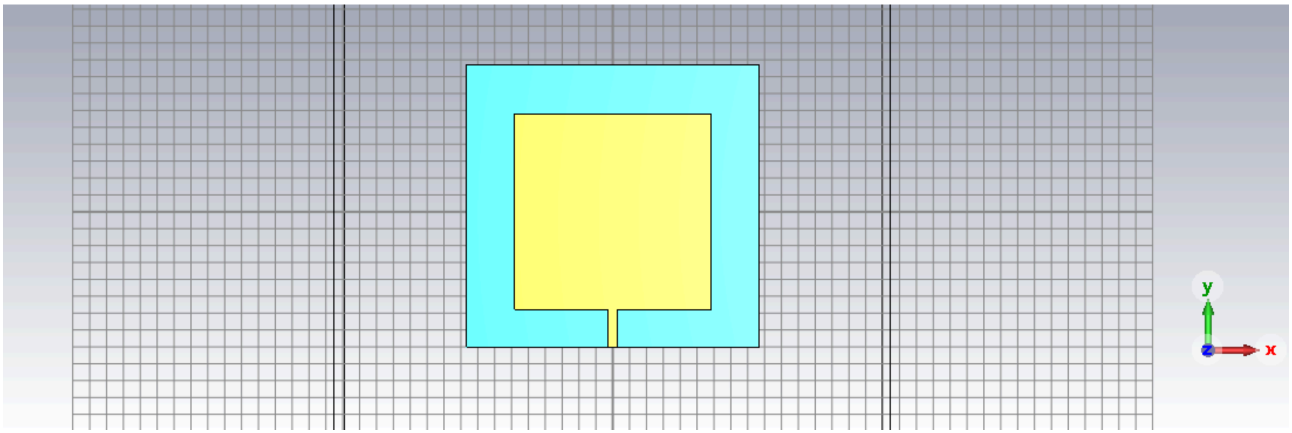

Fig. 32. Microstrip patch antenna of dimensions 116 x 116 mm^2: front view.

TABLE II. MICROSTRIP PATCH ANTENNA GEOMETRICAL DIMENSIONS

Antenna Design Parameters	
Description	***Value***
Substrate Height	2 mm
Copper thickness	31.8 µm
Patch length	116 mm
Patch width	116 mm
Microstrip width	2.4 mm

The simulation results for the abovementioned antenna are presented in the following figures:

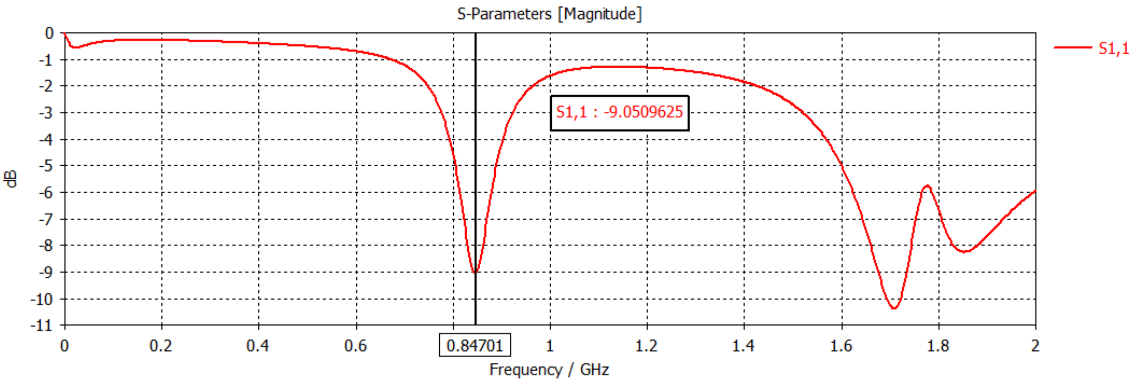

Fig. 33. S_{11} parameter of the microstrip patch antenna.

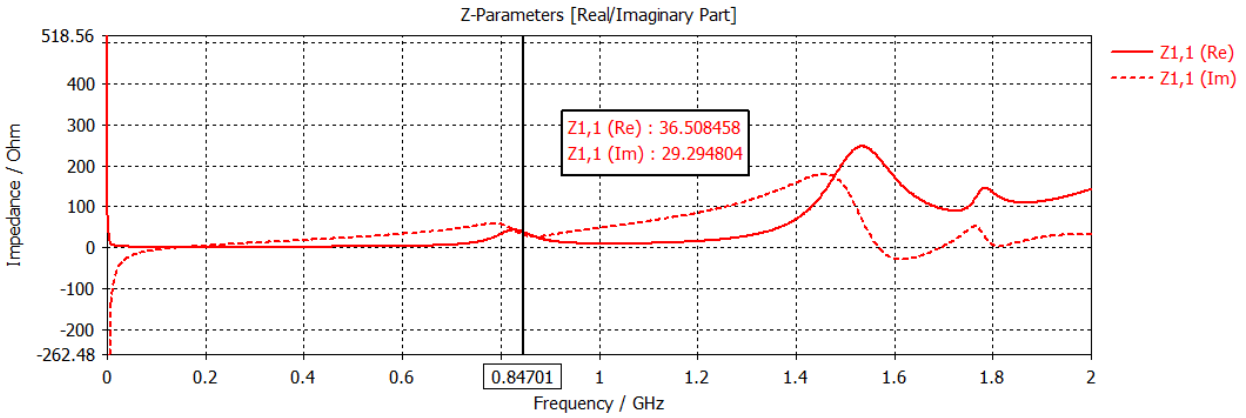

Fig. 34. Input impedance Z_{11} of the microstrip patch antenna.

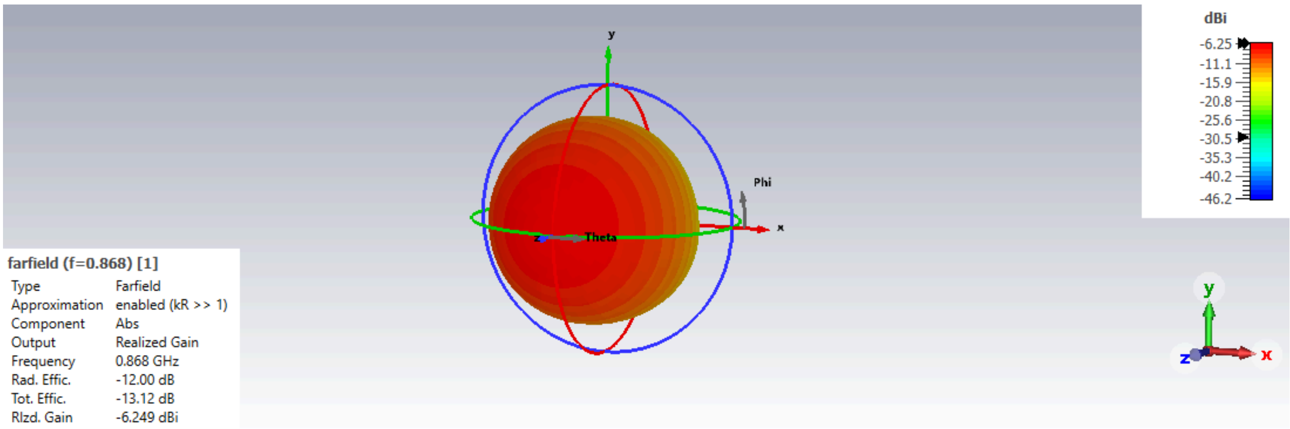

farfield (f=0.868) [1]

Type	Farfield
Approximation	enabled (kR >> 1)
Component	Abs
Output	Realized Gain
Frequency	0.868 GHz
Rad. Effic.	-12.00 dB
Tot. Effic.	-13.12 dB
Rlzd. Gain	-6.249 dBi

Fig. 35. Radiation pattern of the microstrip patch antenna.

TABLE III. MICROSTRIP PATCH ANTENNA PERFORMANCE

Microstrip Patch Antenna Performance at 868 MHz	
Description	***Value***
Realized Gain	–6.25 dBi
Radiation Efficiency	6.3%
Total Efficiency	4.8%

In TABLE III is reported the simulated antenna radiation performances in terms of realized gain, radiation efficiency and total efficiency. These quantities are computed by CST MS in the following way, as described in the CST Studio help page [34], [35]:

$$\boldsymbol{Realized\ Gain = G(\theta,\varphi) = 4\pi \frac{Power\ Radiated\ per\ unit\ solid\ angle}{Stimulated\ Power}} \quad (48)$$

where the Power Stimulated is calculated from the power that is delivered by the signal generator to the port, the Radiated Power is the power accepted by the antenna structure (Outgoing Power due to mismatch at the antenna port subtracted to the Stimulated Power) subtracted of all the losses due to dielectric materials and metals. Fig. 36 summarizes lucidly the CST power view.

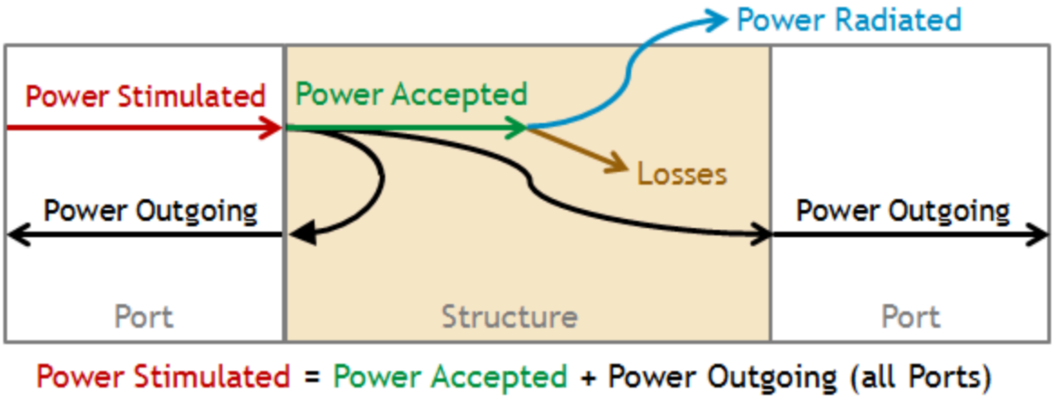

Fig. 36. CST power view [35].

The radiation efficiency is evaluated as the ratio between the Power Radiated and the Power Accepted, mainly considering the losses due to dielectrics and metals, whereas the total efficiency takes into account also the mismatch at the antenna port, thus, the ratio between the Power Radiated and the Power Stimulated. This means that these two quantities are equal only in the case of antenna perfect matching conditions.

Finally, observing TABLE III, it can be concluded that the antenna has very poor radiation capabilities, and this is mostly caused by the very high lossy substrate.

To improve the antenna radiation performance as much as possible, the innovative and creative etching techniques described and validated in the previous chapters have been exploited in order to overcome the great losses intrinsic to the dielectric material.

5.1.2. COPLANAR-FED PATCH ANTENNA ON ETCHED SUBSTRATE

The present antenna configuration, Fig. 37, has been designed with the goal of improving the overall radiation performances of the microstrip patch antenna. In fact, the antenna radiation efficiency and gain have resulted to be deeply affected by the very high loss tangent of the Flexible80A dielectric substrate, $tan\delta = 0.11$.

From the detailed analysis presented in Chapter 4, it has been demonstrated that grounded coplanar waveguide brings benefits to the propagation performance with respect to microstrip transmission lines and performing substrate etchings in the gaps between the hot conductor and the coplanar ground can further improve it, thus, changing the EM properties of the material. In this way, the field propagates partly in the air and partly in the dielectric, reducing both the effective dielectric constant and the loss tangent of the material penetrated by the propagating electric field.

Taking advantage of these considerations, a coplanar-fed patch antenna has been designed and simulated on CST MS. The feeding transmission line is designed in GCPW technology, which means that both the gap (G_p) between the transmission line and the coplanar ground and the line width (w_m) has been chosen to ensure the typical 50 Ω characteristic impedance, thus, considering a 0.2 mm gap, and being the substrate 2-mm-thick, the 50 Ω line width results to be 3.1 mm. Substrate etchings have been performed in the slots between the gap and the line, and the shape of the etchings, shown in Fig. 38, has been chosen based on the best result obtained by the comparison illustrated in Chapter 4 (see Fig. 27 (a)).
Tapering has also been introduced in the gap between the bottom edge of the patch and the coplanar ground to realize the coplanar-microstrip transition maintaining the 50 Ω line impedance.
The coplanar ground is connected to the ground at the bottom of the structure so that them both show the same potential.

Moreover, with the aim of emphasizing the fringing effect in correspondence of the patch radiating sides, the substrate has been etched of a 0.5 mm depth all around the patch perimeter and partly below the edges, so that just a squared piece of substrate of smaller dimensions supports the patch metallization, as shown in Fig. 39.

The patch dimensions are in this case summarized in TABLE IV.

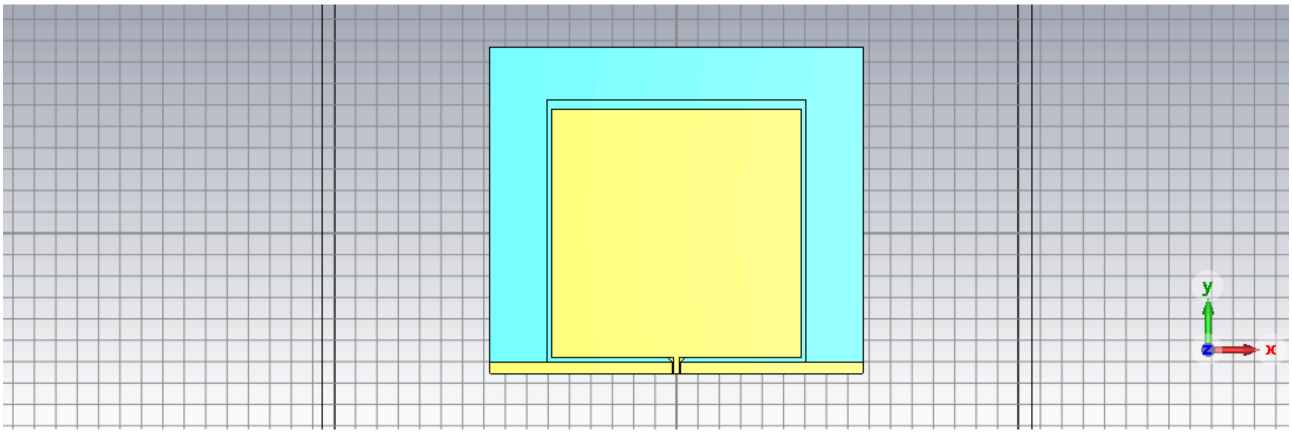

Fig. 37. Coplanar-fed patch antenna of dimensions 116 x 116 mm^2 with etched substrate: front view.

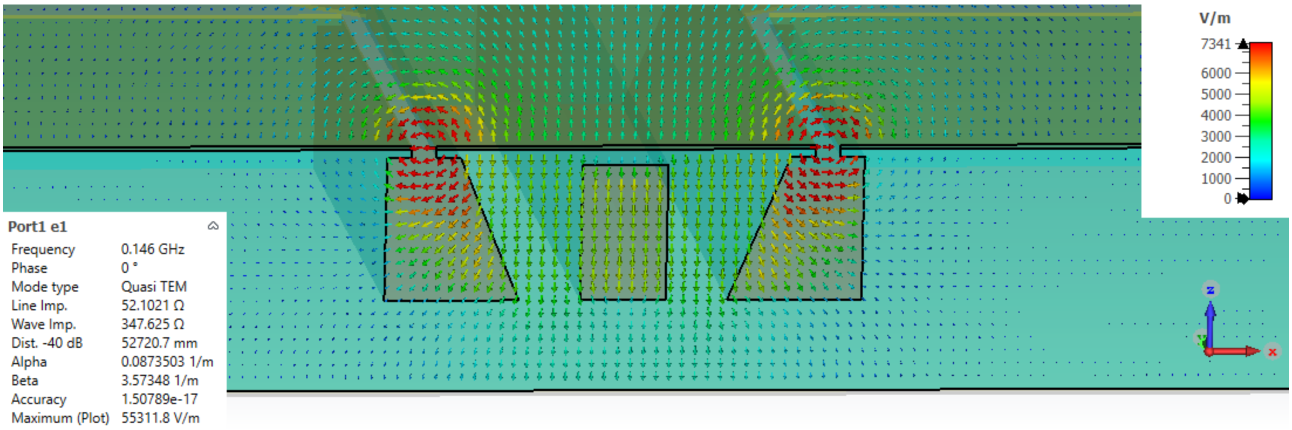

Port1 e1

Frequency	0.146 GHz
Phase	0 °
Mode type	Quasi TEM
Line Imp.	52.1021 Ω
Wave Imp.	347.625 Ω
Dist. -40 dB	52720.7 mm
Alpha	0.0873503 1/m
Beta	3.57348 1/m
Accuracy	1.50789e-17
Maximum (Plot)	55311.8 V/m

Fig. 38. Substrate etching performed in the substrate in correspondence of the gaps between the signal line and the coplanar ground.

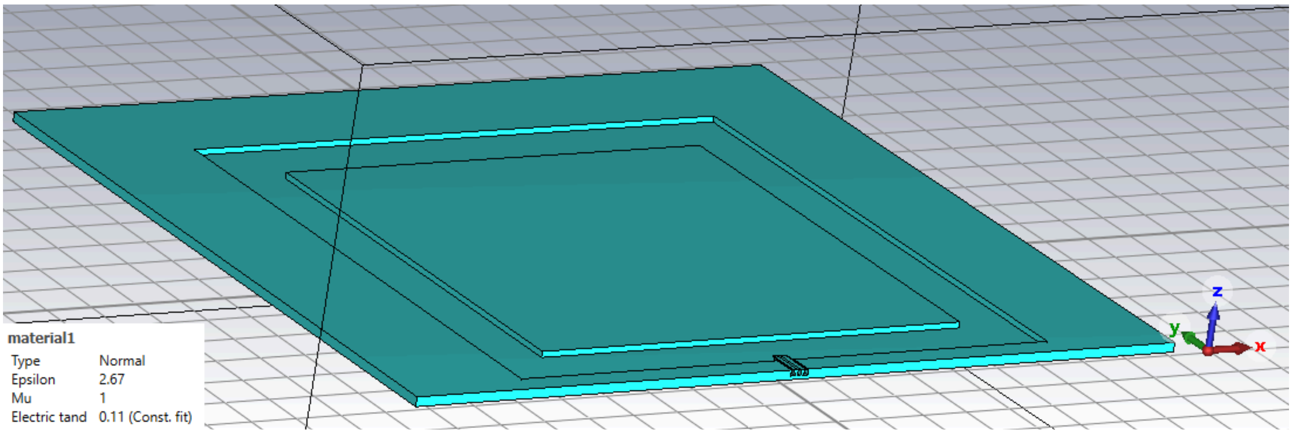

material1

Type	Normal
Epsilon	2.67
Mu	1
Electric tand	0.11 (Const. fit)

Fig. 39. Coplanar-fed patch antenna with etched substrate

TABLE IV. COPLANAR-FED PATCH ANTENNA GEOMETRICAL DIMENSIONS

Antenna Design Parameters	
Description	***Value***
Substrate Height	2 mm
Copper thickness	31.8 μm
Patch length	116 mm
Patch width	116 mm
GCPW width	3.1 mm
Gap between the transmission line and the coplanar ground	0.2 mm
Depth of the substrate etchings	0.5 mm
Width of the substrate etchings at its lateral sides and partly below its edges	12.4 mm
Width of the substrate etchings at its top side and partly below its edge	14.4 mm

The simulation results are the following:

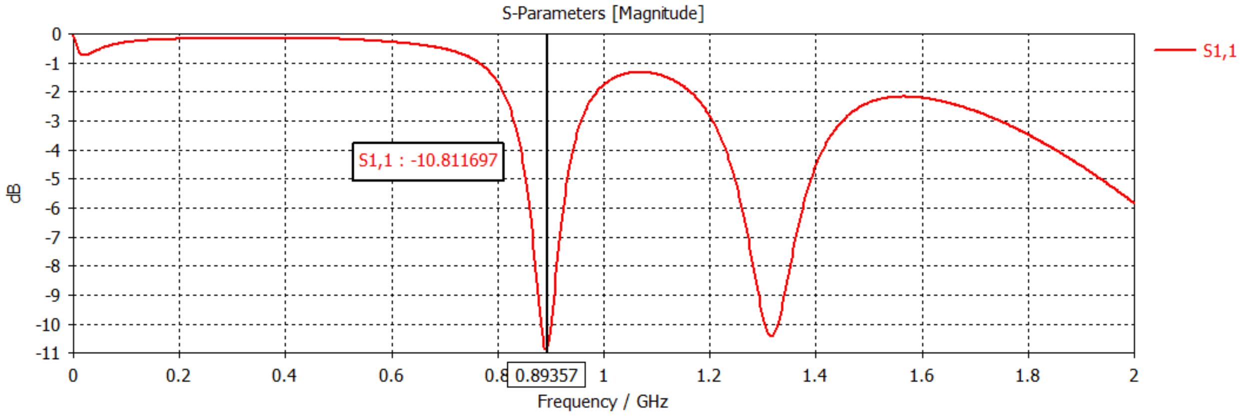

Fig. 40. S_{11} parameter of the coplanar-fed patch antenna with etched substrate.

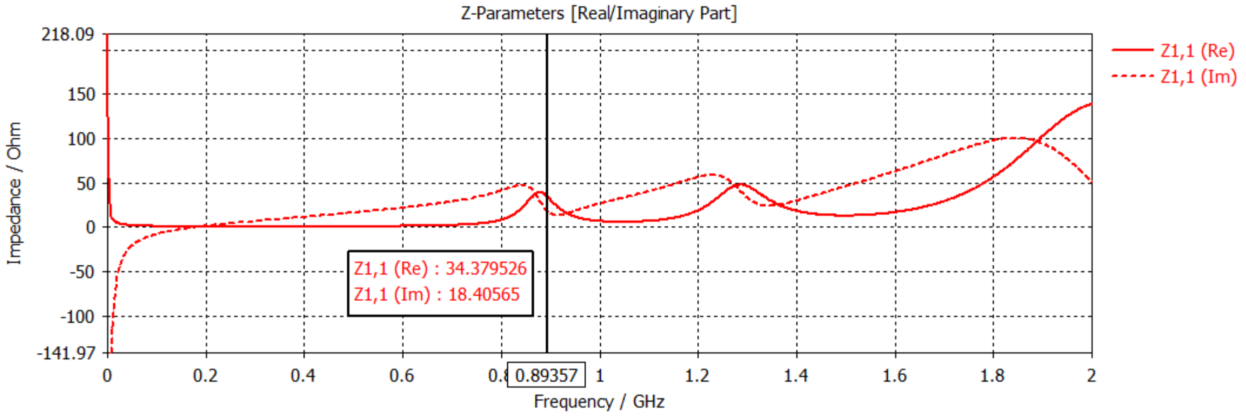

Fig. 41. Input impedance Z_{11} of the coplanar-fed patch antenna with etched substrate.

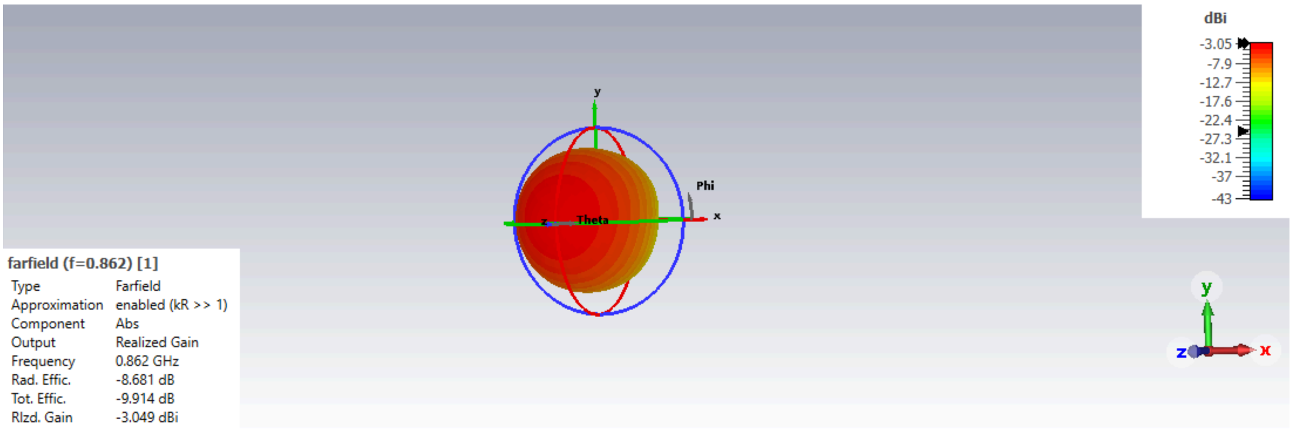

farfield (f=0.862) [1]

Type	Farfield
Approximation	enabled (kR >> 1)
Component	Abs
Output	Realized Gain
Frequency	0.862 GHz
Rad. Effic.	-8.681 dB
Tot. Effic.	-9.914 dB
Rlzd. Gain	-3.049 dBi

Fig. 42. Far-field results of the coplanar-fed patch antenna with etched substrate.

TABLE V. COPLANAR-FED PATCH ANTENNA PERFORMANCE

Coplanar Fed Patch Antenna Performance at 862 MHz	
Description	***Value***
Realized Gain	–3.05 dBi
Radiation Efficiency	13%
Total Efficiency	10%

From the simulation results summarized in TABLE V it can be observed that the expedients introduced with respect to the microstrip patch antenna configuration, has led to doubling both the realized gain and the antenna radiating efficiency.

5.1.3. COPLANAR PATCH ANTENNA WITH ETCHED SUBSTRATE

Drawing inspiration from previous works ([36], [37]), a coplanar patch antenna (CPA) has been designed with the aim of further improving the antenna radiating performance.

In [37], the CPA topology is introduced, consisting of a patch surrounded by closely-spaced ground conductor and a CPW feed line, which has similar geometric configuration as the loop slot antenna. Simulations and experiments clearly demonstrated that the CPA behaves more similarly to the microstrip patch antenna rather than a loop slot antenna, and in particular for what concerns the resonant property. Particularly, the resonant frequency of the antenna is primarily determined by the patch length (L) of about a half guided wavelength instead of the total loop size. EM simulations have also demonstrated the similar distribution of the electric fields around the slots as the distribution around the microstrip patch edges. Similar tendency of the input impedance versus the length (L) of the patch has been also observed. This makes possible to realize an impedance matching by only adjusting the width (W) of the patch.
This kind of patch antenna has more parameters to design, not only the patch dimensions but also slots between the patch and the surrounding coplanar ground.

The simulated CPA, shown in Fig. 43, has the same geometry characteristics presented for the coplanar-fed patch antenna, reported in TABLE VI and the same etchings in the gaps adjacent to the coplanar ground and in the slots surrounding the patch.

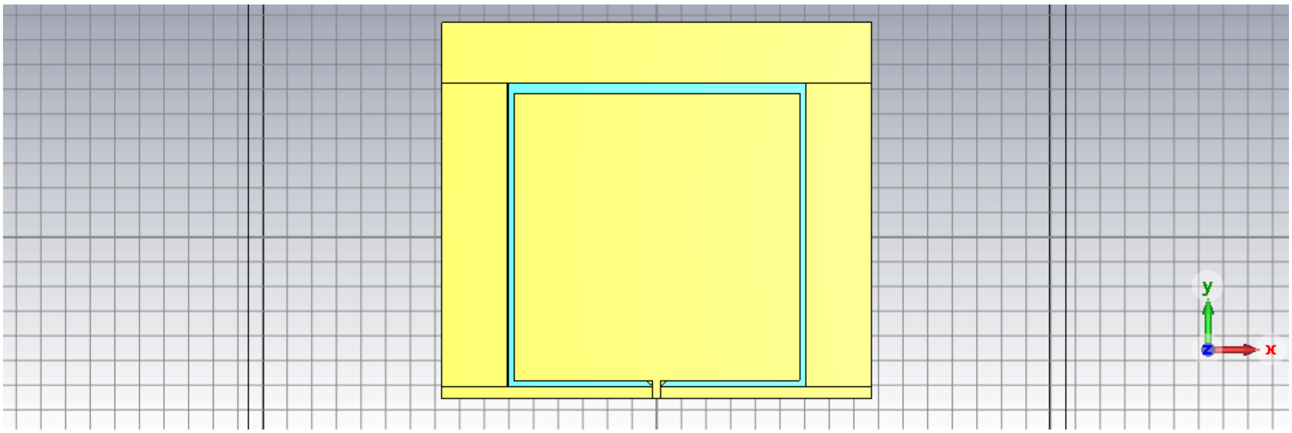

Fig. 43. Coplanar patch antenna of dimension 116 x 116 mm^2 with etched substrate: front view.

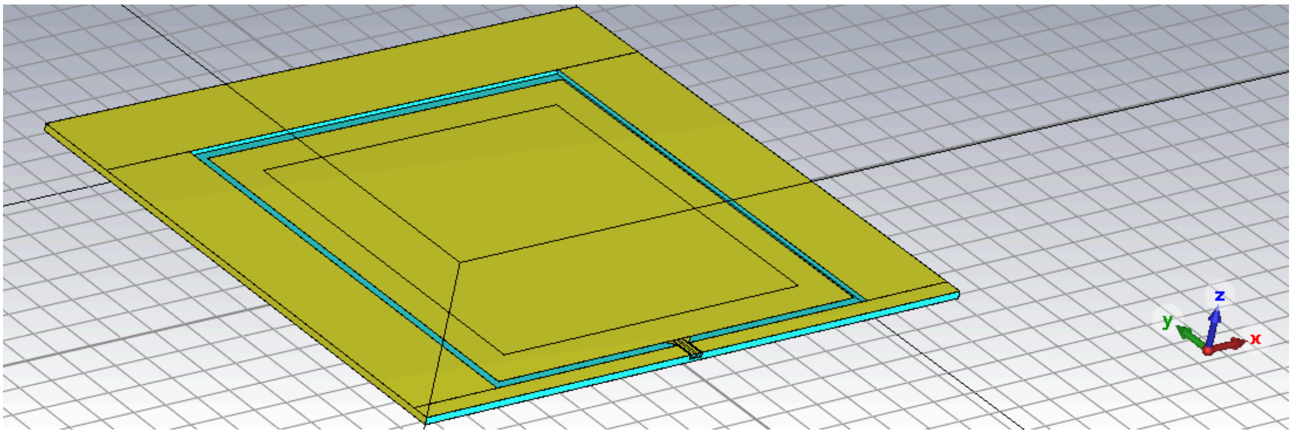

Fig. 44. Coplanar patch antenna with etched substrate: lateral view.

TABLE VI. COPLANAR PATCH ANTENNA WITH ETCHED SUBSTRATE GEOMETRICAL DIMENSIONS

Antenna Design Parameters	
Description	***Value***
Substrate Height	2 mm
Copper thickness	31.8 μm
Patch length	116 mm
Patch width	116 mm
GCPW width	3.1 mm
Gap between the transmission line and the coplanar ground	0.2 mm
Depth of the substrate etchings	0.5 mm
Width of the substrate etchings at its lateral sides and partly below its edges	12.4 mm
Width of the substrate etchings at its top side and partly below its edge	14.4 mm

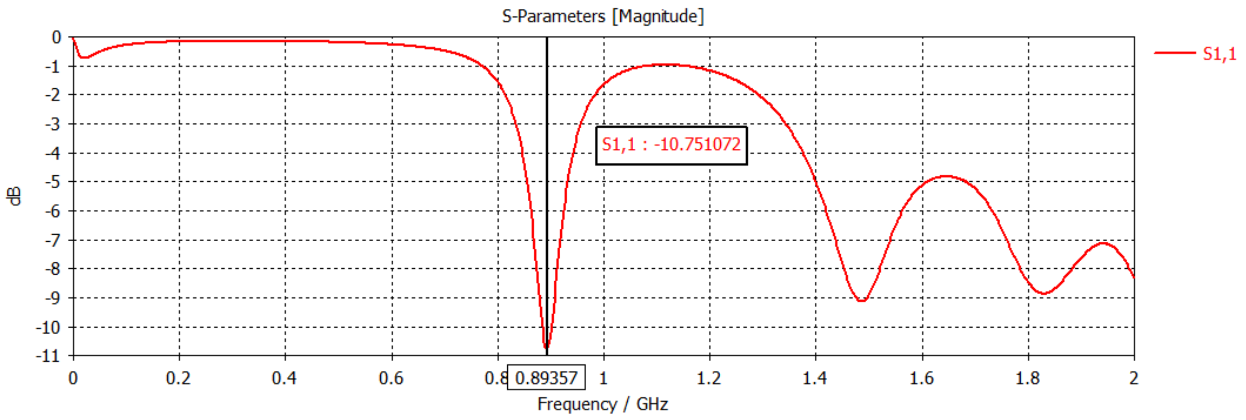

Fig. 45. S_{11} parameter of the coplanar patch antenna with etched substrate.

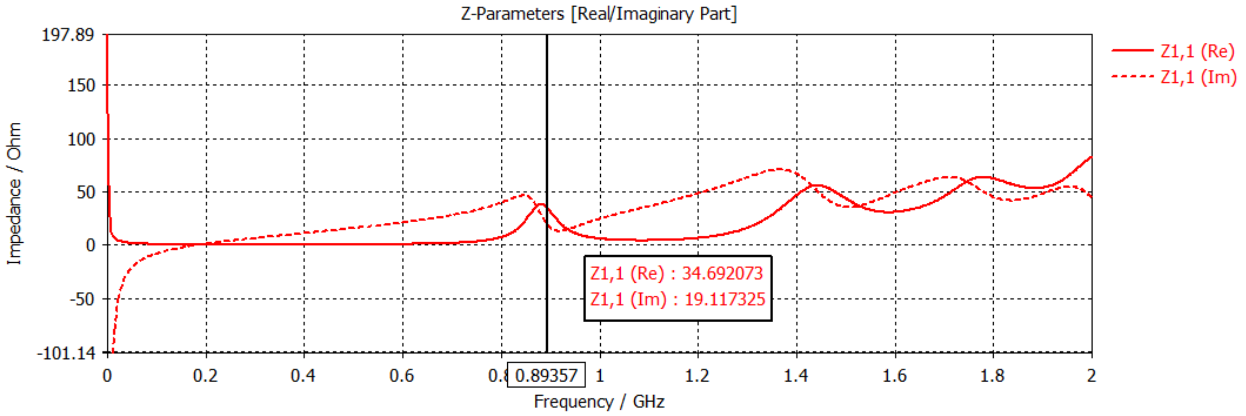

Fig. 46. Input impedance Z_{11} of the coplanar patch antenna with etched substrate.

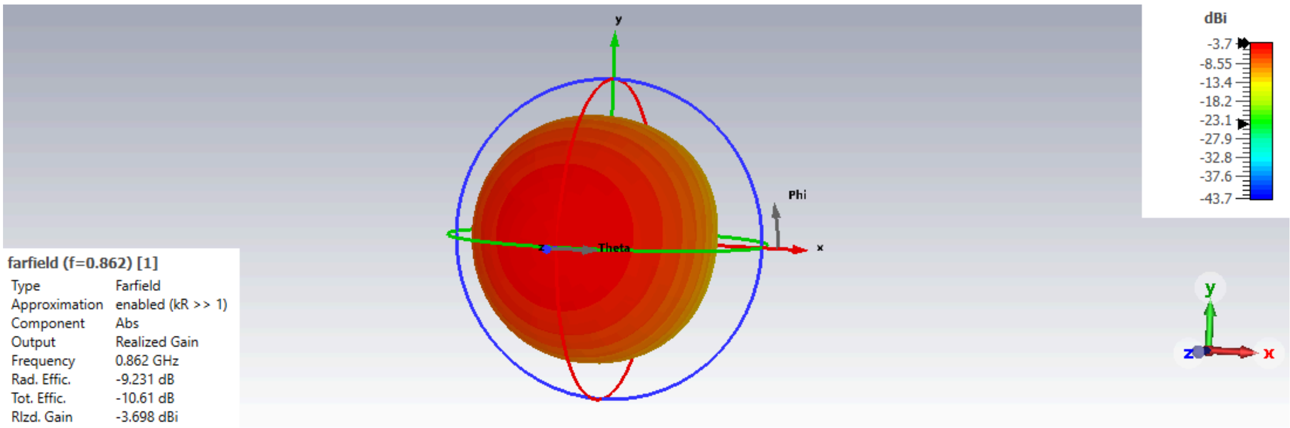

farfield (f=0.862) [1]

Type	Farfield
Approximation	enabled (kR >> 1)
Component	Abs
Output	Realized Gain
Frequency	0.862 GHz
Rad. Effic.	-9.231 dB
Tot. Effic.	-10.61 dB
Rlzd. Gain	-3.698 dBi

Fig. 47. Far-field results of the coplanar patch antenna with etched substrate.

TABLE VII. COPLANAR PATCH ANTENNA WITH ETCHED SUBSTRATE PERFORMANCE

Coplanar Patch Antenna Performance at 862 MHz	
Description	***Value***
Realized Gain	–3.70 dBi
Radiation Efficiency	11%
Total Efficiency	8.6%

The overall performance of the CPA with etched substrate is reported in TABLE VII and it can be noticed that is slightly worsened with respect to that of the coplanar-fed patch antenna, thus it can be concluded that in this particular case, having the coplanar ground closer to the patch doesn’t enhance the radiation efficiency nor the gain.

5.1.4. MINIATURIZED COPLANAR FED PATCH ANTENNA WITH ETCHED SUBSTRATE

The dimensions of the patch antennas presented up to this point is particularly large, due to the very low operating frequency of 868 MHz.

Since one of the main purposes of this thesis is to realize a wearable patch antenna on a flexible low cost and 3D-printed material to be exploited for WPT applications, is of major concern the possibility of reducing the weight and the size of the device.

To do that, a shorting plate of copper has been used to connect the top side of the patch to the ground plane placed at the bottom of the structure, allowing to reduce the patch dimensions of about 50%. Then, the patch width has been enlarged to find the 50 Ω impedance matching conditions. This matching technique is typically used in the case of coplanar fed patch antennas, as mentioned in [37].

This shrinked version of the coplanar-fed patch antenna presents similar substrate etchings to the previous antenna configurations, all around the patch perimeter and partly below its bottom edge, as clearly visible in Fig. 49 and Fig. 50. In particular, larger slots has been kept in correspondence of the radiating sides, whereas the lateral ones have been reduced. The antenna dimensions are reported in TABLE VIII.

Moreover, the shape of the etchings in the gaps between the feeding line and the coplanar ground, Fig. 51, have been modified in order to be compliant to the Formlabs Form3 3D printer, which has a 25-micron XY resolution and 25-300 microns (user-selectable) in the Z direction, using an 85-micron laser.

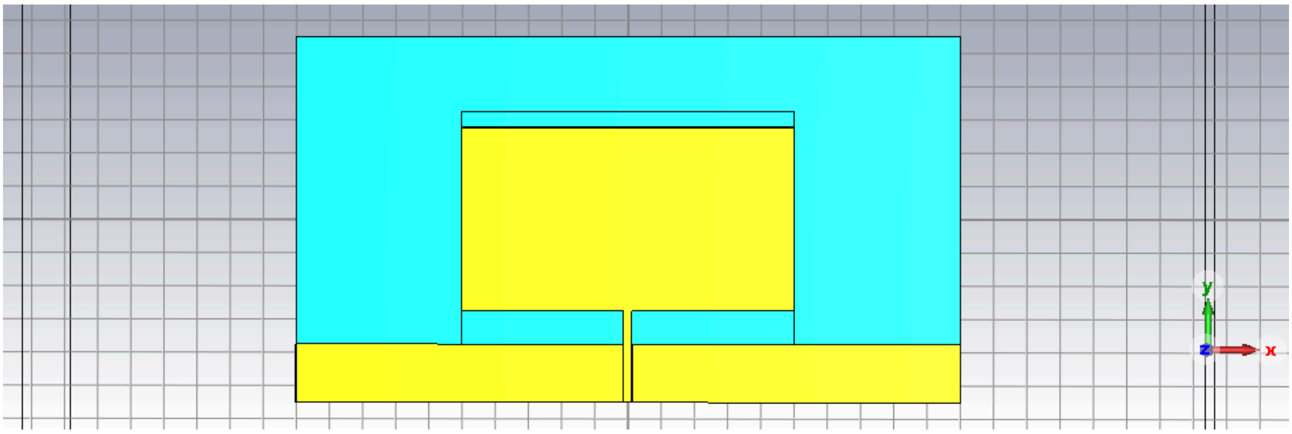

Fig. 48. Miniaturized coplanar fed patch antenna of dimensions 55 x 110 mm^2 with etched substrate: front view.

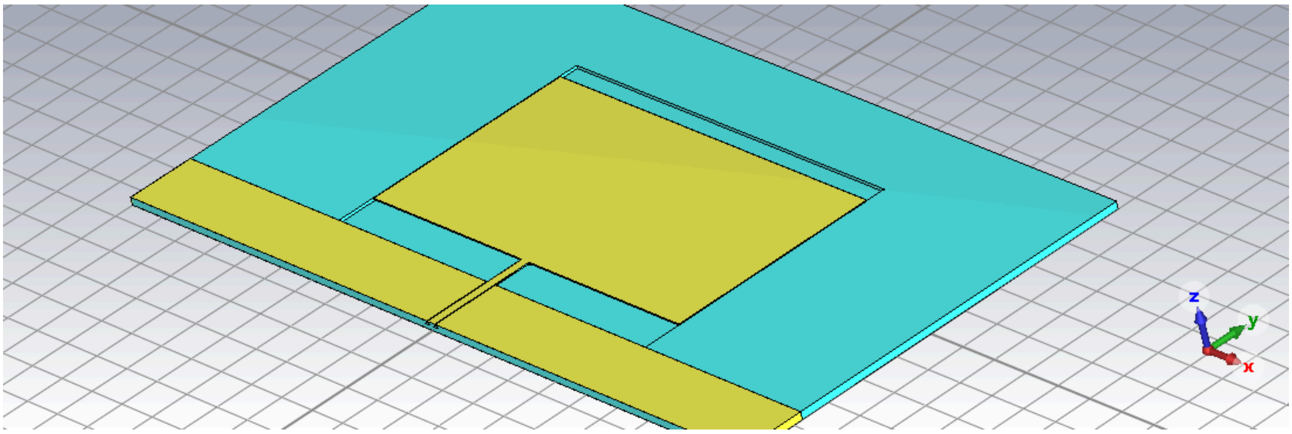

Fig. 49. Miniaturized coplanar fed patch antenna with etched substrate: lateral view.

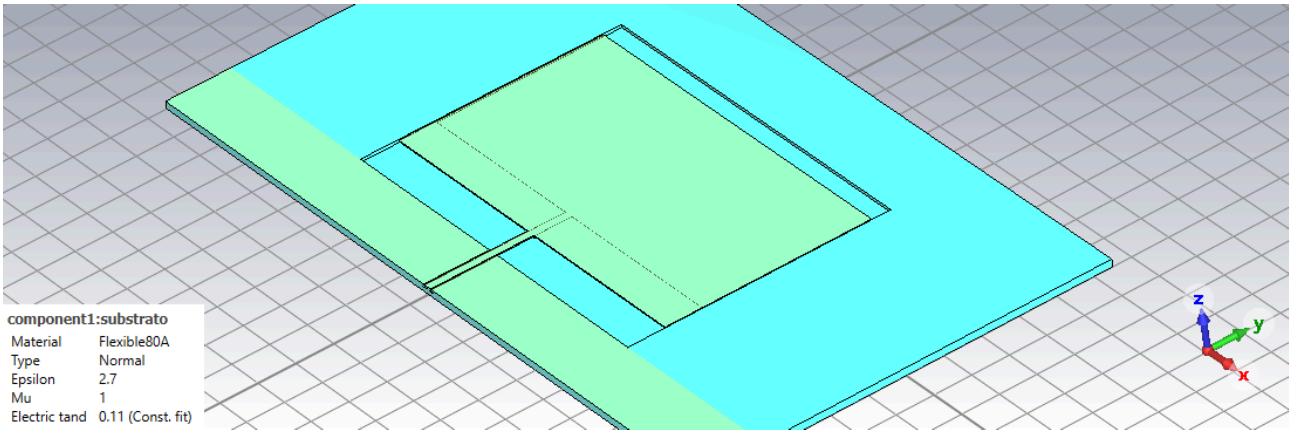

component1:substrato

Material	Flexible80A
Type	Normal
Epsilon	2.7
Mu	1
Electric tand	0.11 (Const. fit)

Fig. 50. Substrate view of the miniaturized coplanar fed patch antenna with etched substrate.

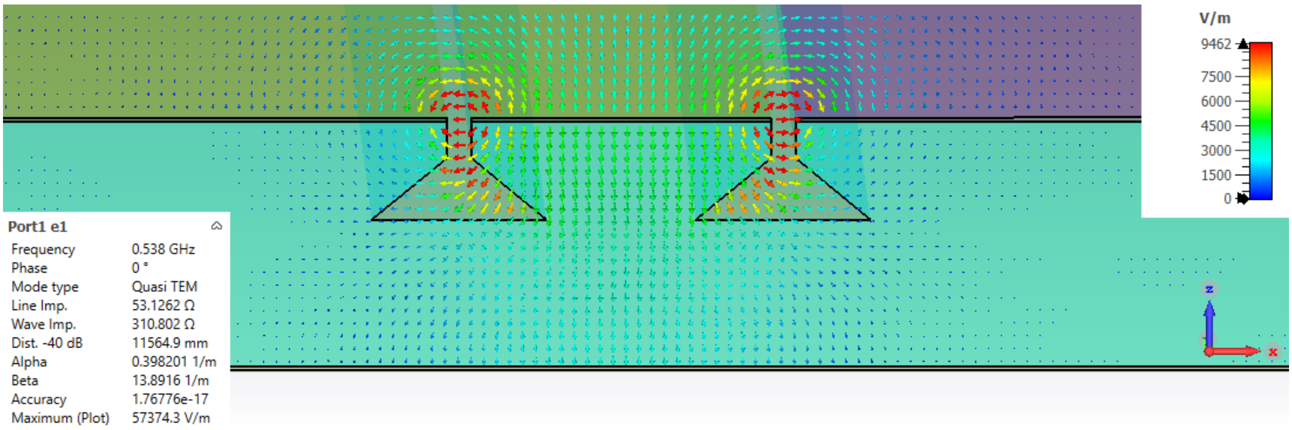

Port1 e1

Frequency	0.538 GHz
Phase	0 °
Mode type	Quasi TEM
Line Imp.	53.1262 Ω
Wave Imp.	310.802 Ω
Dist. -40 dB	11564.9 mm
Alpha	0.398201 1/m
Beta	13.8916 1/m
Accuracy	1.76776e-17
Maximum (Plot)	57374.3 V/m

Fig. 51. Substrate etching in between the feeding line and the coplanar ground.

TABLE VIII. MINIATURIZED COPLANAR-FED PATCH ANTENNA WITH ETCHED SUBSTRATE GEOMETRICAL DIMENSIONS

Antenna Design Parameters	
Description	***Value***
Substrate Height	2 mm
Copper thickness	31.8 µm
Patch length	55 mm
Patch width	110 mm
GCPW width	2.4 mm
Gap between the transmission line and the coplanar ground	0.2 mm
Depth of the substrate etchings	0.5 mm
Width of the substrate etchings at its lateral sides and partely below its edges	0.2 mm
Width of the substrate etchings at its bottom side and partly below its edge	20 mm
Width of the substrate etchings at its top side	5 mm

The simulation results are the following:

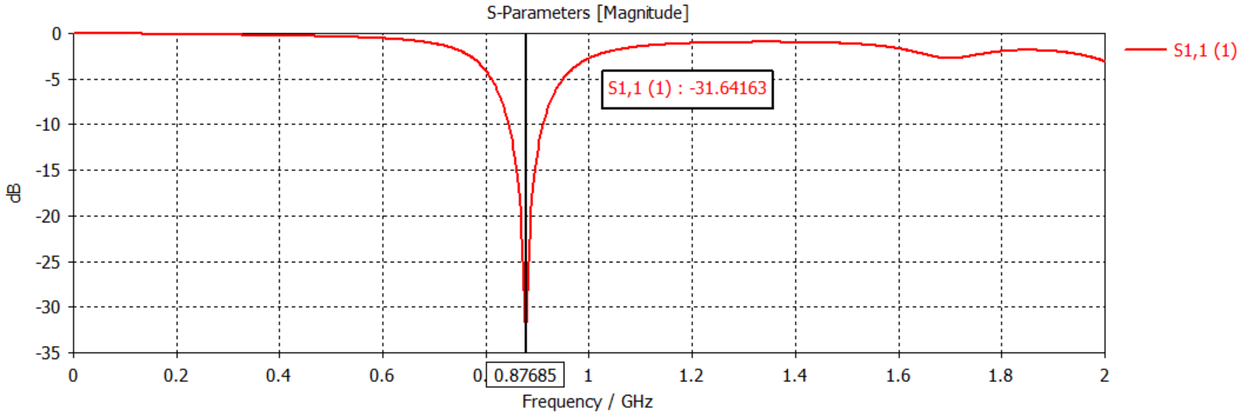

Fig. 52. |S_{11}| parameter of the miniaturized coplanar fed patch antenna with etched substrate.

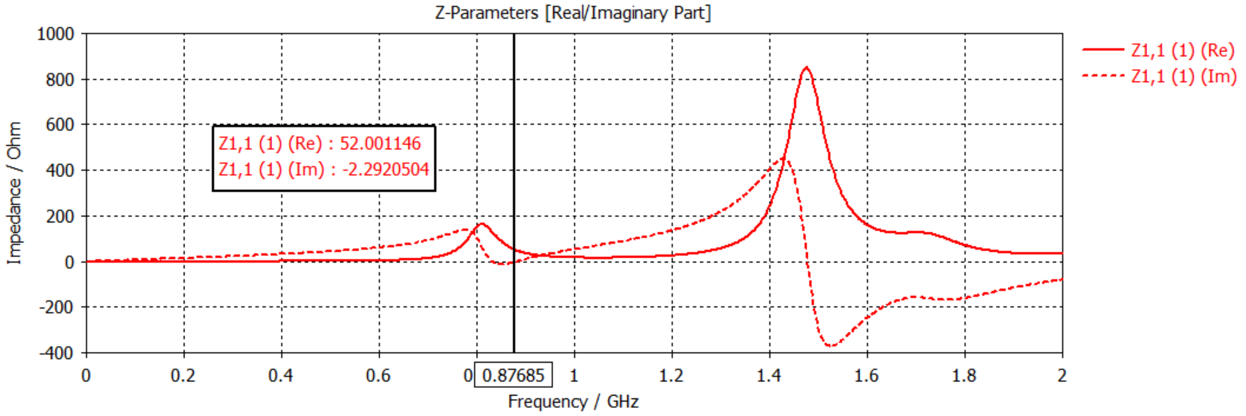

Fig. 53. Z_{11} parameter of the miniaturized coplanar fed patch antenna with etched substrate.

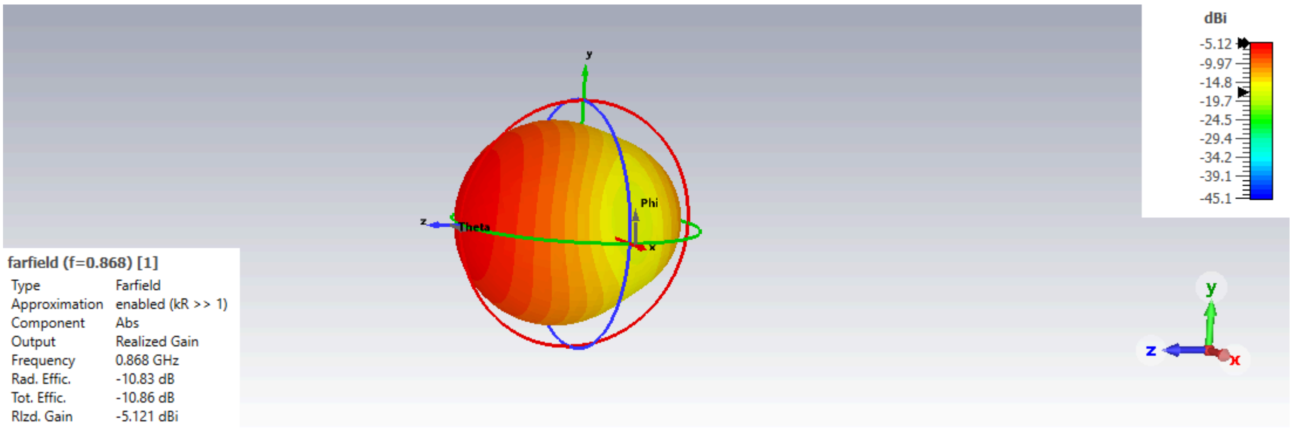

farfield (f=0.868) [1]

Type	Farfield
Approximation	enabled (kR >> 1)
Component	Abs
Output	Realized Gain
Frequency	0.868 GHz
Rad. Effic.	-10.83 dB
Tot. Effic.	-10.86 dB
Rlzd. Gain	-5.121 dBi

Fig. 54. Far-field results of the miniaturized coplanar fed patch antenna with etched substrate.

TABLE IX. MINIATURIZED COPLANAR-FED PATCH ANTENNA WITH ETCHED SUBSTRATE PERFORMANCE

Miniaturized Coplanar Fed Patch Antenna Performance at 868 MHz	
Description	***Value***
Realized Gain	–5.12 dBi
Radiation Efficiency	8.3%
Total Efficiency	8.2%

As can be derived from the far-field simulation results reported in TABLE IX, 8.3% of radiation efficiency has been achieved. This result is not so far from the ones obtained in the case of the full dimension antenna.

Then, the same antenna configuration has also been simulated, adding a coplanar ground all around the patch, realizing a miniaturized coplanar patch antenna, see Fig. 55. Even in this case, this solution doesn't improve the radiation performances, as summarized in TABLE X.

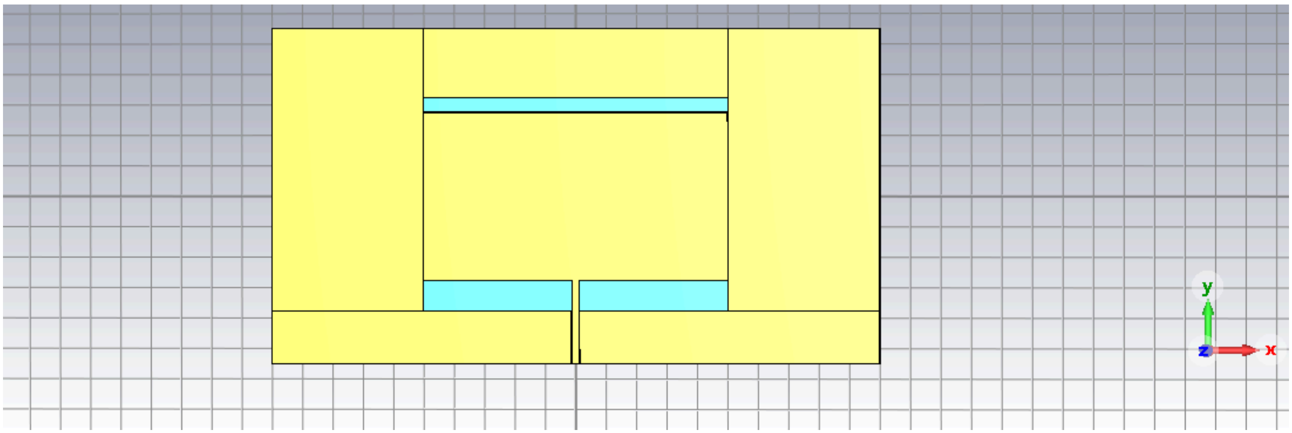

Fig. 55. Miniaturized coplanar patch antenna of dimensions 55 x 110 mm^2 with etched substrate: front view.

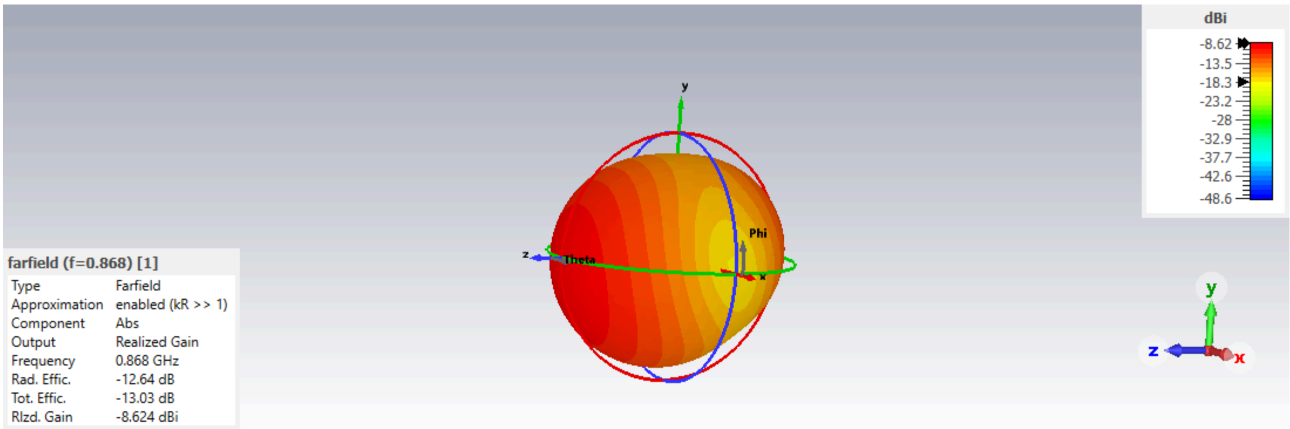

farfield (f=0.868) [1]

Type	Farfield
Approximation	enabled (kR >> 1)
Component	Abs
Output	Realized Gain
Frequency	0.868 GHz
Rad. Effic.	-12.64 dB
Tot. Effic.	-13.03 dB
Rlzd. Gain	-8.624 dBi

Fig. 56. Far-field results of the miniaturized coplanar patch antenna with etched substrate.

TABLE X. MINIATURIZED COPLANAR PATCH ANTENNA WITH ETCHED SUBSTRATE PERFORMANCE

Miniaturized Coplanar Fed Patch Antenna Performance at 868 MHz	
Description	***Value***
Realized Gain	–8.62 dBi
Radiation Efficiency	5.4%
Total Efficiency	4.9%

5.1.5. MINIATURIZED COPLANAR FED PATCH ANTENNA WITH SQUARED ETCHINGS IN THE SUBSTRATE

All the different patch antenna topologies presented up to this point have clearly demonstrated that substrate etchings bring advantages in terms of radiation efficiency.

This is confirmed by works such as the one proposed by Y. Kim and S. Lim in [7] dealing with 3D-printed substrate materials characterized by high dielectric losses (such as lossy polylactic acid, or PLA). In fact, the authors propose as 3D-printed material a non-uniform honeycomb structure in order to reduce the dielectric losses of the latter. This non-uniform honeycomb-shaped substrate is composed of large unit cells, which achieve low insertion loss (0.01 dB/mm) because of the low volume of the dielectric material. In particular, it is experimentally confirmed that the dielectric constant and dielectric losses of the material decrease for increasing honeycomb unit cell size, as shown in Fig. 57 (b). In particular, as the honeycomb unit cell size L_h increases from 3 to 12 mm, the dielectric constant ε_r of the substrate decreases from 1.5 to 1.01 (similar to that of air).

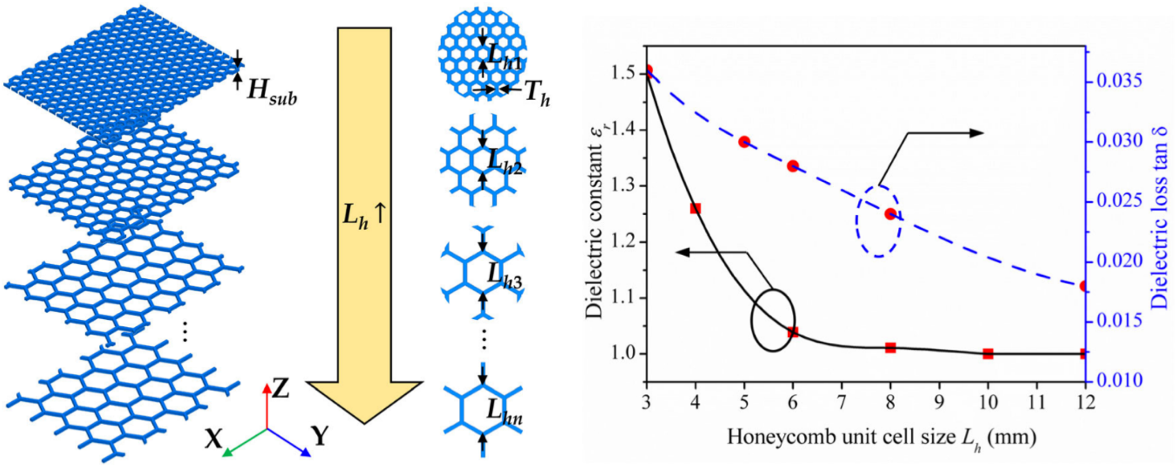

(a) (b)

Fig. 57. (a) Schematic of the PLA honeycomb substrate with differently sized unit cells (L_h= unit cell size, T_h= unit cell thickness, H_{sub}= substrate height); (b) electrical properties of honeycomb substrate with respect to the length of the unit cell L_h [7].

Therefore, taking inspiration by this elaborated structure, in the miniaturized coplanar-fed patch antenna here presented, 4-mm-side squares have been removed from inside the 2 mm-thick substrate, at a 500-µm-distance from the top and the bottom of the substrate surfaces (Fig. 58). Moreover, etchings have been realized in correspondence of the gaps between the feeding waveguide and the coplanar ground to reduce the propagation losses, as done for the previous antenna configurations.

The antenna design parameters are listed in TABLE XI.

In TABLE XII is reported the performance of the antenna at the resonance frequency (935 MHz) and at the operating frequency (868 MHz).

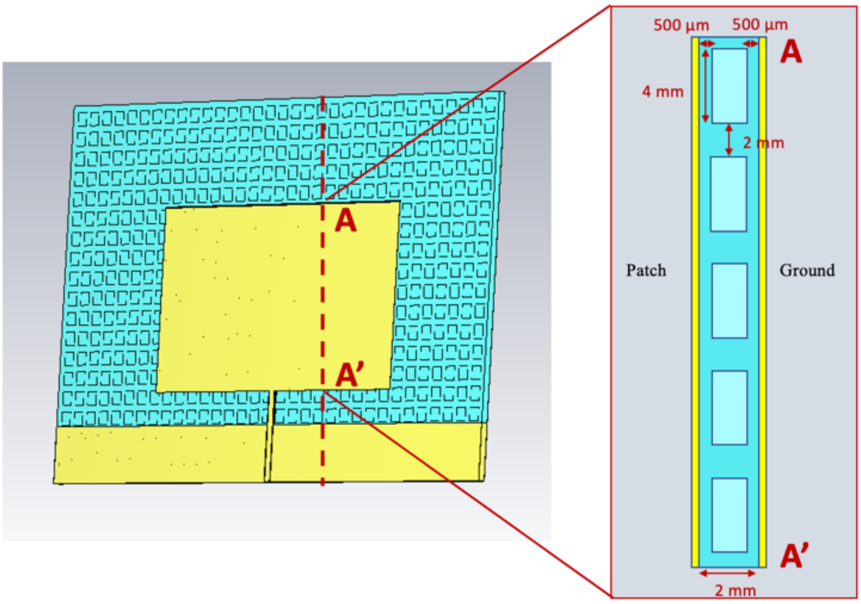

Fig. 58. Layout of the designed coplanar patch antenna of dimensions 55 x 110 mm^2, with a callout on the weft of the trasversal section of the substrate.

TABLE XI. MINIATURIZED COPLANAR FED PATCH ANTENNA WITH SQUARED ETCHINGS IN THE SUBSTRATE GEOMETRIC DIMENSIONS

Antenna Design Parameters	
Description	***Value***
Substrate Height	2 mm
Copper thickness	31.8 µm
Patch length	55 mm
Patch width	110 mm
GCPW width	2.4 mm
Gap between the transmission line and the coplanar ground	0.2 mm
Depth of the substrate etchings in the coplanar gaps.	0.5 mm
Side of the squared holes within the substrate	4 mm
Distance between adjacent squared holes	2 mm

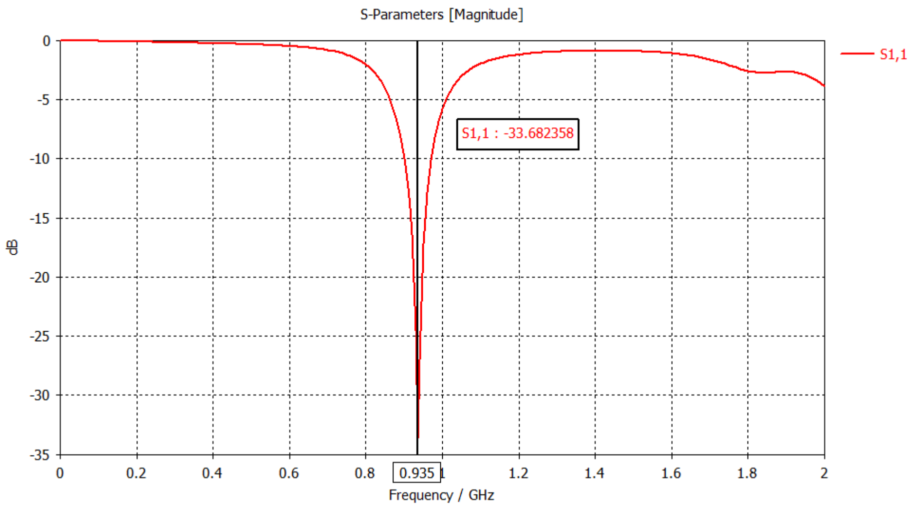

Fig. 59. $|S_{11}|$ parameter of the miniaturized coplanar-fed patch antenna with squared holes etched inside the substrate.

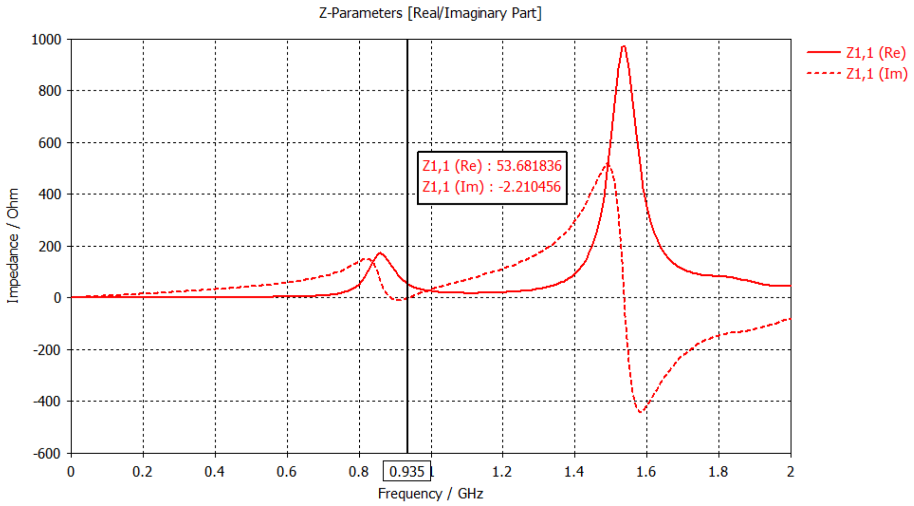

Fig. 60. Input impedance Z_{11} of the miniaturized coplanar fed patch antenna with squared holes etched inside the substrate.

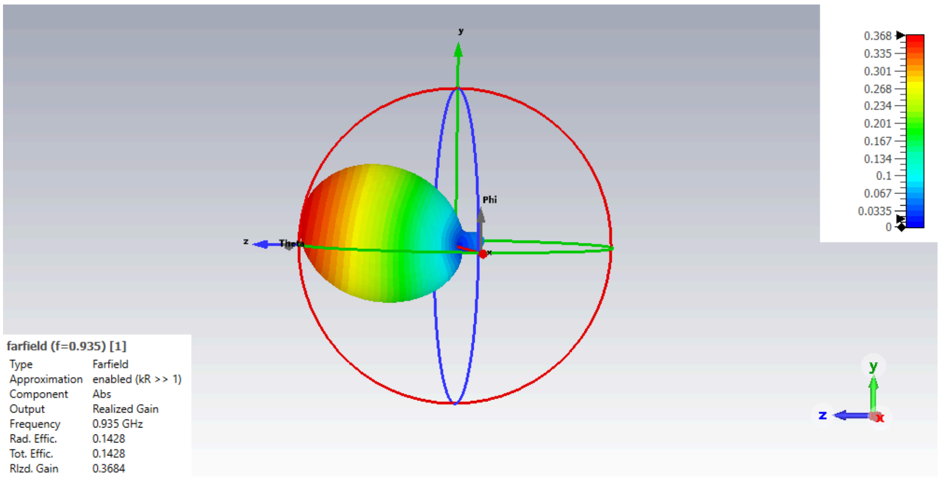

farfield (f=0.935) [1]

Type	Farfield
Approximation	enabled (kR >> 1)
Component	Abs
Output	Realized Gain
Frequency	0.935 GHz
Rad. Effic.	0.1428
Tot. Effic.	0.1428
Rlzd. Gain	0.3684

Fig. 61. Overall performance of the miniaturized coplanar fed patch antenna with squared holes etched inside the substrate at 935 MHz.

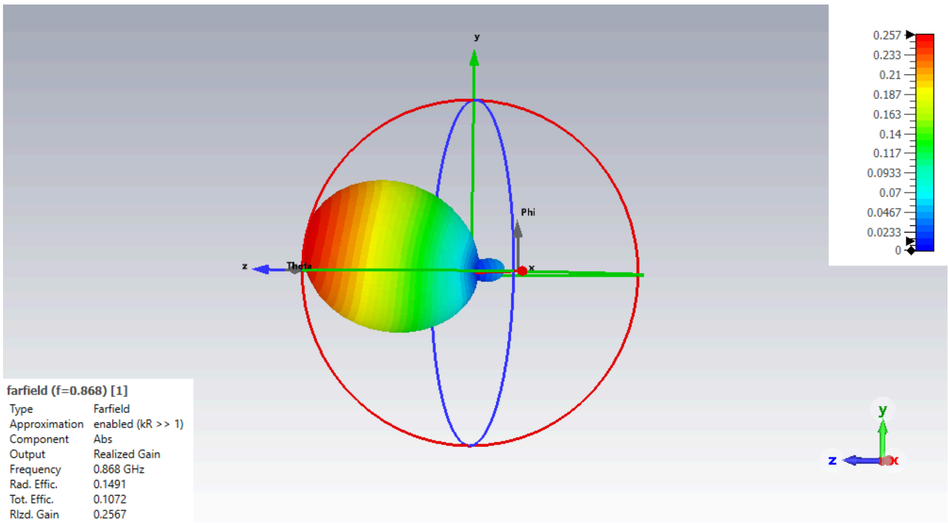

farfield (f=0.868) [1]

Type	Farfield
Approximation	enabled (kR >> 1)
Component	Abs
Output	Realized Gain
Frequency	0.868 GHz
Rad. Effic.	0.1491
Tot. Effic.	0.1072
Rlzd. Gain	0.2567

Fig. 62. Overall performance of the miniaturized coplanar fed patch antenna with squared holes etched inside the substrate at 868 MHz.

TABLE XII. MINIATURIZED COPLANAR FED PATCH ANTENNA WITH SQUARED ETCHINGS IN THE SUBSTRATE PERFORMANCE

Miniaturized Coplanar Fed Patch Antenna Performance at 935 MHz	
Description	***Value***
Realized Gain	–3.14 dBi
Radiation Efficiency	14.3%
Total Efficiency	14.3%

Miniaturized Coplanar Fed Patch Antenna Performance at 868 MHz	
Description	***Value***
Realized Gain	–5.90 dBi
Radiation Efficiency	14.9%
Total Efficiency	10.7%

It must be pointed out that in this case the far-field results of the miniaturized coplanar-fed patch antenna with squared holes etched inside the substrate reported in TABLE XII are given at the resonance frequency of 935 MHz, but the far-field results at 868 MHz don’t differ significatively from those ones.

The values in TABLE XII show that the customization of the substrate as described, leads to a great improvement in terms of the antenna radiation efficiency going from the 8.3% of the antenna layout presented in Section 5.1.4, to 12%.

5.1.6. MINIATURIZED COPLANAR-FED PATCH ANTENNA WITH EMPTIED SUBSTRATE

If performing holes and etchings in the substrate allows to improve the performance, it is expected that an emptied substrate, showing a dielectric constant very close to that of the air and a very low dielectric loss tangent, should boost the radiation efficiency.
Based on this assumption, the extreme case of a patch antenna realized on a completely emptied substrate has been designed and simulated. In order to give more robustness to the structure, pillars made of substrate material with 10 mm of diameter and same substrate height, have been distributed symmetrically within the structure as shown in Fig. 63.

In TABLE XIV is reported the performance of the antenna at the resonance frequency (920 MHz) and at the operating frequency (868 MHz).

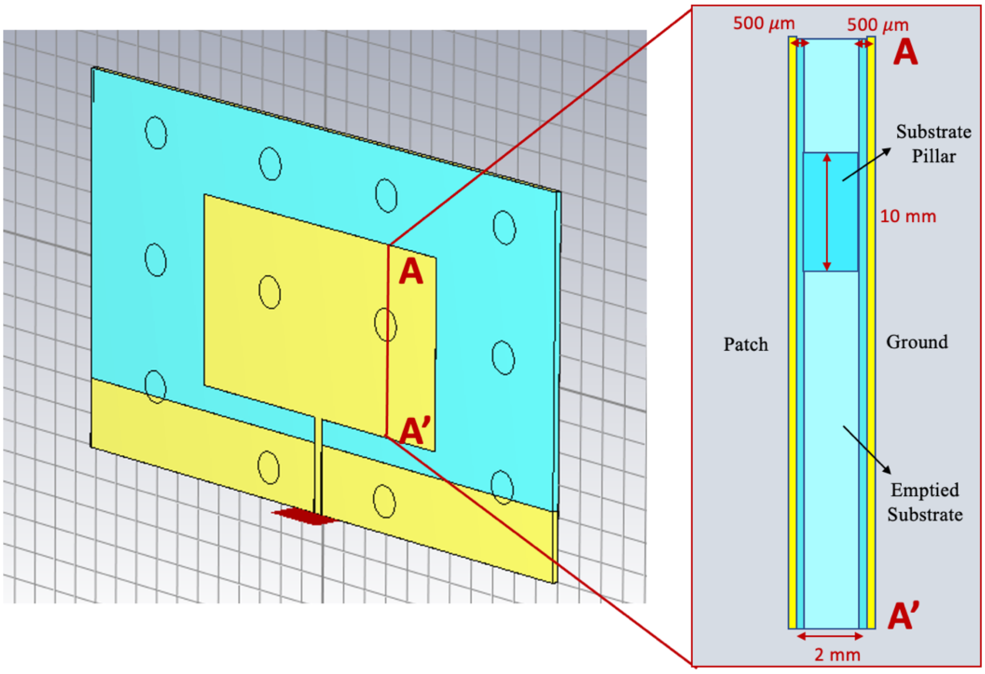

Fig. 63. Layout of the designed coplanar patch antenna of dimensions 55 x 110 mm^2, with a callout on the weft of the transversal section of the substrate.

TABLE XIII. MINIATURIZED COPLANAR-FED PATCH ANTENNA WITH EMPTIED SUBSTRATE GEOMETRICAL DIMENSIONS

Antenna Design Parameters	
Description	***Value***
Substrate Height	2 mm
Copper thickness	31.8 μm
Patch length	55 mm
Patch width	110 mm
GCPW width	2.4 mm
Gap between the transmission line and the coplanar ground	0.2 mm
Depth of the substrate etchings in the coplanar gaps.	0.5 mm
Diameter of the pillars within the substrate	10 mm

Antenna Design Parameters	
Description	***Value***
Horizontal Distance between pillars	45 mm
Horizontal Distance between pillars	30 mm

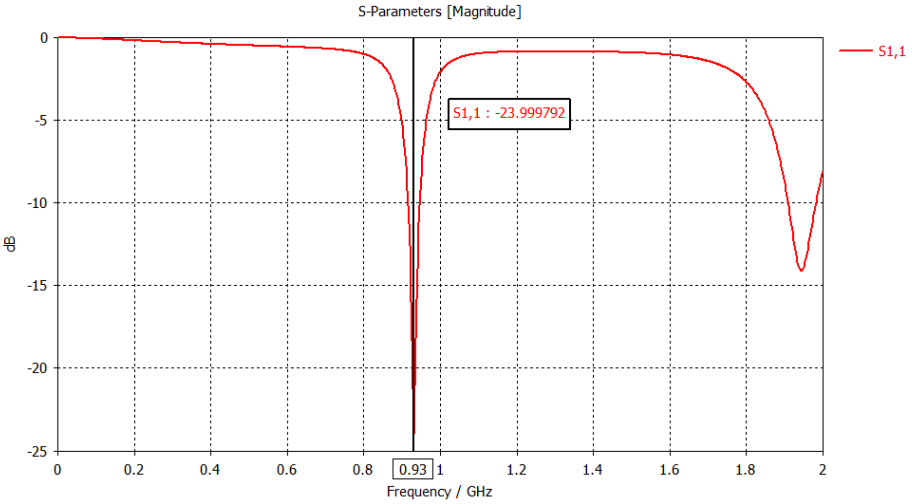

Fig. 64. $|S_{11}|$ parameters of the miniaturized coplanar fed patch antenna emptied substrate.

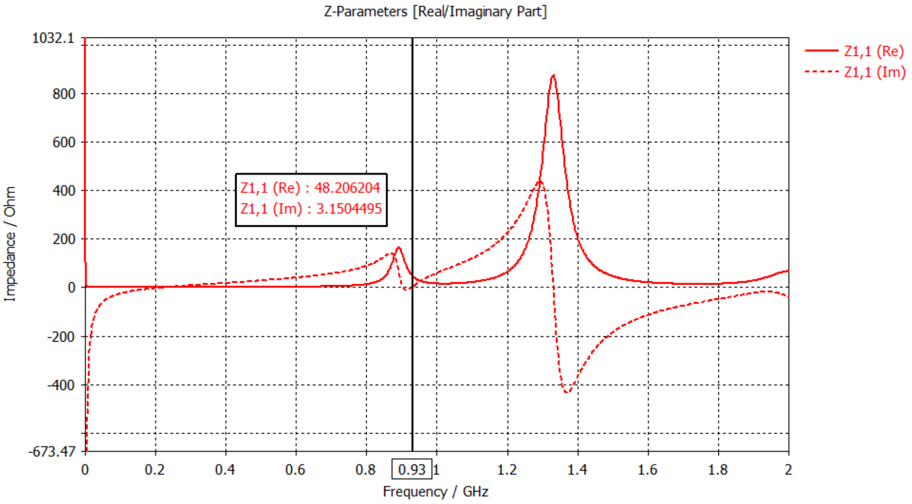

Fig. 65. Z_{11} parameter of the miniaturized coplanar fed patch antenna emptied substrate.

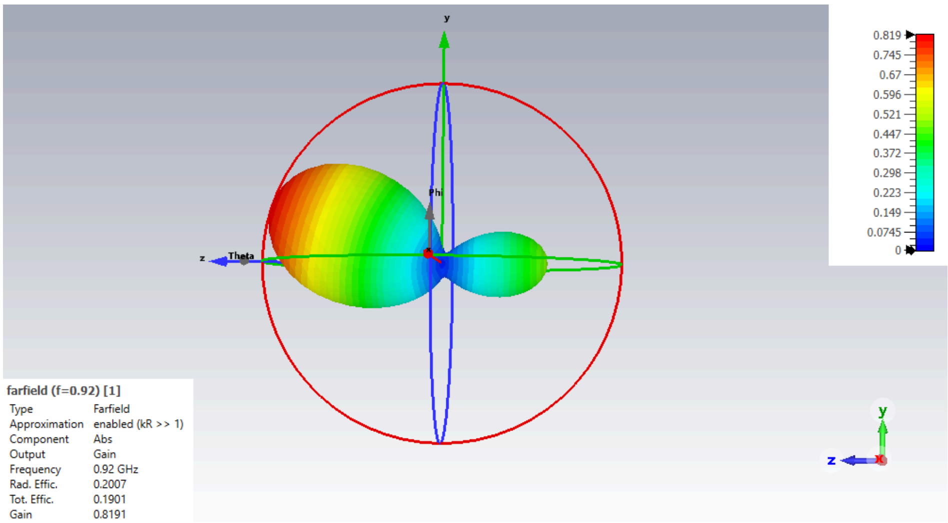

farfield (f=0.92) [1]

Type	Farfield
Approximation	enabled (kR >> 1)
Component	Abs
Output	Gain
Frequency	0.92 GHz
Rad. Effic.	0.2007
Tot. Effic.	0.1901
Gain	0.8191

Fig. 66. Overall performance of the miniaturized coplanar fed patch antenna with emptied substrate at 920 MHz.

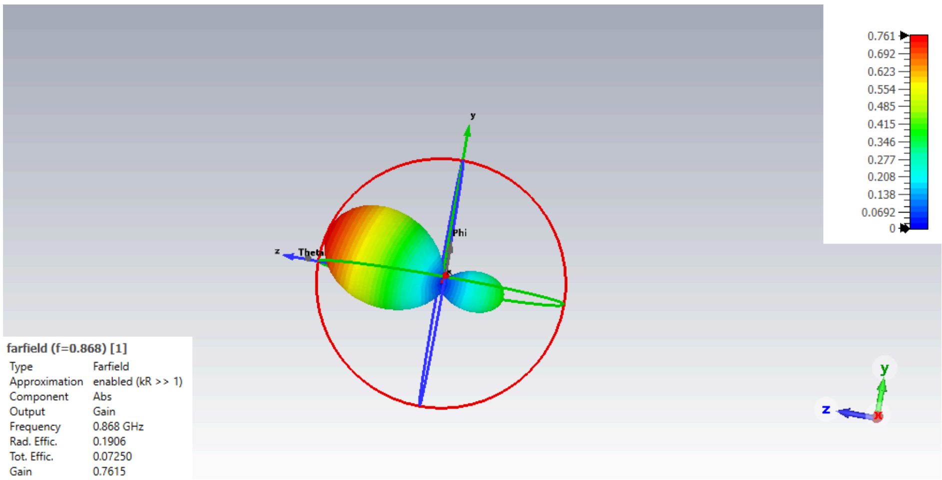

farfield (f=0.868) [1]

Type	Farfield
Approximation	enabled (kR >> 1)
Component	Abs
Output	Gain
Frequency	0.868 GHz
Rad. Effic.	0.1906
Tot. Effic.	0.07250
Gain	0.7615

Fig. 67. Overall performance of the miniaturized coplanar fed patch antenna with emptied substrate at 868 MHz.

TABLE XIV. MINIATURIZED COPLANAR-FED PATCH ANTENNA WITH EMPTIED SUBSTRATE ANTENNA PERFORMANCE

Miniaturized Coplanar Fed Patch Antenna with Emptied Substrate Performance at 920 MHz	
Description	***Value***
Realized Gain	–0.87 dBi
Radiation Efficiency	20%
Total Efficiency	19%

Miniaturized Coplanar Fed Patch Antenna Performance with Emptied Substrate at 868 MHz	
Description	***Value***
Realized Gain	–1.18 dBi
Radiation Efficiency	19%
Total Efficiency	7.25%

The far-field results reported in TABLE XIV show that emptying the substrate leads to a great improvement to the radiation efficiency both at the resonance frequency of 935 MHz and at 868 MHz, achieving about 20% of radiation efficiency.

Moreover, as can be noticed from the radiation diagram in Fig. 66 and Fig. 67, the main lobe direction is slightly tilted of 15 degrees with respect to the normal to the patch plane and there is some back radiation due to the fact that the patch dimensions are comparable to that of the ground metallization below the structure.

5.1.7. COPLANAR-FED PATCH ANTENNA OPERATING AT 2.45 GHZ

An interesting observation coming from the last antenna topologies presented is that the radiation efficiency is higher at higher frequencies.

For this reason, it has been considered to increase the operating frequency from 868 MHz to 2.45 GHz. This also allows to significantly reduce the antenna dimensions without using the shorting plate technique. The current antenna dimensions are listed in TABLE XV. The width of the patch has been enlarged with respect to its length in order to enhance the radiation efficiency, going from a value of 57% of the squared patch, to 64%.

Moreover, the substrate etchings of the present antenna topology have been modified and designed as a tradeoff between the completely emptied substrate and the substrate etchings performed around the antenna perimeter. In fact, the substrate has been emptied just in a rectangular volume slightly larger than the patch and a 0.3-mm-thick layer of substrate have been kept as supporting layers on top and at the bottom surfaces of the substrate, as shown in Fig. 69. The same kind of dielectric material removal has been performed below the coplanar feeding line, while the etchings in the gaps between the line and the coplanar ground have been prolonged at the whole substrate height but kept with rectangular shape and gap width (G_p), see Fig. 70.

The GCPW with this kind of substrate etchings in the gaps between the line and the coplanar ground and below the line itself, has been simulated in CST and the resulting $|S_{12}|$ curve has been compared to the $|S_{12}|$ curves obtained from the simulation of two other GCPWs designed on a 2mm-thick substrate, with rectangular etchings as those shown in Fig. 30, and without etchings, respectively. The comparison is reported in Fig. 71 and demonstrates that this new kind of etchings, illustrated in Fig. 70, has the best performance compared to the others, losing about 1.8 dB at 6 GHz.

In addition, in order to maintain the structure robustness where the substrate has been emptied, small squared pillars of 4 mm side have been introduced, as illustrated in Fig. 69 where the squared dashed lines determine their position inside the substrate emptied space.

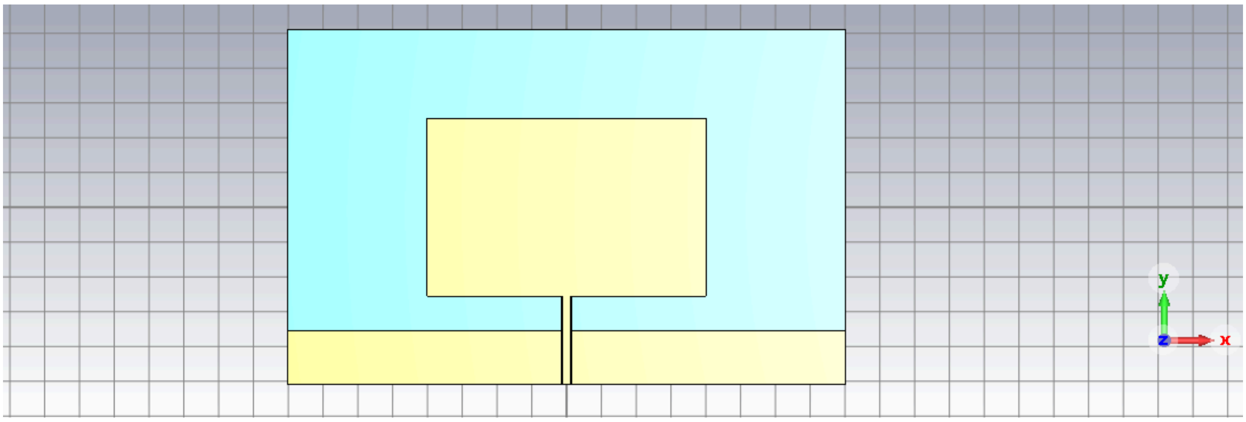

Fig. 68. Coplanar-fed patch antenna of dimensions 51 x 80 mm^2 operating at 2.45 GHz: front view.

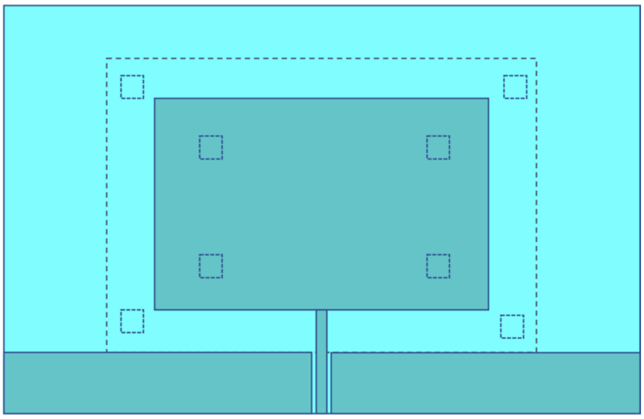

Fig. 69. Substrate layout of the coplanar-fed patch antenna operating at 2.45 GHz: the dark blue areas are the ones where the patch metallization is placed on top of the substrate and the dashed lines delimit the perimeter of the emptied area inside the substrate and the pillars' position.

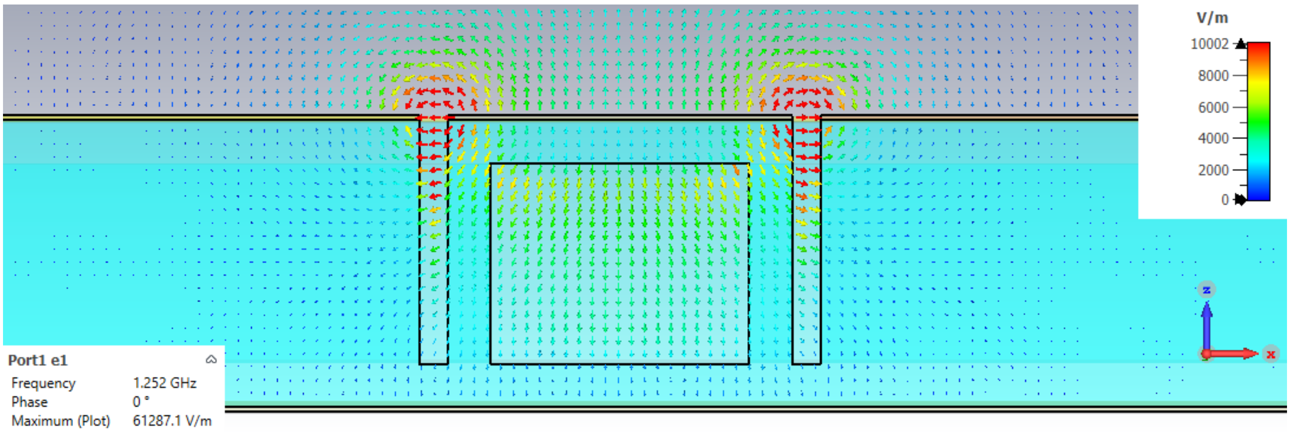

Fig. 70. Substrate etching in between the feeding line and the coplanar ground and rectangular excavation below the line.

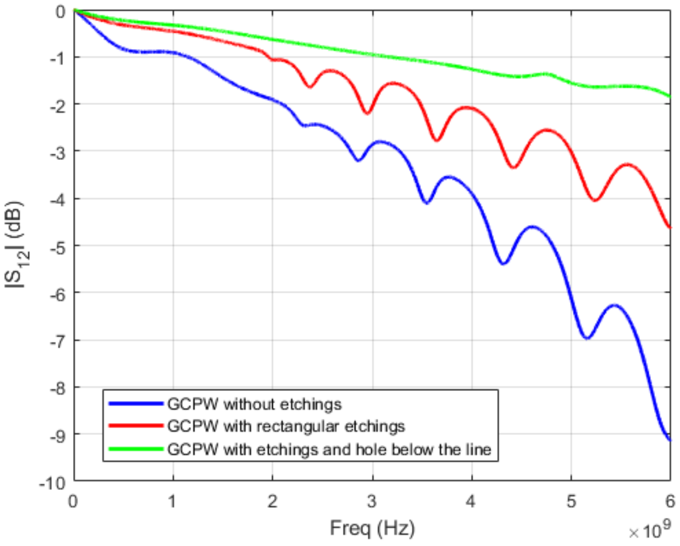

Fig. 71. Comparison of the $|S_{12}|$ curves of GCPW structures on a 2 mm-thick substrate with etchings in the gaps between the line and the coplanar ground, see Fig. 70, with rectangular etchings, see Fig. 30, and GCPW without etchings.

TABLE XV. COPLANAR-FED PATCH ANTENNA OPERATING AT 2.45 GHZ GEOMETRIC DIMENSIONS

Antenna Design Parameters	
Description	***Value***
Substrate Height	2 mm
Copper thickness	31.8 µm
Patch length	51 mm
Patch width	80 mm
GCPW width	2.4 mm
Gap between the transmission line and the coplanar ground	0.2 mm
Gap between the bottom patch edge and the coplanar ground	10 mm
Depth of the substrate etchings in the coplanar gaps	1.7 mm
Depth of the substrate etching below the patch and below the feeding line	1.4 mm
Thickness of substrate layer kept on top and at the bottom of the substrate in correspondence of the etchings	0.3 mm
Side of the squared pillars	4 mm

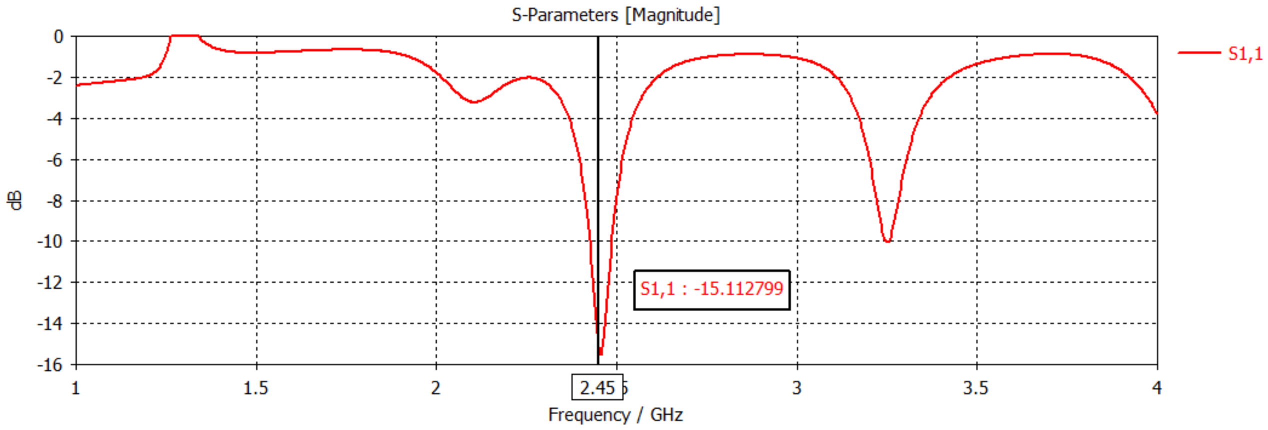

Fig. 72. |S_{11}| parameter of the coplanar-fed patch antenna operating at 2.45 GHz.

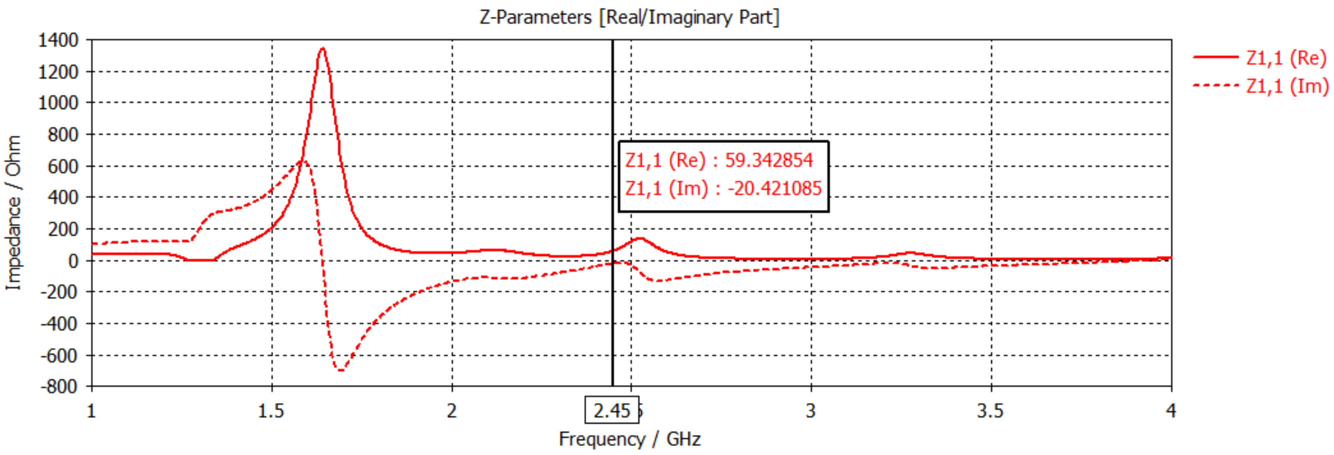

Fig. 73. Z_{11} parameter of the coplanar-fed patch antenna operating at 2.45 GHz.

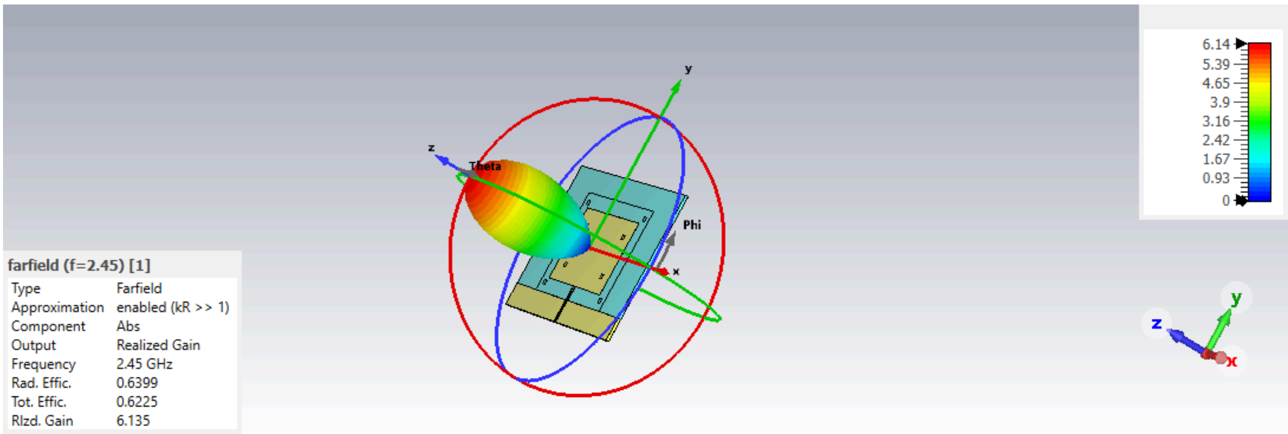

farfield (f=2.45) [1]

Type	Farfield
Approximation	enabled (kR >> 1)
Component	Abs
Output	Realized Gain
Frequency	2.45 GHz
Rad. Effic.	0.6399
Tot. Effic.	0.6225
Rlzd. Gain	6.135

Fig. 74. Far-field simulation results of the coplanar-fed patch antenna operating at 2.45 GHz.

TABLE XVI. COPLANAR-FED PATCH ANTENNA OPERATING AT 2.45 GHZ PERFORMANCE

Radiation Performance of the Coplanar Fed Patch Antenna operating at 2.45 GHz	
Description	***Value***
Realized Gain	7.88 dBi
Radiation Efficiency	64%
Total Efficiency	62.3%

From the far-field simulation results obtained, and reported in TABLE XVI, is clear that increasing the patch operating frequency from 868 MHz to 2.45 GHz and using this emptied-substrate layout led to very good antenna performance, reaching 64% of radiation efficiency, also allowing to overcome the high dielectric losses intrinsic to the Flexible80A substrate.

In this case, being the patch antenna dimensions much smaller than the ground metallization at the bottom of the structure, there is no back radiation.

To conclude this section, TABLE XVII summarizes the radiating performances obtained by the different antennas designed and here presented at their corresponding operating frequency, in order to show the process which has led to the optimization of the design of a patch antenna on a lossy dielectric material such as the Flexible80A, by means of the introduction of innovating etching techniques which are possible thanks to the design freedom provided by 3D-printing technology.
In particular, have been highlighted the best obtained results in terms of radiation performances.

TABLE XVII. SUMMARY OF DESIGNED ANTENNA PERFORMANCES

Antenna topology	**Operating Frequency**	**Realized Gain**	**Radiation Efficiency**	**Total Efficiency**
5.1.1 - MICROSTRIP PATCH ANTENNA	*868 MHz*	*–6.25 dBi*	*6.3%*	*4.8%*
5.1.2 – COPLANAR-FED PATCH ANTENNA ON ETCHED SUBSTRATE	*868 MHz*	*–3.05 dBi*	*13%*	*10%*
5.1.3 – COPLANAR PATCH ANTENNA WITH ETCHED SUBSTRATE	*868 MHz*	*–3.70 dBi*	*11%*	*8.6%*
5.1.4 – MINIATURIZED COPLANAR-FED PATCH ANTENNA WITH ETCHED SUBSTRATE	*868 MHz*	*–5.12 dBi*	*8.3%*	*8.2%*
5.1.5 - MINIATURIZED COPLANAR-FED PATCH ANTENNA WITH SQUARED ETCHINGS IN THE SUBSTRATE	*868 MHz*	*–5.90 dBi*	*14.9%*	*10.7%*
5.1.6 - MINIATURIZED COPLANAR-FED PATCH ANTENNA WITH EMPTIED SUBSTRATE	*868 MHz*	*–1.18 dBi*	*19%*	*7.25%*
5.1.7 – COPLANAR-FED PATCH ANTENNA OPERATING AT 2.45 GHz	***2.45 GHz***	***7.88 dBi***	***64%***	***62.3%***

Being the coplanar-fed patch antenna (Section 5.1.7) the antenna showing the best radiation performances, it has been selected as receiving antenna to be connected to the rectifier in the rectenna design that will be described in Chapter 5.2.

5.2. RECTENNA DESIGN

The aim of this thesis is to realize a low cost, 3D-printable, miniaturized, and wearable planar rectenna on a flexible substrate material, the Flexible 80A.
To begin with, before presenting the rectenna designed in this thesis, here is given an introductive overview about rectenna systems, impedance matching and the on-going dilemma of representing the receiving antenna equivalent circuit.

5.2.1. RECTENNA DEFINITION AND FUNCTIONS

A rectenna (rectifying antenna) consists mainly of two elements: an antenna to collect the power transmitted by an intentional source (WPT) or harvested by the surrounding EM environment, and a rectifier nonlinear circuit which is able to convert the RF power collected by the antenna into dc power which is typically stored in a capacitor or a battery and re-used as a power supply when needed [38]. A schematic of a standard rectenna system for far-field WPT or EH applications is shown in Fig. 75. Both in EH and far-field WPT applications is of extreme importance to have a clear evaluation of the power budget. Being this project meant for far-field WPT applications, the following discussion will focus on that.

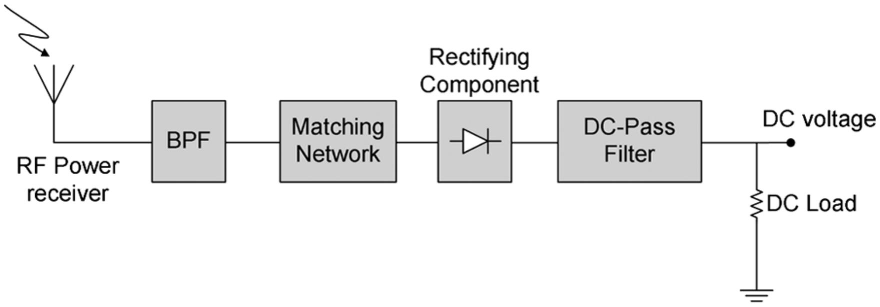

Fig. 75. General block diagram of a rectenna system for WPT or EH applications [38].

In order to realize an efficient far-field radiative WPT, first of all it must be considered the power lost due to the large distance. Moreover, the used frequencies are usually in the license-free bands for Industry, Science, and Medicine (ISM), thus limited in allowed transmit power. This means that the power actually received by a single receiving antenna element is already limited, which further stresses the significance of designing a highly efficient receiving antenna, since the amount of power made available at the rectifier input, must be sufficient to activate it. Therefore, in order to obtain a high Power Conversion Efficiency (PCE) of the rectenna system (i.e., the ratio between the dc output power delivered to the load and the RF power available to the receiving antenna) as high as possible, the efficiency of each single rectenna element must be maximized and the optimum rectifier load must be chosen [39].

As regards the rectifier, it is a nonlinear circuit typically consisting of Schottky diodes, an output bypass capacitor acting as a dc filter suppressing the harmonics produced by the nonlinear diodes performance, and an optimum load resistor. Many different rectifier topologies may be adopted depending on the diodes configuration, which may be single series, single shunt, or voltage multipliers, as illustrated in Fig. 76. The latter consists of multiple diodes arranged in such a way to produce an output voltage *n*- times greater than the one at the rectifier input (where *n* is the number of diode stages in the voltage multiplier). Obviously, the higher the number of diodes introduced in the rectification circuit, the higher will be also the losses related to the diodes junction resistance and the amount of nonlinearities introduced.

In the present work, a voltage doubler made of two SMS7630-079LF Schottky diodes has been used for rectification purposes in order to further improve the output voltage at the load.

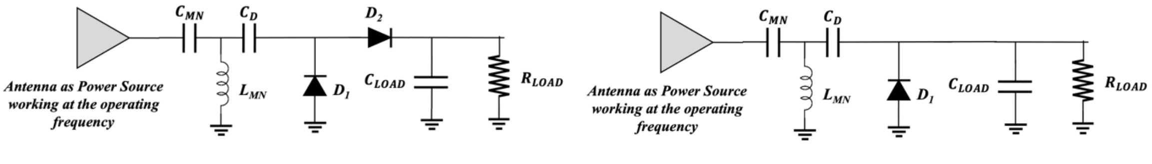

a) Voltage Doubler

b) Shunt Diode

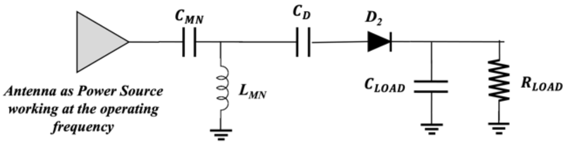

c) Series Diode

Fig. 76. Schematic of three different Rectifier topologies: (a) voltage doubler, (b) shunt diode, and (c) series diode.

In addition to the choice of the rectifier configuration, the impedance matching network is one of the most critical aspects of designing an efficient rectenna system, due to the fact that the rectifier, consisting of diodes, is a nonlinear device whose input impedance varies both with input power and frequency, meaning that an accurate full wave nonlinear analysis is needed in order to predict the rectifier impedance behavior over a wide range of input powers [40]. To maximize the power transfer from the antenna to the diodes, the antenna input impedance, evaluated by means of linear EM analysis at a specific operating frequency and input power level, must be matched to the nonlinear behavior of the rectifier input impedance by means of an ad-hoc designed matching network. Unfortunately, at high frequencies, planar technology matching networks need to be realized by means of distributed elements such as pieces of microstrip lines and open and/or short stubs which introduce losses and increase the overall rectenna size, in addition to narrowing the overall operating frequency band.

This is why, in recent years, many authors have investigated the possibility of removing the matching network with the aim of reducing the losses, the size and the costs for the realization of rectennas, designing the receiving antenna input impedance in order to be conjugate matched to the rectifier input impedance ($Z_{Antenna} = Z^{*}_{Rectifier}$) such as in [39], [40], [41].

This is also one of the goals addresses by this work. In fact, it will be demonstrated that, being the Flexible80A a lossy substrate, the introduction of a matching network made of distributed components, even if in GCPW technology, affects very much the overall rectenna efficiency. Thus, the performance of a rectenna design with external matching network in between the antenna and the rectifier, and a rectenna where the receiving antenna has been specifically designed in order to have an input Impedance conjugate matched to that of the rectifier, have been compared.

Fig. 77 shows a measurement set up of a 50 Ω rectenna with external matching network, and the one of a rectenna where the matching network has been removed because of the receiving antenna impedance is directly conjugate matched to the rectifier input impedance.

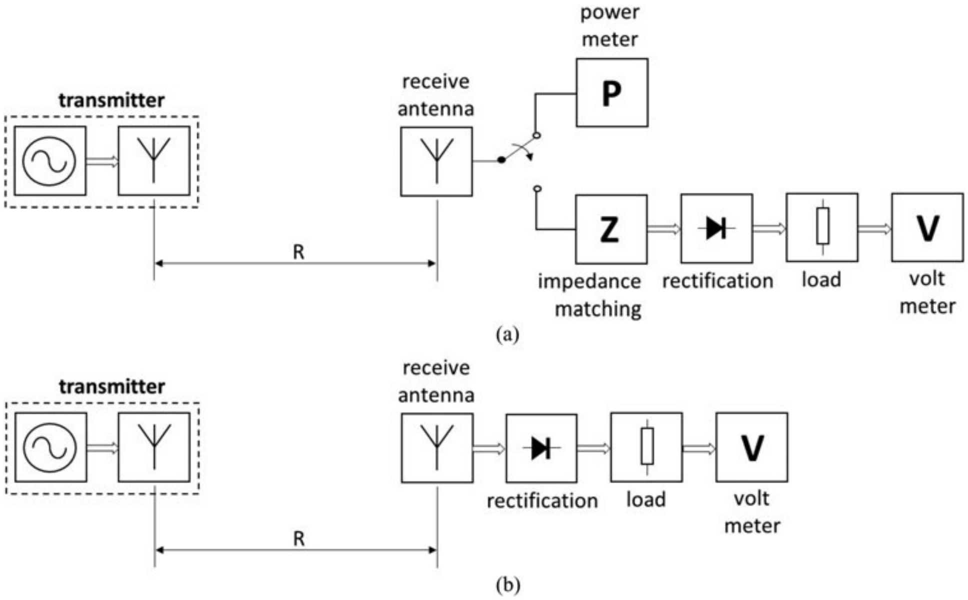

Fig. 77. Rectenna measurement setups. (a) Setup for 50 V rectenna measurement; (b) setup for complex conjugate impedance matched rectenna measurement [39].

The overall rectenna system, being an RF nonlinear device due to the diodes operations, must be simulated by means of circuital/EM simulations, where the antenna part, in which the EM effects cannot be neglected, is simulated with an EM simulator, from which is then extracted the corresponding matrix description (scattering, and impedance/admittance matrices) and imported into the circuital simulator.

The overall system is thus simulated by means of Harmonic Balance (HB) method analysis which is a mixed-domain method which directly addresses the RF circuit operating in steady state regime without analyzing its transient, and where the linear components are described in the frequency domain (i.e., taking into account their dispersive effects), whereas the nonlinear components are described in time domain (and then transformed in frequency domain (Fast Fourier Transform)). Since the circuital simulator used in the present work is Keysight ADS, are here described the operating principles of its HB simulator.

As mentioned, the HB Simulator has the main objective of computing the steady-state solution of a nonlinear circuit which is represented as a system of N differential equations, where N is the size of the circuit (number of nodes and branch currents). The source and the solution waveforms (all node voltages and branch currents) are approximated by truncated Fourier series [42]. In particular, a rectenna with a single receiving antenna element, will be represented as a circuit with a single input power source requiring a single tone HB analysis.

The truncated Fourier series representation of the solution transforms the system of N nonlinear differential equations into a system of $N \times M$ nonlinear algebraic equations in the frequency domain, where M is the total number of frequencies including the fundamentals (whenever there is more than one), their harmonics, and the mixing terms (in the case of multiple input tone excitations).

The system of nonlinear equations is derived from applying the Kirchhoff’s currents law (KCL) in the frequency domain to each node connecting the linear subnetwork (the circuital part consisting of linear components only) to the nonlinear one (the circuital part consisting of nonlinear components only), meaning that the sum of the currents entering the node must be equal to the sum of the currents exiting it.

This system of algebraic equation is solved via Newton's method, the nonlinear solver of the HB simulator. This is an iterative method which starts from an initial guess to arrive at the solution and thus achieving the convergence when the KCL residual (the amount by which the KCL is violated at each iteration) is driven to a small value.

5.2.2. RECEIVING ANTENNA EQUIVALENT CIRCUIT: AN OVERVIEW

As mentioned above, in order to simulate the overall rectenna system, the EM-simulated antenna must be imported in the circuital simulator in order to take into account, even in the circuital nonlinear analysis, its EM behavior, namely its scattering matrix, its impedance or admittance matrix and thus, the far-field results such as radiation efficiency, gain and total efficiency (evaluated as mentioned in the previous Chapter, in section 5.1.1).

Actually, the representation of the receiving antenna equivalent circuit has been an hot discussion topic for many years and has been addressed by many authors such as R.E. Collin in [43], A.W. Love in [44], M.A.C. Niamien et al. in [45], and Li et al. in [46]. To follow, it will be given a brief reconstruction of the mentioned authors positions about this topic and the position adopted in this thesis.

To begin with, C.A. Balanis in "Antenna theory analysis and design" [47] defines the input impedance of an antenna at its terminals as:

$$\boldsymbol{Z_A = R_A + jX_A} \tag{49}$$

where R_A is the antenna resistance at its terminals and X_A is the antenna reactance.
The resistive part of the antenna consists of two components, namely the radiation resistance R_T and the loss resistance R_J , thus

$$\boldsymbol{R_A = R_T + R_J} \tag{50}$$

If the antenna is used in the receiving mode, it can be represented as shown in Fig. 78 (a), where the incident wave impinges upon the antenna, inducing a voltage V_i. The antenna can be represented with its Thevenin or Norton equivalent circuits as illustrated in Fig. 78 (a), where Z_L is the antenna load impedance:

$$\boldsymbol{Z_L = R_L + jX_L} \tag{51}$$

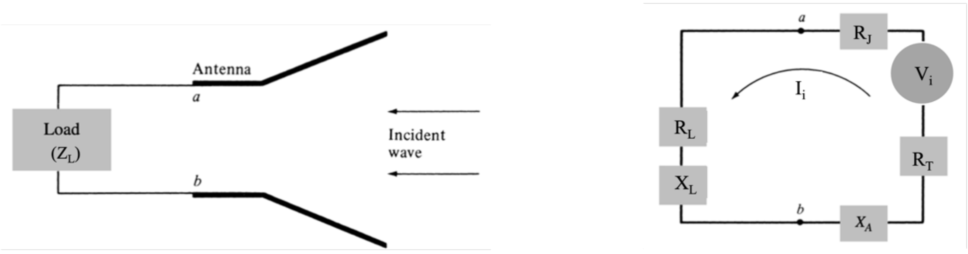

(a) (b)

Fig. 78. (a) Schematic representation and (b) Thevenin equivalent circuit of an antenna in receiving mode [47].

In receiving mode, under conjugate matching conditions ($R_T + R_J = R_L$ and $X_A = -X_L$), the amount of power delivered to the load R_L (P_L), the power available, delivered to the radiation resistance R_T, which is the scattered or reradiated power P_T, and the amount of power P_J dissipated in R_J as heat, can be calculated respectively as:

$$\boldsymbol{P_L = \frac{|V_i|^2}{8}\left[\frac{R_L}{4(R_T + R_J)^2}\right] = \frac{|V_i|^2}{8}\left[\frac{1}{R_T + R_J}\right] = \frac{|V_i|^2}{8R_L}} \tag{52}$$

$$\boldsymbol{P_T = \frac{|V_i|^2}{2}\left[\frac{R_T}{4(R_T + R_J)^2}\right] = \frac{|V_i|^2}{8}\left[\frac{R_T}{(R_T + R_J)^2}\right]} \tag{53}$$

$$\boldsymbol{P_J = \frac{|V_i|^2}{8}\left[\frac{R_J}{(R_T + R_J)^2}\right]} \tag{54}$$

while the captured power during conjugate matching is given by:

$$\boldsymbol{P_C = \frac{1}{2}\, V_i I_i^* = \frac{1}{2} V_i \left[\frac{V_i^*}{2(R_T + R_J)}\right] = \frac{|V_i|^2}{4}\left[\frac{1}{R_T + R_J}\right]} \tag{55}$$

Under conjugate matching conditions, it is clear that half of the total power captured by the antenna is delivered to the load R_T, whereas the other half is both scattered or reradiated through R_T and dissipated as heat through R_J. On the other hand, when the antenna is lossless ($R_J = 0$), half of the captured power is delivered to the load and the other half is scattered.

The definition of the antenna radiation efficiency based on these considerations takes into account the reflection, conduction, and dielectric losses. The conduction and dielectric losses are difficult to compute and in most cases they are measured. Even with measurements, they are difficult to separate, and they are usually considered together in R_J to form the conduction-dielectric efficiency, defined as the ratio between the power delivered to the radiation resistance R_T and the power delivered to R_T and R_J. Thus, the radiation efficiency can be written as:

$$\boldsymbol{\eta_{rad} = \frac{R_T}{R_T + R_J}} \tag{56}$$

R.E. Collin in [43] questions the appropriateness of using Thevenin or Norton equivalent Circuit models in order to evaluate either the power absorbed or scattered by a receiving antenna system. In particular, he states that it is not correct to equate the power dissipation calculated within the Thevenin and Norton equivalent circuits to the power reradiated or scattered from the receiving antenna as many articles and textbooks do. In fact, Collins claims that “the internal power dissipation in the Thevenin and Norton equivalent antenna circuits does not have a physical meaning. There is no known power-conservation theorem associated with it.” However, they can be used to find the reradiated EM field that is a part of the total field scattered by a receiving antenna.

Thus, starting from the representation of a transmitting-receiving antenna system shown in Fig. 79, where Z_{11} is the input impedance of the receiving antenna, Z_{12} is the interaction term between the transmitting-receiving antennas, Z_{22} is the impedance of the transmitting antenna, and Z_g and V_g are respectively the internal generator impedance and voltage, he affirms that in this system the power conservation principle can be established by the following expression:

$$P_{in} = P_L + P_{LT} + P_{LR} + P_R \tag{57}$$

where P_{in} is the input power at the transmitting antenna terminal, P_L is the power across the receiving antenna load impedance, P_{LT} is the power loss intrinsic to the transmitting antenna and P_R is the power actually radiated. This latter term summarizes three different power terms, namely the power radiated by the transmitting antenna, the power scattered by the receiving antenna and a power interaction term. The power dissipated in the impedance elements Z_{11}, Z_{12}, Z_{22} and Z_L shown in Fig. 79 corresponds to the power terms in the right hand side of (49) and can be solved for and equated to P_{in}. The problem related to this representation is relating those power terms to the power dissipated in the impedance elements.

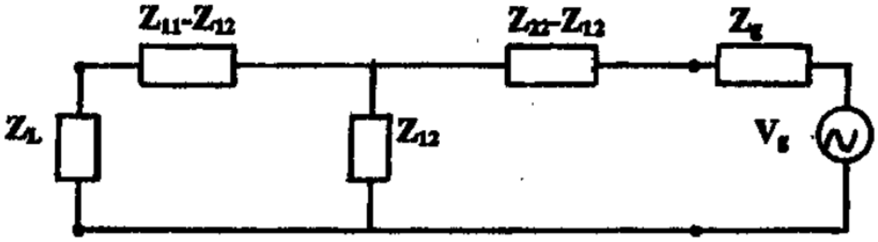

Fig. 79. Equivalent circuit for a transmitting-receiving antenna circuit [43].

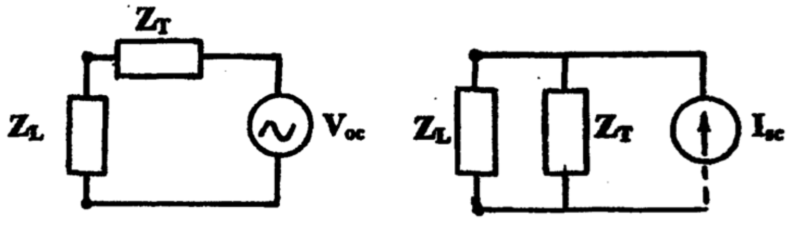

(a) (b)

Fig. 80. (a) Thevenin equivalent circuit and (b) Norton equivalent circuit for a receiving antenna [43].

If the receiving antenna is described by means of the Thevenin and Norton equivalent circuits, as shown in Fig. 80 (a) and (b) respectively, the power delivered to the receiving antenna can be calculated in both cases as:

$$P_L = \frac{1}{2}\left|\frac{V_{OC}}{Z_L + Z_T}\right|^2 Re\{Z_L\} \tag{58}$$

whereas, if we calculate the internal power dissipated in the network in both cases, using the Thevenin equivalent circuit it will be obtained:

$$P_D = \frac{1}{2}\left|\frac{V_{OC}}{Z_L + Z_T}\right|^2 Re\{Z_T\} \tag{59}$$

And using the Norton equivalent circuit:

$$P_D = \frac{1}{2}\left|\frac{V_{OC}}{Z_L + Z_T}\right|^2 \left|\frac{Z_L}{Z_T}\right|^2 Re\{Z_T\} \tag{60}$$

The expressions (51) and (52) are different, excepted when $|Z_L|=|Z_T|$, thus this shows that the Thevenin and Norton equivalent circuits cannot be relied upon for calculating the internal power dissipated inside the network.

However, since the mutual impedance term Z_{12} is usually very small, the power in the receiving antenna load impedance will be very small compared to the power delivered by the source generator to Z_g and Z_{22} (the transmitting antenna input impedance). Thus, the total internal power dissipated in the network will be much greater than that given in expressions (51) and (52), which have the same order of magnitude of the power delivered to the receiving antenna load.
It can also be noted that in Thevenin and Norton equivalent circuits, when the antenna is open-circuited, the scattered power is null, because there wouldn't be any internal dissipated power, but this is not physically true. In fact, when an antenna is open-circuited although no current exists at its terminals, induced currents exist on the antenna structure itself due to EM coupling. Thus, these surface currents will reradiate in all directions giving a non-zero scattered power in open-circuit mode, as pointed out by M.A.C. Niamien et al. in [45]. In this paper, in fact, they propose a hybrid model equivalent circuit for a receiving antenna which takes into account the power scattered by the antenna when operating either in open or short-circuit mode. It consists of two blocks, as shown in Fig. 81 (a), the left-hand block is identical to the Thevenin circuit, representing the coupling between the antenna and the incident wave E_{inc} (h_e in the figure corresponds to the antenna's effective height), the right-hand block represents the radiation pattern term ($-F_r \cdot I_L$) where F_r is the current-normalized radiated field in the far-field region and I_L is the load current, opposite to the input current I_1, whereas $S_{OC} \cdot E_{inc}$ is the open circuit scattering pattern term of the antenna, where S_{OC} is the open-circuit scattering coefficient used to physically represent how much the open-circuited illuminated antenna, would couple to the incident wave (E_{inc}).
Since a general receiving antenna can behave either as a series or a parallel RLC circuit, both short and open scattered fields are inserted, so that the scattered field E_S is given as:

$$E_S = \frac{V_L}{V_{OC}} E_S^{OC} + \frac{I_L}{I_{SC}} E_S^{SC} \tag{61}$$

and the scattered power is calculated integrating the scattered field E_S in all directions.
Then, the power-budget circuit model can be considered for a general receiving antenna, as shown in Fig. 81 (b), introducing a short-circuit scattering resistance R_S^{SC} and an open circuit scattering conductance G_S^{OC}, which are related to the power scattered by the antenna in short-circuit and in open-circuit, and an open-short scattering correlation coefficient ρ^{OC-SC} which tells whether short and open current modes are correlated.

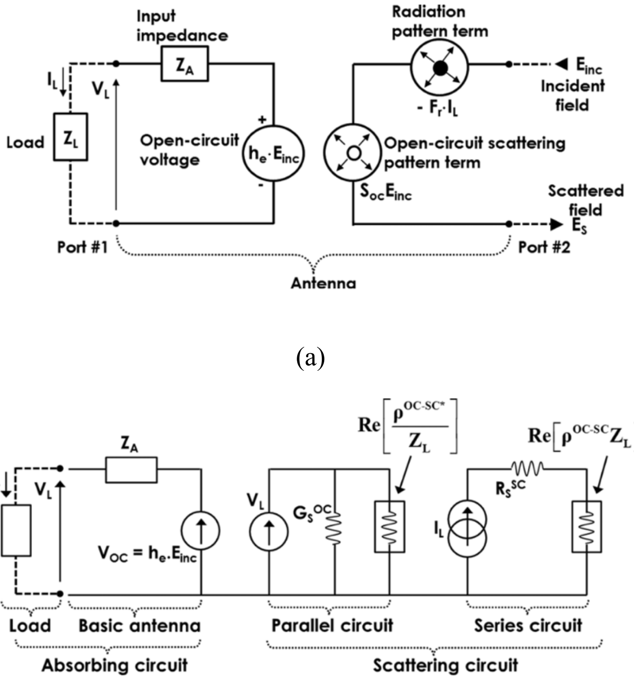

(a)

(b)

Fig. 81. (a) Hybrid model equivalent circuit and (b) power-budget circuit model for a generic receiving antenna [45].

Moreover, the fact that the internal power dissipation obtained by expressions (51) and (52), thus calculated for the Thevenin and Norton equivalent circuits respectively, shouldn't be equated to the power scattered by the receiving antenna is confirmed even by S. Silver in [48].
In fact, he explains that when an incident wave field impinges on the receiving antenna, two interaction effects take place: part of this energy is taken from the incident wave and dissipated inside the antenna as heat, this effect is called absorption, and another part of this energy is reradiated into all directions about the antenna: this is the scattering effect. Whether the antenna is of the same order of magnitude of the wavelength, larger or smaller, the interaction between the incident and reflected waves is the same: the scattered wave is out of phase with the incident wave and thus there is destructive interference between the two fields, resulting in the removal of part of the energy from the incident wave.
The main problem arising here is that the energy which is subtracted from the incident field includes both the absorbed and scattered contributions, and they are different to separate. In fact, even if the definition and measurement of the absorbed power is unambiguous, however, the scattered power is not directly measurable, and its theoretical evaluation is subject to ambiguities. In fact, even if EM fields are additive, their energies are not, and the resultant energy is modified by the interaction between the fields.

Now, if we replace the antenna by an equivalent generator, assuming that the generator has an internal impedance equal to the input antenna impedance Z_A when it is used as a transmitter, and if we connect this generator to a load impedance Z_L, some power will be dissipated both in the load impedance Z_L and in the internal impedance of the generator.

The power dissipated in Z_L is interpreted as the power absorbed from the incident wave by the antenna and delivered to the load, whereas the power dissipated in Z_A is frequently interpreted as the scattered power, i.e., the sum of the power dissipated by the antenna ohmic resistance and the power reradiated. But if the ohmic losses are neglected, the power dissipated in Z_A would coincide with the scattered power. Unfortunately, this interpretation is valid only for dipole antenna and small loop antennas because Silver demonstrates that the power dissipated in the internal impedance of the equivalent generator has no direct relation to the energy reradiated by the antenna and in general cannot be used to evaluate the scattered wave.

Therefore, as clarified also by the previous mentioned authors, the Thevenin or Norton equivalent circuit representations can be used in general only for the treatment of absorption and it is not possible to separate the dissipated power contribution from the scattered one.

Other famous authors deal with the same topic. One of them is A.W. Love, who proposes in [44] an alternative equivalent circuit with both equivalent voltage and current sources for a receiving antenna for which a physical aperture and the aperture efficiency can be defined. However, even in this case the internal power dissipated in his equivalent circuit can be equated to the power reradiated or scattered from the antenna. This is inappropriate since as occurs in Thevenin and Norton equivalent circuits, when the antenna is open-circuited, the scattered power is null, because there wouldn't be any internal dissipated power, but this is not physically true.

The same issue has been discussed in a more recent paper, e.g., by Li et al. in [46] with the aim of calculating the signal correlation of lossy Multiple Input Multiple Output (MIMO) antennas while taking into account antenna losses, including both conduction and dielectric losses.

Here they analyze the literature, citing the authors' works mentioned up to this point, and they propose a new method based on equivalent circuit to estimate correlation coefficients more accurately in lossy antenna arrays. In particular, having knowledge of the S-parameters and antenna efficiencies, loss components are separated from the original lossy antenna array and then appended to the lossless antenna ports as equivalent lumped resistors.

In lossless antennas, all the power that is accepted by the transmit antenna P_{in} is released into free space as radiated power P_{rad} ($P_{in}=P_{rad}$), but in practical lossy antennas, the non-ideal materials consume parts of the accepted power in the antenna system P_{loss} so that the radiated power is lower than the accepted one, i.e., $\eta_{rad} < 100\%$. The accepted power becomes $P_{in} = P_{rad} + P_{loss}$.

Equivalent circuit is an effective way to describe a lossy antenna system, where the inductance, capacitance, radiation resistance and loss resistance are distributed along the antenna structure.

In this proposed method a lumped resistor is connected in series or in parallel (depending on the antenna type) at each antenna port to approximate the losses in the original antenna.

Thus, the loss components are extracted based on the equivalent circuit from the measured S-parameters and antenna efficiencies, then, the transmission or ABCD matrix of each loss component is obtained and, finally, from the measured S-parameters of the original antenna array and the ABCD matrix, the S-parameters of the lossless antenna array (S') are extracted. The resulting network approximation is shown in Fig. 82 (a). In this procedure, the most critical step is the evaluation of the loss components from the equivalent circuit.

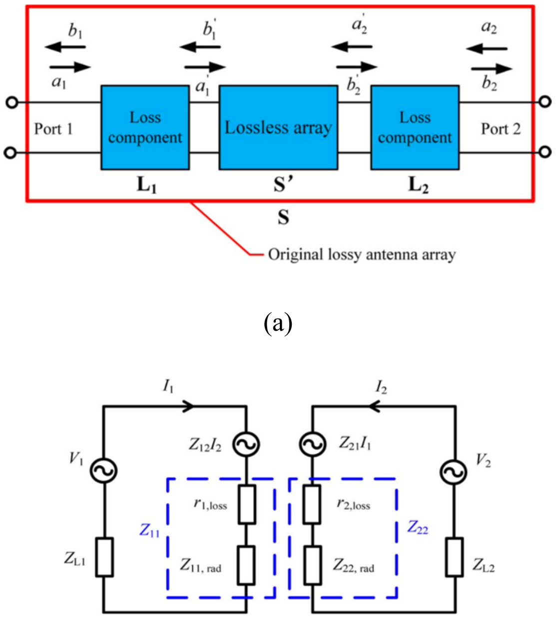

(a)

(b)

Fig. 82. (a) Network approximation of a lossy dual-antenna array where the antenna losses mainly occur in the vicinity of the ports, and (b) series equivalent circuit model of a lossy dual antenna array [46].

Depending on the impedance behavior of the antennas, series or parallel circuit are used to model them. If the impedance behavior of omnidirectional antennas, such as dipoles, is considered, these can be represented by a series RLC circuit, where the real part of the self-impedances Z_{11} and Z_{22} is divided into loss resistances $r_{1,loss}$ and $r_{2,loss}$, and radiation resistances $r_{1,rad}$ *and* $r_{2,rad}$, which are the real parts of $Z_{11,rad}$ and $Z_{22,rad}$ respectively, whereas Z_{12} and Z_{21} are the mutual impedances between the antennas, whose value increase for decreasing spacing between the antennas. The series equivalent circuit as described here is represented in Fig. 82 (b). The purpose of using the equivalent circuit is to determine the value of the loss resistances.
The two antennas are assumed to be identical, meaning $r_{1,loss} = r_{2,loss} = r_{loss}$, $r_{1,rad} = r_{2,rad} = r_{rad}$ and $Z_{L1} = Z_{L2} = Z_L$.

When the dual-antenna system is considered as a two-port network with port 2 loaded on Z_L and not excited, the total antenna efficiency is expressed as:

$$\boldsymbol{\eta_{1,tot} = \eta_{1,rad}\left(1 - |S_{11}|^2 - |S_{21}|^2\right)} \tag{62}$$

where the radiation efficiency $\eta_{1,rad}$ is calculated as:

$$\boldsymbol{\eta_{1,rad}} = \frac{\boldsymbol{P_{rad}}}{\boldsymbol{P_{in}}} = \frac{\boldsymbol{P_{rad}}}{\boldsymbol{P_{rad}} + \boldsymbol{P_{loss}}} = \frac{|\boldsymbol{I_1}|^2\boldsymbol{r_{rad}} + |\boldsymbol{I_2}|^2\boldsymbol{r_{rad}}}{|\boldsymbol{I_1}|^2\boldsymbol{r_{rad}} + |\boldsymbol{I_1}|^2\boldsymbol{r_{loss}} + |\boldsymbol{I_2}|^2\boldsymbol{r_{rad}} + |\boldsymbol{I_2}|^2\boldsymbol{r_{loss}}} = \frac{\boldsymbol{r_{rad}}}{\boldsymbol{r_{rad}} + \boldsymbol{r_{loss}}} \tag{63}$$

Whereas, when the dual antenna system is considered as a one port network, where Z_L at port 2 is a loss resistance consuming the accepted power, the total efficiency is given as:

$$\boldsymbol{\eta_{1,tot}} = \boldsymbol{\eta'_{1,rad}}(\mathbf{1} - |\boldsymbol{S_{11}}|^2) \tag{64}$$

where $\eta'_{1,rad}$ is evaluated as follows:

$$\boldsymbol{\eta'_{1,rad}} = \frac{\boldsymbol{P_{rad}}}{\boldsymbol{P_{rad}} + \boldsymbol{P'_{loss}}} = \frac{|\boldsymbol{I_1}|^2\boldsymbol{r_{rad}} + |\boldsymbol{I_2}|^2\boldsymbol{r_{rad}}}{|\boldsymbol{I_1}|^2\boldsymbol{r_{rad}} + |\boldsymbol{I_1}|^2\boldsymbol{r_{loss}} + |\boldsymbol{I_2}|^2\boldsymbol{r_{rad}} + |\boldsymbol{I_2}|^2\boldsymbol{r_{loss}} + |\boldsymbol{I_2}|^2\boldsymbol{Re}\{\boldsymbol{Z_L}\}} \tag{65}$$

Thus, the radiation efficiency can be obtained by the knowledge of the measured S-parameters and total efficiency, and then, having the radiation efficiency and the impedance matrix, the loss resistance can be calculated as follows:

$$\boldsymbol{r_{loss}} = \frac{\boldsymbol{\eta'_{1,rad}}\left(\mathbf{1} - \boldsymbol{\eta_{1,rad}}\right)\boldsymbol{Re}\{\boldsymbol{Z_L}\}}{(\boldsymbol{\eta_{1,rad}} - \boldsymbol{\eta'_{1,rad}})(\boldsymbol{k}^2 + \mathbf{1})} \tag{66}$$

where k is defined as

$$\boldsymbol{k} = \left|\frac{\boldsymbol{I_1}}{\boldsymbol{I_2}}\right| = \left|\frac{\boldsymbol{Z_{22}} + \boldsymbol{Z_L}}{\boldsymbol{Z_{21}}}\right| \tag{67}$$

After obtaining the loss resistances, the equivalent circuit can be used to obtain the scattering matrix of the lossless antenna.

Therefore, it can be concluded that in this method, the loss resistance considers both the ohmic losses and the losses due to the EM coupling between the two antennas composing the dual antenna array.

5.2.3. PROPOSED RECEIVING ANTENNA EQUIVALENT CIRCUIT

In this thesis, the issue of the equivalent circuit of a receiving antenna has been studied in order to correctly represent the EM simulated antenna when it is imported on the circuital nonlinear simulator and connected to the rectifier to carry out a nonlinear analysis of the overall rectenna system.

Starting from the equivalent circuit of a receiving antenna proposed by C.A. Balanis in [47], it has been investigated how the EM simulator used for simulating the receiving patch antenna, i.e. CST MS, evaluates the total and radiation efficiencies and which are the quantities taken into account in this calculation.

As mentioned in Chapter 5, Section 5.1.1, CST MS calculates the efficiencies of the antenna when used as a transmitter. The power provided at the antenna port by a signal generator is called Stimulated Power and a portion of it is accepted by the antenna, Power Accepted, whereas the rest of it is reflected depending on the matching conditions between the antenna and its feeding line. Then, part of the Power Accepted by the antenna is lost due to dielectric and conductor losses and the remaining part is radiated, Radiated Power, as represented in Fig. 36 which better clarifies this power subdivision.

The radiation efficiency is evaluated as the ratio between the Power Radiated and the Power Accepted, mainly considering the losses due to dielectrics and metals, whereas the total efficiency takes into account also the mismatch at the antenna port, thus it is the ratio between the Power Radiated and the Power Stimulated. This means that these two quantities are equal only in the case of an antenna in perfect matching conditions.

It is clear from this brief insight that is not possible to determine, on the basis of these quantities, the amount of power reradiated by the antenna when this is used in receiving mode, which is why it has not been considered in the representation of the receiving antenna equivalent circuit described in this work.

In fact, the proposed equivalent receiving antenna circuit is shown in Fig. 83 and it is composed of the Touchstone file of the antenna containing the results of the EM simulation exported from CST, connected to a single-frequency excitation power source which represents the wave incident to the antenna. The internal impedance of the generator has been chosen in order to be equal to the antenna radiation resistance R_T, so that it considers the conductor and dielectric losses:

$$\boldsymbol{R_T = \eta_{rad}(R_T + R_J)} \tag{68}$$

where $R_T + R_J = R_A$ is the real part of the antenna input impedance and η_{rad} is the patch antenna radiation efficiency obtained by the CST EM simulation.

Another negative resistance $-R_T$ has been added in between the generator and the antenna .s1p Touchstone file so that the radiation resistance is not considered twice, since it is already present in the .s1p itself.

The radiation efficiency has been used instead of the total efficiency because the latter takes into account also the matching of the antenna impedance with the characteristic feeding line impedance.

In fact, in the case of absence of an external matching network between the antenna and the rectifier, the antenna impedance has to be conjugate-matched to the input impedance of the rectifier; on the other hand, with the presence of a real matching network composed of lumped/distributed elements, the antenna impedance is matched by means of the matching network itself.

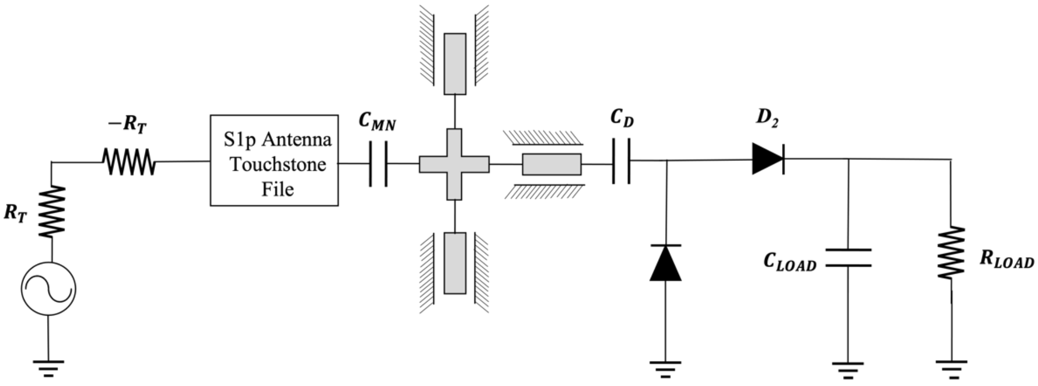

(a)

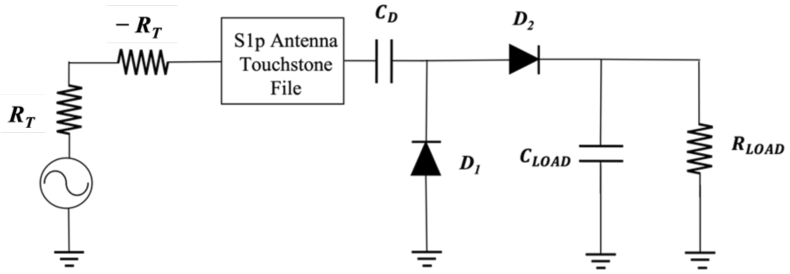

(b)

Fig. 83. Schematic of the antenna-rectifier equivalent circuit (a) with external matching network, and (b) with the antenna conjugate-matched to the rectifier.

5.2.4. RECTENNA SIMULATED RESULTS

Among the different antenna layouts presented in Chapter 5, the one with best radiation performances has been selected for the rectenna design. As summarized in TABLE XVII, the coplanar-fed patch antenna operating at 2.45 GHz (Section 5.1.7) shows the best results, with a radiation efficiency of 64%.

As previously mentioned, since one of the main objectives of this thesis is to minimize the dielectric losses caused by the high loss tangent of Flexible80A, here are proposed two rectenna designs: one having the antenna input impedance matched to the typical 50 Ω feeding line and with an external hybrid matching network (distributed components in GCPW technology and a capacitor), placed in between the antenna and the rectifier, in order to match the antenna input impedance to the rectifier one, Fig. 83 (a), and the other rectenna with the antenna input impedance conjugate-matched to the rectifier's one, Fig. 83 (b). In fact, since the introduction of an external matching network increases the cost, the size, and the losses of the overall rectenna structure, its elimination has resulted to be advantageous, also because of the fact that the structure is no longer constrained to the 50 Ω traditional characteristic impedance.

In the latter case, the antenna parameters have been tuned in order to reach an input impedance matching the rectifier's one without much compromising the radiation characteristics.

The chosen rectifier topology in both the projects is the voltage doubler, illustrated in Fig. 76 (a), which allows to produce an output voltage almost twice greater than the one applied at the input. The Schottky diode models used in the voltage-doubler is the Skyworks SMS7630-079LF, represented in Fig. 84 with its parasitic components defined at 2.45 GHz, namely an inductor (L = 1 nH) and a capacitor (C = 0.275 pF), which significantly impact the diode performance at higher frequencies. In TABLE XVIII are reported the characteristics of the abovementioned diodes.

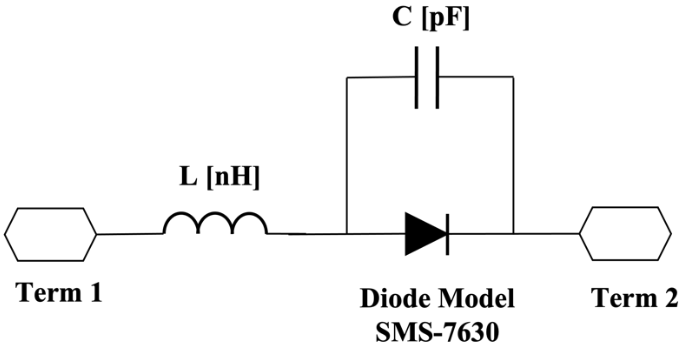

Fig. 84. Schottky Diode model of the Skyworks SMS7630-079LF with the corresponding parasitic components at 2.45 GHz.

TABLE XVIII. SCHOTTKY DIODE MODEL OF THE SMS-7630 AT 2.45 GHz

Description	***Abbreviation***	***Value***
Saturation current	I_s	0.005 mA
Ohmic resistance	R_s	20 Ω
Emission Coefficient	N	1.05
Transient Time	T_t	0.01 nsec
Zero-bias Junction Capacitor	C_{j0}	0.14 pF
Junction Potential	V_j	0.34 V
Grading Coefficient	M	0.4
Forward-bias Depletion Capacitor Coefficient	F_c	0.5
Breakdown Voltage	B_v	3.5 V
Current at Reverse Breakdown Voltage	I_{bv}	0.1 mA
Energy Gap	E_g	0.69 eV

These two rectennas have been designed and simulated by means of the HB simulation on Keysight ADS up to the eighth harmonic.

In order to have a fair comparison between the two rectenna designs, two antennas both operating in the 2.45 GHz band have been used but showing different input impedances to be matched in one case with the typical 50 Ω impedance, and in the other case directly with the rectifier.

For the rectenna with a 50-Ω patch antenna and external matching network, it has been chosen to use the same antenna layout of the coplanar-fed patch antenna operating at 2.45 GHz (Section 5.1.7), shown in Fig. 68, but with squared dimensions, so that the obtained radiation efficiency could be comparable to the one obtained in the antenna with input impedance conjugate matched to that of the rectifier. Thus, the length and the width of the patch antenna shown in Fig. 68 are equal to 52 mm. The resulting antenna input impedance $Z_A = 52 + j14.7$ is matched to the 50-Ω feeding transmission line and has a simulated radiation efficiency of 57%, as depicted in Fig. 85 and Fig. 86, respectively. Thus, the radiation resistance R_T, evaluated using expression (68), is equal to 24.65 Ω. This value has been set as internal impedance of the generator connected to the antenna and it's opposite (–24.65 Ω) as value of the negative resistance $-R_T$ which allows to consider it only once.

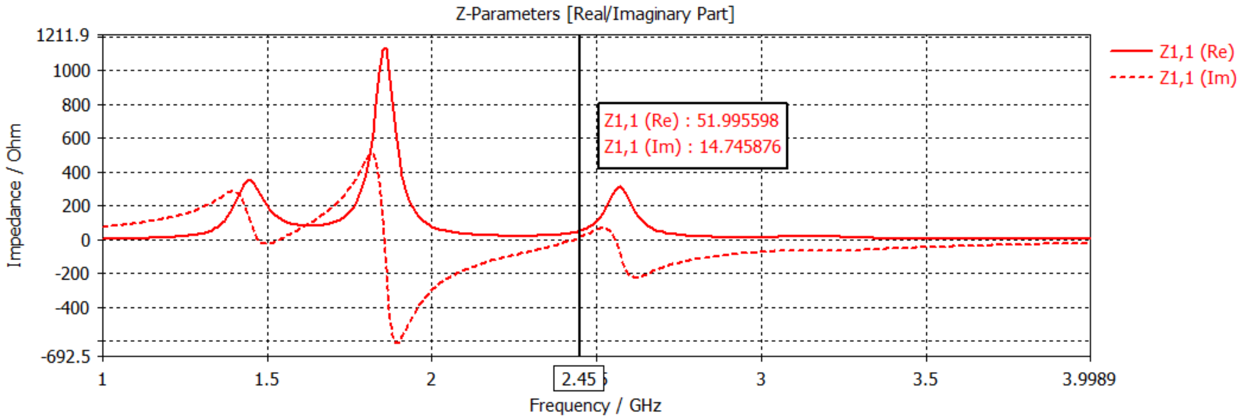

Fig. 85. Z_{11} parameter of the coplanar-fed patch antenna with squared dimensions operating at 2.45 GHz.

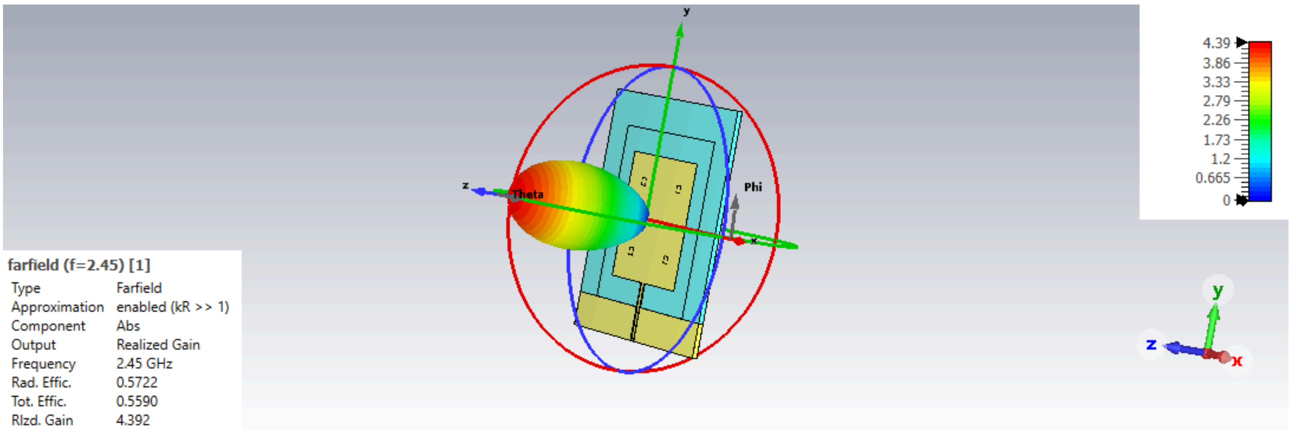

farfield (f=2.45) [1]

Type	Farfield
Approximation	enabled (kR >> 1)
Component	Abs
Output	Realized Gain
Frequency	2.45 GHz
Rad. Effic.	0.5722
Tot. Effic.	0.5590
Rlzd. Gain	4.392

Fig. 86. Far-field results of the coplanar-fed patch antenna with squared dimensions operating at 2.45 GHz.

The antenna input impedance is then matched to the rectifier's one by means of an external matching network in GCPW technology. The choice of using GCPW is compliant to the study presented in Chapter 4, thus adopting the etching technique of the substrate in the gaps to reduce the dielectric losses. The external matching network has been realized with an input capacitor (C_{MN} = 1.32 pF), two 50-Ω open stubs in GPCW technology (length: 10.64 mm each), and a 50-Ω grounded coplanar waveguide (length: 19.4 mm). The optimum load of the rectifier is about 1.624 kΩ.

Conversely, in the rectenna where the antenna has been directly attached to the rectifier through the conjugate-matching technique, the coplanar-fed patch antenna operating at 2.45 GHz (Section 5.1.7) has been slightly changed in order to obtain an input impedance Z_A that matches, as much as possible, the rectifier input impedance Z_{rec}, for a selected rectifier input power range. This step is not straightforward because of the fact that the rectifier is a nonlinear circuit, thus, the input impedance not only varies with frequency, but also with the input power and must be accounted for in the nonlinear/EM co-design process.

Therefore, an accurate nonlinear analysis of the rectifier input impedance variation at the operating frequency of 2.45 GHz, in the input power range –20 to 10 dBm has been carried out when the rectifier is not yet connected to the antenna. In Fig. 87 the analysis results are shown, and it can be observed that the real and imaginary parts of the rectifier impedance vary respectively in the ranges [4.9 ÷ 38] Ω and [–70 ÷ –57] Ω.

It is worth noticing that the imaginary part of the rectifier input impedance has a very little variation in the input power range considered. Thus, the best-compromise choice must be taken.

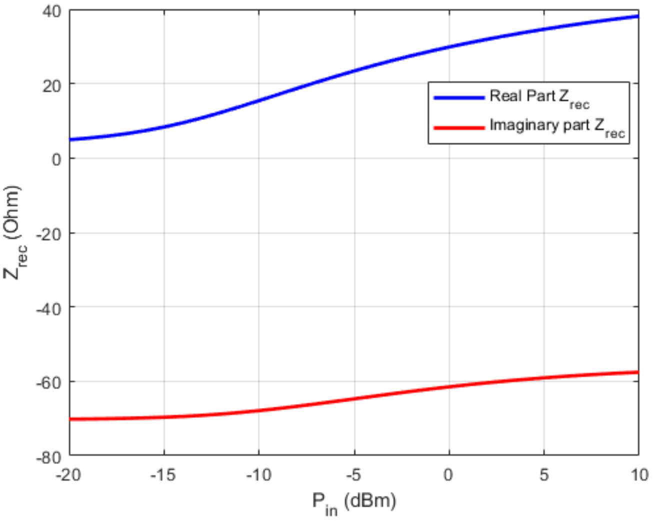

Fig. 87. Simulated Rectifier complex input impedance versus the rectifier input power P_{in}.

The coplanar-fed patch antenna, whose input impedance is intended to be conjugate-matched to the rectifier input one, is shown in Fig. 88 and its dimensions are described in TABLE XIX. As stated, it has been tried to find an input impedance of the antenna which matched as much as possible that of the rectifier by changing its design parameters, while maintaining almost the same radiation performance. In particular, many different attempts have been made, varying the length and the width of the patch itself, or even introducing the inset feeds with different lengths. At last, setting the dimensions of the squared patch to 53 mm has led to an antenna impedance $Z_A = 82.5 + j30.4$, reported in Fig. 89, which doesn't fall within the abovementioned ranges of the real and imaginary parts of the rectifier input impedance, but it is the best compromise achieved through the EM simulation.

As regards the far-field results of the antenna conjugate matched to the rectifier, shown in Fig. 90, the radiation efficiency has been found to be slightly lower, i.e., 51% , thus, not so different from the 57% of radiation efficiency obtained for the 50-Ω antenna.

Finally, an optimization analysis of the rectenna realized with conjugate matching has been carried out, obtaining a short-circuited stub of length (L_{stub}) 17.6 mm, width of the line of 1.88 mm and gap between the line and the coplanar ground equal to 0.2 mm, the two rectifier capacitors (C_D and C_{LOAD}) are both equal to 1 pF, and the optimum load (R_{LOAD}) has resulted to be 737 Ω.

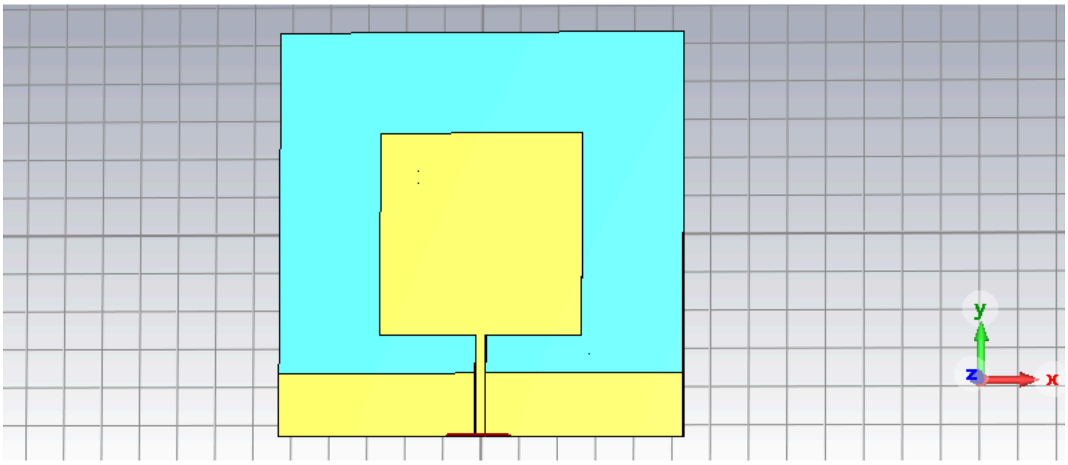

Fig. 88. Coplanar-fed patch antenna at 2.45 GHz designed to achieve an input impedance conjugate matched to the one of the rectifier.

TABLE XIX. COPLANAR-FED PATCH ANTENNA CONJUGATE MATCHED TO THE RECTIFIER OPERATING AT 2.45 GHZ: GEOMETRIC DIMENSIONS

Antenna Design Parameters	
Description	***Value***
Substrate Height	2 mm
Copper thickness	31.8 µm
Patch length	53 mm
Patch width	53 mm
GCPW width	2.4 mm
Gap between the transmission line and the coplanar ground	0.2 mm
Gap between the bottom patch edge and the coplanar ground	10 mm
Depth of the substrate etchings in the coplanar gaps	1.7 mm
Depth of the substrate etching below the patch and below the feeding line	1.4 mm
Thickness of substrate layer kept on top and at the bottom of the substrate in correspondence of the etchings	0.3 mm
Side of the squared pillars	4 mm

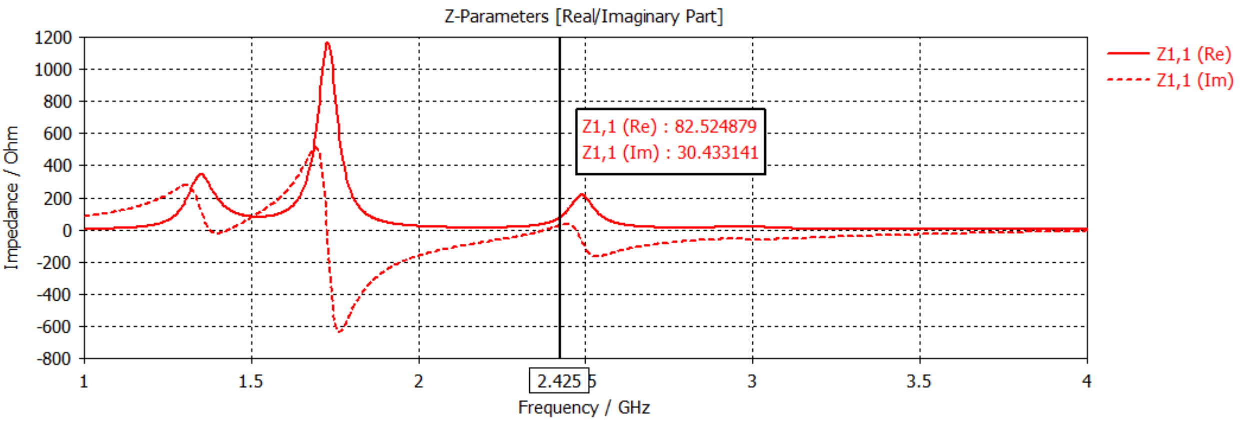

Fig. 89. Z_{11} parameter of the coplanar-fed patch antenna at 2.45 GHz designed to achieve an input impedance conjugate matched to the rectifier one.

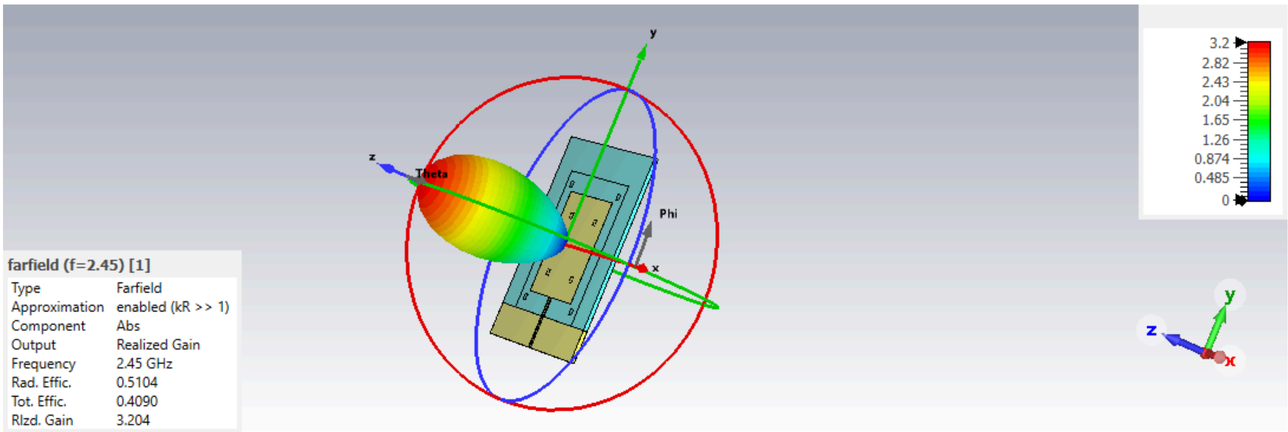

farfield (f=2.45) [1]

Type	Farfield
Approximation	enabled (kR >> 1)
Component	Abs
Output	Realized Gain
Frequency	2.45 GHz
Rad. Effic.	0.5104
Tot. Effic.	0.4090
Rlzd. Gain	3.204

Fig. 90. Far-field results of the coplanar-fed patch antenna conjugate matched to the rectifier, operating at 2.45 GHz.

TABLE XX. COPLANAR-FED PATCH ANTENNA CONJUGATE MATCHED TO THE RECTIFIER OPERATING AT 2.45 GHZ PERFORMANCE

Radiation Performance of the Coplanar Fed Patch Antenna operating at 2.45 GHz	
Description	***Value***
Realized Gain	5.1 dBi
Radiation Efficiency	51%
Total Efficiency	41%

The overall rectenna performance has been evaluated by means of the following figures of merit: the rectified dc output power P_{out}, the rectifier power conversion efficiency η_{rec} and the rectenna power conversion efficiency η_{tot} (in percentage), which are respectively calculated as follows:

$$\boldsymbol{P_{out} = Re\left\{\frac{V_{out}{}^{2}}{R_{load}}\right\}} \tag{69}$$

where V_{out} is the dc voltage across the load resistance R_{LOAD},

$$\boldsymbol{\eta_{rec} = 100 \cdot \frac{P_{out}}{P_{rec}}} \tag{70}$$

where P_{rec} is the power actually entering the rectifier, thus, a portion of the input power P_{in} received by the antenna. The power received by the antenna, P_{in}, in the ADS schematic is the input power made available by the generator.

$$\boldsymbol{\eta_{tot} = 100 \cdot \frac{P_{out}}{P_{in}}} \tag{71}$$

Fig. 91 (a) shows the comparison of the overall rectenna efficiency η_{tot} plotted versus the power which is received by the antenna (P_{in}), achieved with the two design approaches, and specifically with external matching network and with the antenna conjugate-matched to the rectifier. It can be observed that the efficiency of the rectenna with antenna conjugate matched to the rectifier outperforms the one with external matching network from 0 dBm of P_{in} onwards, demonstrating that for this input power range, the removal of the matching network can actually reduce the losses caused by the latter.

However, in Fig. 91 (b) is illustrated the comparison of the rectifier efficiency η_{rec} achieved in the two cases plotted versus the power actually entering the rectifier (P_{rec}), showing that in the case of external matching network η_{rec} with $P_{rec} = 0$ dBm is about 13% higher than in the case of antenna conjugate matched to the rectifier due to the mismatch caused by the imperfect conjugate matching, which results in part of the P_{rec} being reflected.

Finally, the rectenna and rectifier efficiency results are confirmed by the plots in Fig. 91 (c) and Fig. 91 (d), which show respectively the rectified output power P_{out} with respect to the power received by the antenna P_{in}, and the variation of power entering the rectifier P_{rec} versus the received power P_{in}.

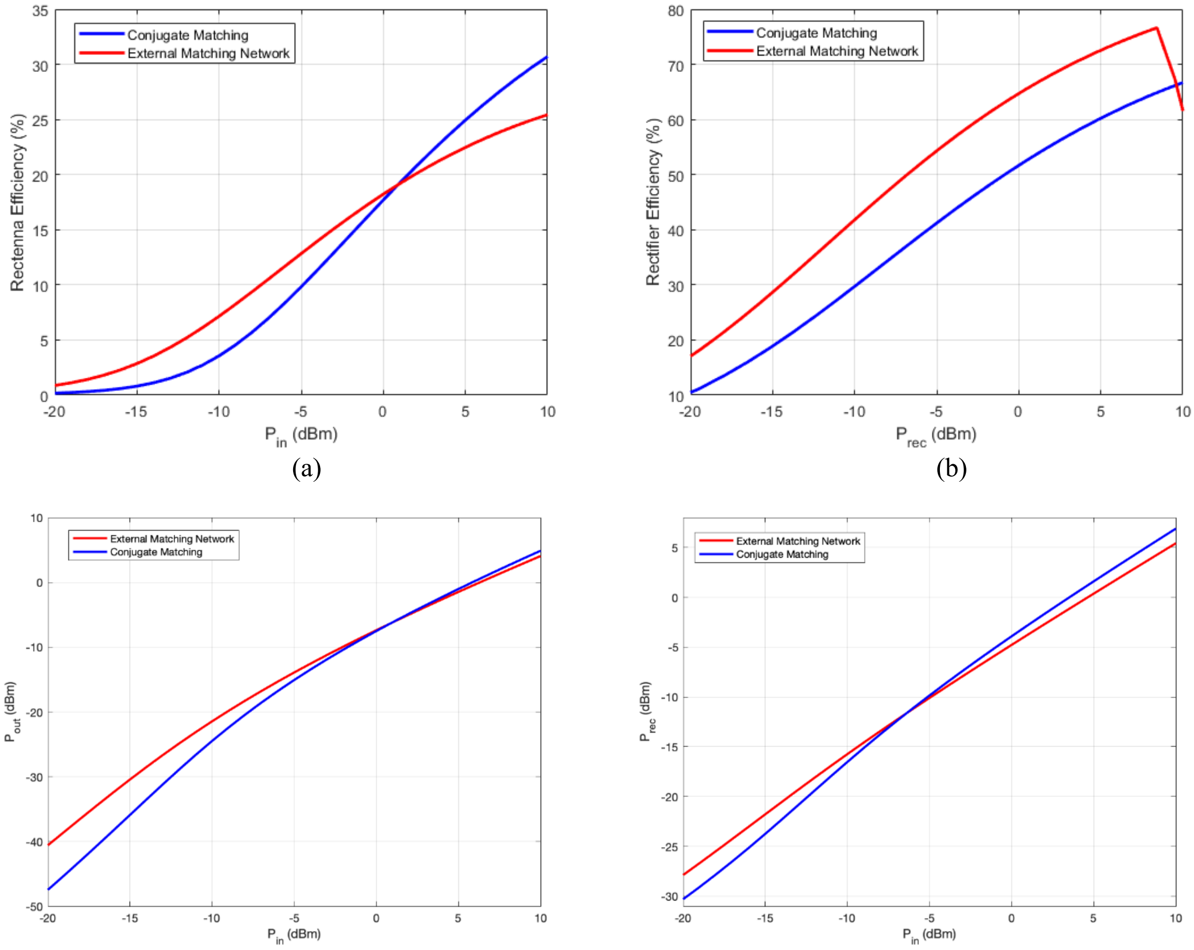

(a)

(b)

(c)

(d)

Fig. 91. (a) Comparison of the rectenna power conversion efficiency (%) achieved in the two design approaches for different values of power received by the antenna (P_{in}); (b) comparison of the rectifier power conversion efficiency versus the power entering the rectifier (P_{rec}) and (c) dc output power (P_{out}) versus antenna received power (P_{in}), and (d) variation of the rectifier input power (P_{rec}) versus P_{in}.

5.2.5. RECTENNA MEASURED RESULTS

To provide an example of the measured results that can be obtained by a 2.45 GHz rectenna fabricated with adhesive copper on Flexible80A with the antenna directly conjugate matched to the rectifier input impedance, it has been chosen to 3D-print a substrate sample of dimensions 13.5 x 14 cm^2 and 2 mm-thick, having the same substrate layout simulated in Chapter 5.1, Section 5.1.5: the coplanar-fed patch antenna with a pattern of squared 4 mm-side etchings inside the dielectric material, illustrated in Fig. 58, with the aim of reducing the insertion loss and the effective dielectric permittivity of the material and improve the antenna radiation efficiency.

Also the gaps between the transmission line and the coplanar ground have been maintained the same trapezoidal shape and size of the ones illustrated in Fig. 51.

The patch antenna has been previously design and EM simulated on CST MS in order to achieve an input impedance conjugate matched as much as possible to that of the rectifier at the operating frequency of 2.45 GHz. The rectifier input impedance behavior has been simulated on Keysight ADS by means of a nonlinear HB simulation in the power range going from –20 to 10 dBm and in Fig. 87 the analysis results are shown, where it can be observed that the real and imaginary parts of the rectifier input impedance vary respectively in the ranges [4.9 ÷ 38] Ω and [–70 ÷ –57] Ω.

The simulated antenna is illustrated in Fig. 92 (a) and its length and width dimensions, equal to 40 mm (L_p) and 20 mm (W_p) respectively, have been tuned to vary the input impedance, whereas the remaining antenna design parameters are the same reported in TABLE XI. The best conjugate matching result has been obtained at the frequency of 2.66 GHz and corresponds to a simulated $Z_A = 70.2 + j41.9\ \Omega$, as depicted in Fig. 92 (c), (d). The far-field simulation results are reported in Fig. 92 (e) and show a 14% of radiation efficiency and a realized gain of –1.3 dBi.

Moreover, the patch antenna alone, disconnected from the rectifier, illustrated in Fig. 94, has been measured and the comparison between the measured and simulated $|S_{11}|$, Re(Z_{11}) and Im(Z_{11}) curves (where Z_{11} corresponds to the antenna input impedance that has been called Z_A) are reported in Fig. 92 (b), (c) and (d), respectively. As can be noticed from the comparison in Fig. 92 (b), the measured and simulated $|S_{11}|$ curves have the main resonance at the same frequency of about 2.55 GHz, where the antenna is matched to the 50-Ω feeding transmission line.

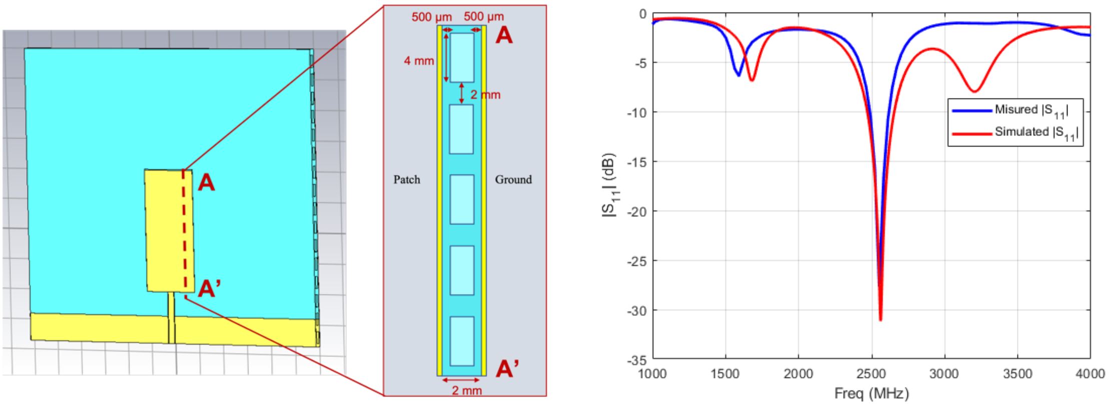

(a) (b)

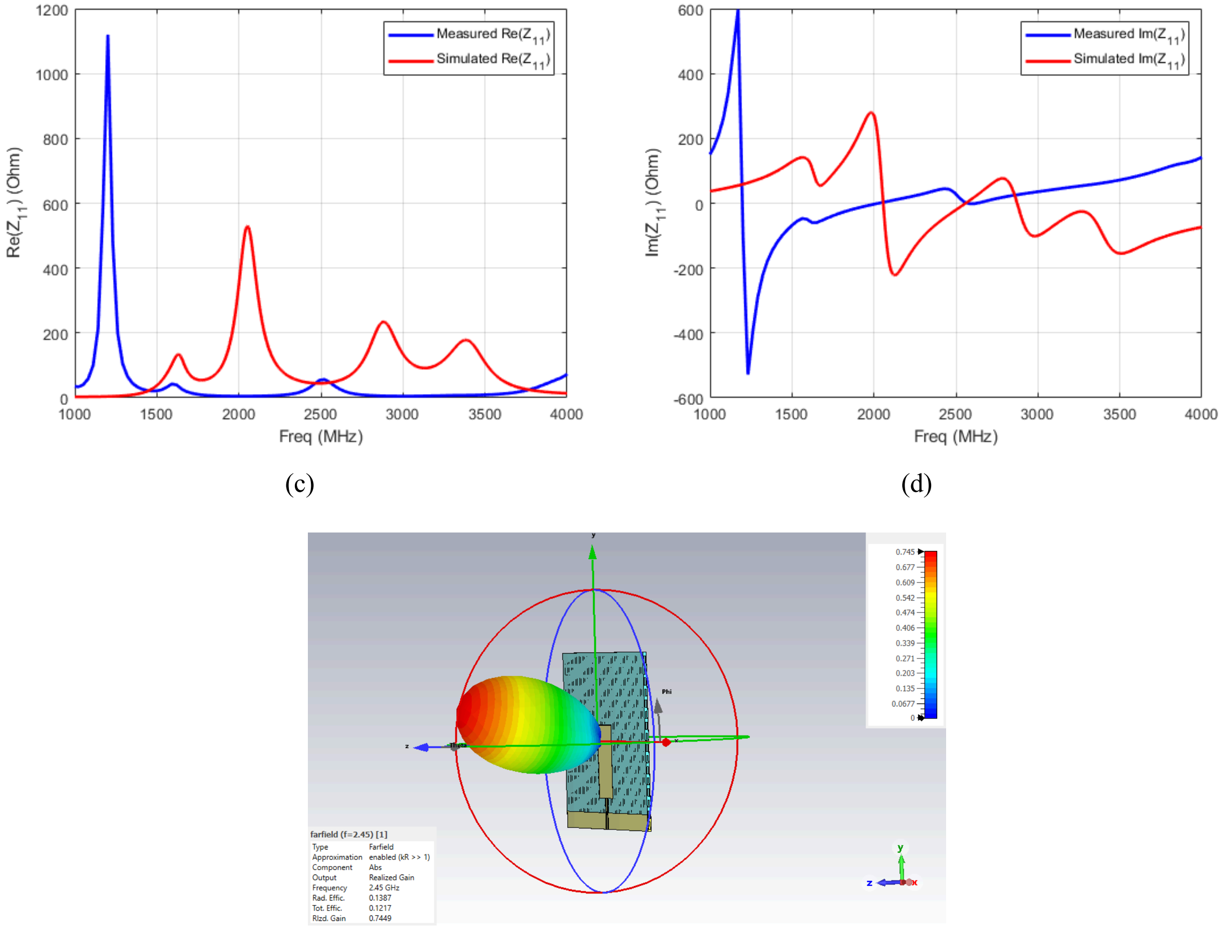

(c)

(d)

farfield (f=2.45) [1]
Type Farfield
Approximation enabled (kR >> 1)
Component Abs
Output Realized Gain
Frequency 2.45 GHz
Rad. Effic. 0.1387
Tot. Effic. 0.1217
Rlzd. Gain 0.7449

(e)

Fig. 92. (a) Layout of the designed coplanar-fed patch antenna conjugate matched to the rectifier, with a callout on the weft of the trasversal section of the substrate; comparison between measured and simulated curves of (b) |S_{11}| parameter, (c) Re(Z_{11}), (d) Im(Z_{11}) of the coplanar-fed patch antenna conjugate matched to the rectifier; (e) far-field results of the coplanar-fed patch antenna.

The patch antenna Touchstone file has been exported from CST and imported on Keysight ADS in order to connect it directly to the rectifier, as illustrated in Fig. 83 (c), and perform a nonlinear HB simulation of the overall rectenna circuit at the operating frequency of 2.66 GHz and in the input power range –20 ÷ 10 dBm. The optimum load resulting from the HB analysis is 935 Ω.

The figures of merit observed are the rectenna efficiency, evaluated as reported in expression (71), and the dc output voltage V_{out} (V), which are plotted in Fig. 93(a) and (b) respectively, where it can be noticed that at 0 dBm of input power (the power received by the antenna), the rectenna shows an efficiency of 2.45%, corresponding to a dc output voltage of 151 mV.

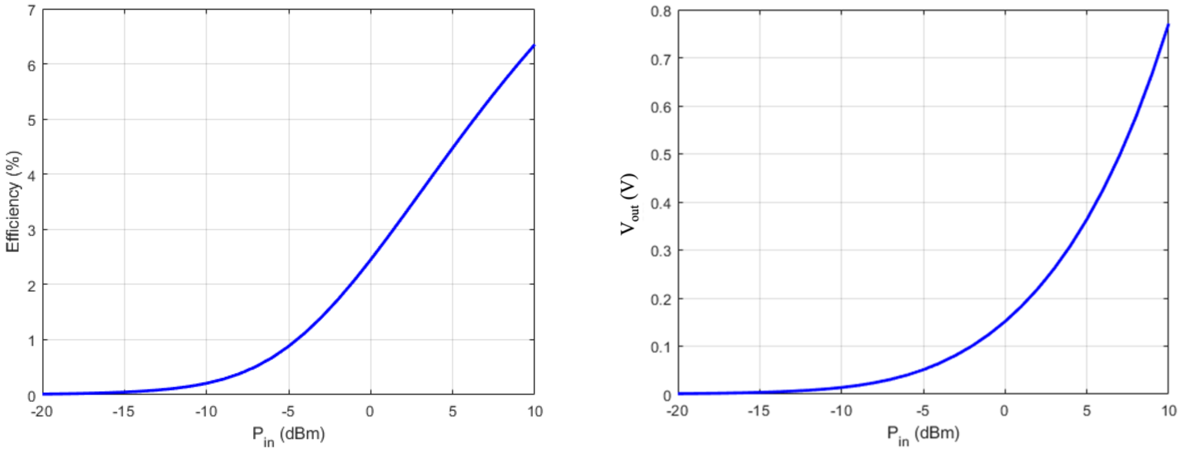

(a) (b)

Fig. 93. (a) Simulated efficiency and (b) output voltage of the rectenna with antenna input impedance conjugate matched to that of the rectifier.

Now, as stated, to validate these results, this same rectenna has been fabricated with adhesive copper on a 3D-printed sample of Flexible80A, as shown in Fig. 94 (a), and its efficiency and output voltage have been measured. The measurement setup is the same schematized in Fig. 77 (b) and pictured in Fig. 94 (b).

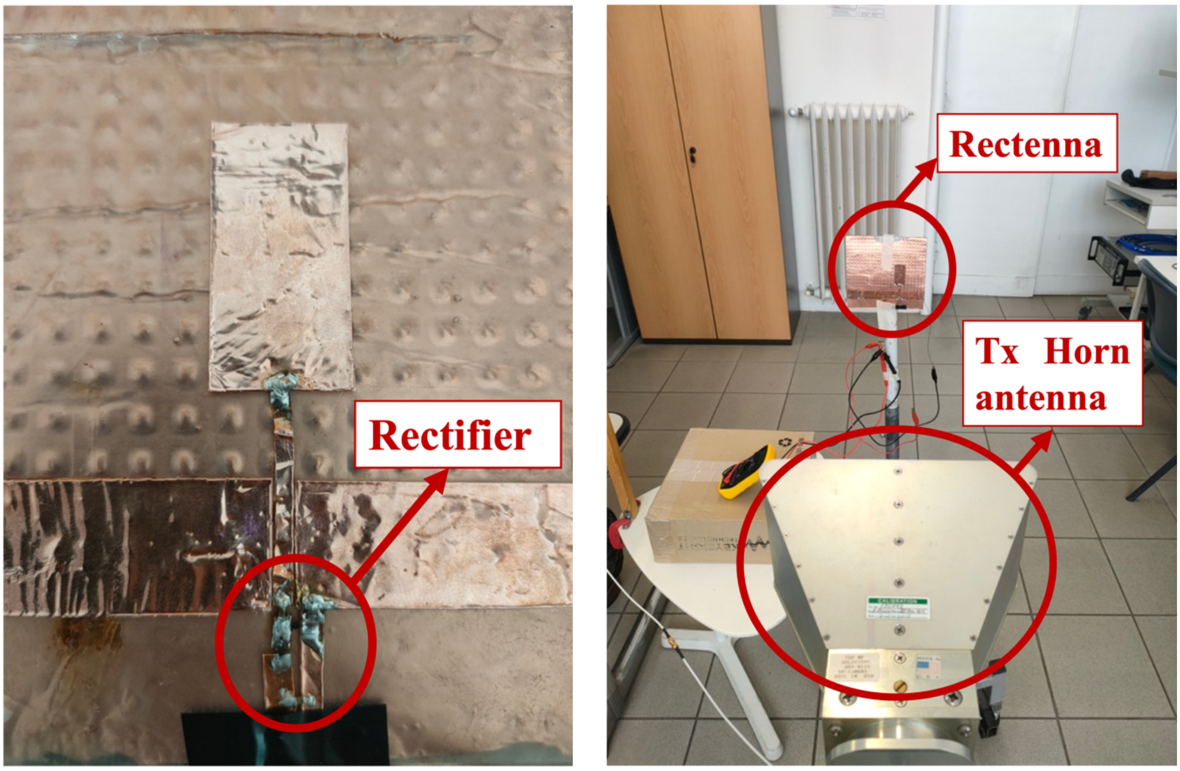

(a) (b)

Fig. 94. (a) Picture of the fabricated rectenna and (b) measurement setup.

The transmitting antenna which has been used for measurement purposes is the TDK HRN-0118 broadband horn antenna (1 to 18 GHz), which has a gain of 10.1 dBi at 2.45 GHz.
The receiving antenna gain, has, instead, been calculated by means of the three-antenna-gain-measurement technique, consisting of determining the unknown gain of an antenna by firstly measuring the power received at a given frequency and at a given transmitted power value when the transmitting and receiving antenna gains are well known from a datasheet or from literature, and then, changing the receiving antenna with the one whose gain has to be evaluated and measuring the received power. The difference between the two results is the gain of the antenna which had to be measured. Thus, the receiving coplanar-fed patch antenna gain resulting from this measurement has resulted to be –0.8 dBi.

The measures have been performed at a distance of 60 and 41.5 cm between the rectenna and the transmitting horn antenna; the rectenna efficiency and rectified output voltage have been measured and plotted in the two cases.

The measurements results of the rectenna at the distance of 60 cm from the horn antenna and at the frequency of 2.46 GHz (the frequency at which was measured the highest rectenna efficiency) with an optimum load of 900 Ω, are reported in Fig. 95 (a) and (b), respectively, versus the power incident at the receiving antenna, thus, P_{in}.
The power in the plot abscissa has been calculated as the power incident to the receiving antenna, evaluated by measuring the power received by an antenna whose gain is known (quarter wavelength monopole) and then subtracting to this value it gain.
A first appreciation is that the efficiency is much higher than the simulated performance, and this is partly because of the measured antenna gain being a little higher than the simulated one, and partly due to the measured antenna impedance having a value better conjugate matched to the rectifier's one; in fact it can be observed from *Fig. 92* (c) and (d), that the input impedance of the measured antenna at 2.46 GHz is $Z_A = 43.7 + j42.3\ \Omega$, thus much closer to the rectifier input impedance range of values for the input power range considered. This results in having a rectenna efficiency of about 12.5% at –10 dBm of power incident to the receiving antenna, corresponding to a dc output voltage of about 100 mV.

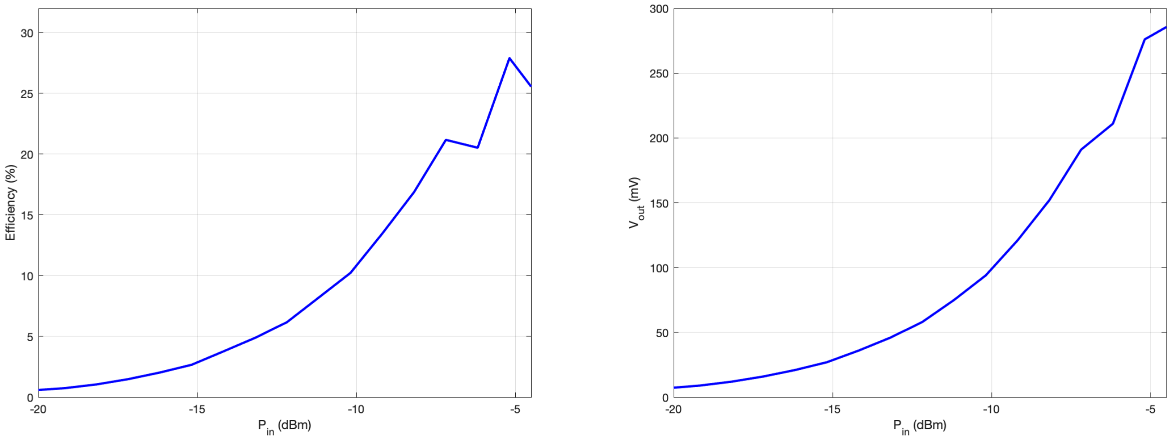

(a) (b)

Fig. 95. Measured (a) efficiency and (b) rectified output voltage of the rectenna pictured in Fig. 94 (a) at a distance of 60 cm.

To have higher power received by the antenna, the distance has been reduced to 41.5 cm and the optimum load has been measured at the frequency of 2.46 GHz and for a level of power incident to the antenna equal to –14 dBm. In Fig. 96 is shown the measured PCE (%) versus different values of load resistance R_L spanning from 199 to 1959 Ω; it can be appreciated that the highest efficiency corresponds to an optimum load resistance of about 570 Ω.

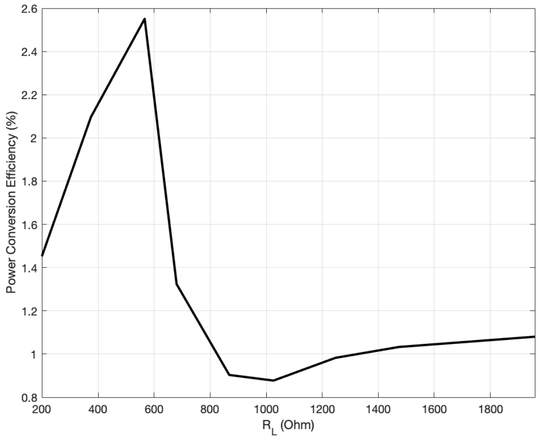

Fig. 96. Measured PCE versus different values of load resistance R_L.

Finally, the measured efficiency and dc output voltage of the rectenna at the distance of 41.5 cm and at the operating frequency of 2.46 GHz, with the optimum load of 600 Ω, have been plotted in Fig. 97, showing that the rectenna efficiency at –14 dBm of P_{in} is about 2.7%, consistently with the results of the optimum rectenna load shown in Fig. 96, and a rectified output voltage of about 25 mV.

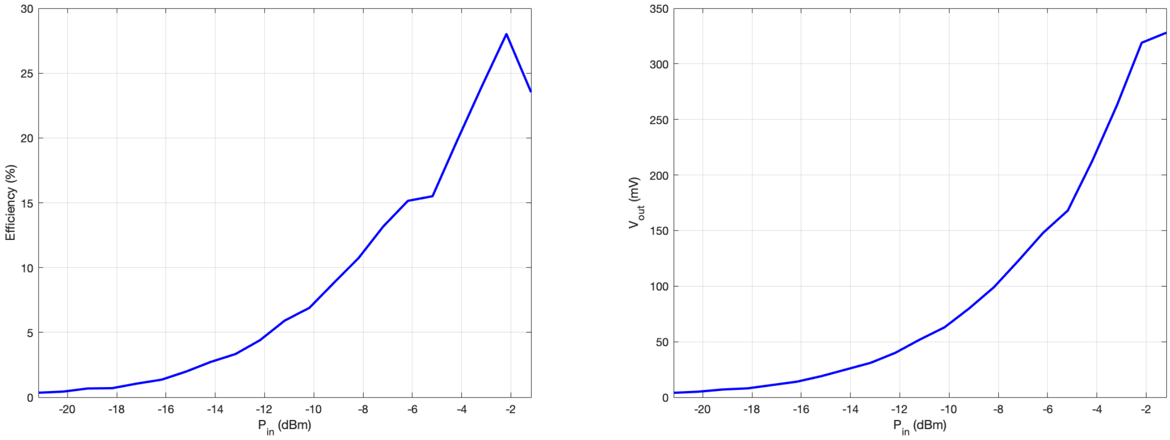

(a) (b)

Fig. 97. Measured (a) efficiency and (b) rectified output voltage of the rectenna pictured in Fig. 94 (a) at a distance of 41.5 cm.

6. CONCLUSIONS

The work presented in this thesis is aimed at revealing the exceptional potentialities of 3D-printing technologies in the research for innovative inexpensive, biocompatible, soft, and flexible materials and customization techniques that can be used for the realization of wireless, battery-free, wearable, bio-integrated devices and sensors for a wide range of RF WPT and EH applications across clinical, commercial and research domains.

In particular, a new 3D-printable, low-cost, resin material, the Flexible80A, is proposed as RF substrate material in the implementation of a wearable, lightweight and miniaturized rectenna operating at 2.45 GHz for WPT applications.

A careful and accurate EM characterization of the Flexible80A, carried out using the T-resonator method and revealing it to be a very lossy substrate, has paved the way for the investigation of innovative transmission line and antenna layouts as well as etching techniques for improving the wave propagation performance within such lossy materials.

To begin with, a first overview about guided propagation and planar transmission lines theory has been reported in order to compare different transmission lines topologies and choose the one which could benefit the most despite this kind of lossy substrate. In particular, a comparison between GCPW and microstrip technologies has brought up that the former, being the electric field mostly confined in the gaps between the line and the coplanar ground and penetrating less the material , provides better propagation performances with respect to the latter. Moreover, exploiting the design freedom enabled by 3D-printing technologies, new substrate etching techniques have been studied with the objective of obtaining a wave propagation performance inside the lossy dielectric, as much as possible comparable to that obtained in a low-loss substrate material.

This analysis has been crucial in the design process of a patch antenna, meant to be successively connected to the rectifier. In fact, many different patch antenna layouts have been explored varying the antenna dimensions, the substrate etchings shape and position, the feeding line technology and the operating frequency. The final antenna design showing the highest efficiency performances, i.e. 64% of radiation efficiency, has resulted to be a coplanar-fed patch antenna operating at 2.45 GHz on a substrate having the EM properties obtained by the Flexible80A material characterization previously carried out, and inside of which the dielectric material has been partially removed without affecting the overall structure stability but, instead, providing the wave propagation benefits observed by the abovementioned investigations. The antennas design and simulations have been performed on the EM simulator CST MS in the frequency domain.

The issue of optimizing the antenna radiation efficiency has been crucial for the design of a rectenna meant for WPT and EH applications, where the efficiency of each single stage has to be maximized in order to achieve the best rectification performances allowing to provide high power levels to the sensor to which it has to be delivered.

Before dealing with the rectification stage of the rectenna design, the hot and long-discussed topic of the equivalent receiving antenna circuit representation has been addressed, providing an overview of the interpretation of many different microwave and RF design authors about the issue, and the position which has been adopted in this thesis.

Furthermore, two rectenna designs have been proposed with the aim of minimizing the dielectric losses caused by the high loss tangent of Flexible80A; one, having the antenna input impedance matched to the typical 50 Ω feeding line and with an external hybrid matching network placed in between the antenna and the rectifier, in order to match the antenna input impedance to the rectifier's one, the other, a rectenna with the antenna input impedance directly conjugate-matched to the rectifier's one.

The comparison between the rectenna efficiencies obtained with the two approaches shows that the introduction of an external matching network increases the cost, the size, and the losses of the overall rectenna structure, and can provide better rectification performances at lower input power levels (up

to 0 dBm of power received by the antenna); however, its elimination has resulted to be advantageous for input power levels above 0 dBm, also providing a miniaturized, inexpensive structure no longer constrained to the 50 Ω traditional characteristic impedance.
Finally, a prototype of a rectenna with the antenna conjugate matched to the rectifier, operating at 2.45 GHz, has been fabricated with adhesive copper on a substrate sample of Flexible80A and measured, in order to validate the simulated results. The obtained measurements have resulted to be even better than the simulated ones, showing a rectenna efficiency of about 10 % at -10 dBm of power incident to the receiving antenna.

Therefore, with this thesis it has been demonstrated that 3D-printing technologies can be considered significantly attractive in the production of microwave, biocompatible and wearable devices and in the antennas design and fabrication, with the intention of making them lightweight, inexpensive, flexible and easily integrable, replacing the use of stiff, difficult to process, and very expensive materials traditionally used as substrates for the production of wireless wearable sensors for vital signals monitoring.

BIBLIOGRAPHY

[1] T. R. Ray *et al.*, «Bio-Integrated Wearable Systems: A Comprehensive Review», *Chem. Rev.*, vol. 119, n. 8, pp. 5461–5533, 2019, doi: 10.1021/acs.chemrev.8b00573.

[2] S. Cheng *et al.*, «Recent Progress in Intelligent Wearable Sensors for Health Monitoring and Wound Healing Based on Biofluids», *Front. Bioeng. Biotechnol.*, vol. 9, 2021, doi: 10.3389/fbioe.2021.765987.

[3] S. M. Won, L. Cai, P. Gutruf, and J. A. Rogers, «Wireless and battery-free technologies for neuroengineering», *Nat. Biomed. Eng.*, Mar. 2021, doi: 10.1038/s41551-021-00683-3.

[4] S. Khan, S. Ali, and A. Bermak, «Recent Developments in Printing Flexible and Wearable Sensing Electronics for Healthcare Applications», *Sensors*, vol. 19, n. 5, 2019, doi: 10.3390/s19051230.

[5] C. Hassler, T. Boretius, and T. Stieglitz, «Polymers for Neural Implants», *J. Polym. Sci. Part B Polym. Phys.*, vol. 49, pp. 18–33, Jan. 2011, doi: 10.1002/polb.22169.

[6] K.-I. Jang *et al.*, «Self-assembled three dimensional network designs for soft electronics», *Nat. Commun.*, vol. 8, n. 1, p. 15894, Jun. 2017, doi: 10.1038/ncomms15894.

[7] Y. Kim and S. Lim, «Low Loss Substrate-Integrated Waveguide Using 3D-Printed Non-Uniform Honeycomb-Shaped Material,» in *IEEE Access*, vol. 8, pp. 191090-191099, 2020, doi: 10.1109/ACCESS.2020.3032132.

[8] Fortify, «3D Printed Dielectric Lenses increase antenna gain and widen beam scanning angle», [Online]. https://www.microwavejournal.com/articles/36375-d-printed-dielectric-lenses-increase-antenna-gain-and-widen-beam-scanning-angle

[9] P. Njogu, B. Sanz-Izquierdo, A. Elibiary, S. Y. Jun, Z. Chen, and D. Bird, «3D Printed Fingernail Antennas for 5G Applications», *IEEE Access*, vol. 8, pp. 228711–228719, 2020, doi: 10.1109/ACCESS.2020.3043045.

[10] S. Xu *et al.*, «Stretchable batteries with self-similar serpentine interconnects and integrated wireless recharging systems», *Nat. Commun.*, vol. 4, n. 1, p. 1543, Feb. 2013, doi: 10.1038/ncomms2553.

[11] E. McGlynn *et al.*, «The Future of Neuroscience: Flexible and Wireless Implantable Neural Electronics», *Adv. Sci.*, vol. 8, p. 2002693, May 2021, doi: 10.1002/advs.202002693.

[12] J. Huang, Y. Zhou, Z. Ning, and H. Gharavi, «Wireless Power Transfer and Energy Harvesting: Current Status and Future Prospects», *IEEE Wirel. Commun.*, vol. 26, n. 4, pp. 163–169, 2019, doi: 10.1109/MWC.2019.1800378.

[13] Wikipedia, [Online]. https://en.wikipedia.org/wiki/Near_and_far_field

[14] X. Huang *et al.*, «Epidermal radio frequency electronics for wireless power transfer», *Microsyst. Nanoeng.*, vol. 2, n. 1, p. 16052, Oct. 2016, doi: 10.1038/micronano.2016.52.

[15] S. I. Park *et al.*, «Soft, stretchable, fully implantable miniaturized optoelectronic systems for wireless optogenetics», *Nat. Biotechnol.*, vol. 33, n. 12, pp. 1280–1286, Dec. 2015, doi: 10.1038/nbt.3415.

[16] K. W. Choi *et al.*, «Simultaneous Wireless Information and Power Transfer (SWIPT) for Internet of Things: Novel Receiver Design and Experimental Validation», *IEEE Internet Things J.*, vol. 7, n. 4, pp. 2996–3012, 2020, doi: 10.1109/JIOT.2020.2964302.

[17] G. Paolini, M. Feliciani, D. Masotti, and A. Costanzo, «Toward an Energy-Autonomous Wearable System for Human Breath Detection», in *2020 IEEE MTT-S International Microwave Biomedical Conference (IMBioC)*, 2020, pp. 1–3. doi: 10.1109/IMBIoC47321.2020.9385027.

[18] L. Adey, [Online]. https://eacpds.com/formlabs-form-3-form-3l-answers-to-your-faqs/.

[19] G. Battistini, G. Paolini, D. Masotti, and A. Costanzo, «3-D Etching Techniques for Low-Cost Wearable Microwave Devices in Grounded Coplanar Waveguide», submitted at *IMBioC 2022,* May 2022.

[20] G. Battistini, G. Paolini, D. Masotti, and A. Costanzo, «Innovative 3-D Printing Processing Techniques for Flexible and Wearable Planar Rectennas», submitted at *WPTC 2022*, Jul. 2022.

[21] V.Rizzoli, A. Lipparini, «*Propagazione Elettromagnetica Guidata (Parte seconda)»,* Esculapio.

[22] D. M. Pozar, «*Microwave Engineering»*, 4th Edition. John Wiley & Sons, Inc., 2012.

[23] M. Steer, «*Microwave and RF Design II - Transmission Lines»,* North Carolina State University.

[24] E. Bartoletti, «Caratterizzazione sperimentale delle proprietà elettromagnetiche di materiali plastici mediante metodi risonanti» Master degree thesis, 2012-2013.

[25] S. Maurya and V. V. Nagar, «An Extensive Study, Design And Simulation Of Mems Guided Media: Microstrip Line», *Int. J. Smart Sens. Intell. Syst.*, vol. 3, pp. 88–93, 2010.

[26] Rainee N. Simons, «*Coplanar Waveguide Circuits, Components, and Systems»,* John Wiley & Sons, Inc., 2001.

[27] N. I. Dib and L. P. B. Katehi, «Theoretical characterization of coplanar waveguide transmission lines and discontinuities», 1992.

[28] I. Rosu, «Microstrip, Stripline, CPW, and SIW Design» [Online]. https://www.qsl.net/va3iul/Microstrip_Stripline_CPW_Design/Microstrip_Stripline_and_CPW_Design.pdf

[29] J. Coonrod, «Comparing Microstrip and Grounded Coplanar Waveguide», [Online].

https://www.microwavejournal.com/blogs/1-rog-blog/post/24374-comparing-microstrip-and-grounded-coplanar-waveguide

[30] B. C. Wadell, *«Transmission line design handbook»,* Artech House, 1991.

[31] V. Rizzoli, «Resonance Measurement of Single- and Coupled-Microstrip Propagation Constants », *IEEE Transactions on Microwave Theory and Techniques*, vol. 25, no. 2, pp. 113-120, Feb. 1977.

[32] K.-P. Latti, M. Kettunen, J. Strom, and P. Silventoinen, «A Review of Microstrip T-Resonator Method in Determining the Dielectric Properties of Printed Circuit Board Materials», in *IEEE Transactions on Instrumentation and Measurement*, vol. 56, no. 5, pp. 1845-1850, Oct. 2007.

[33] K. J. Herrick, T. A. Schwarz, and L. P. B. Katehi, «Si-micromachined coplanar waveguides for use in high-frequency circuits», in *IEEE Transactions on Microwave Theory and Techniques*, vol. 46, no. 6, pp. 762-768, Jun. 1998.

[34] CST Microwave Studio, [Online]. https://space.mit.edu/RADIO/CST_online/mergedProjects/3D/special_postpr/special_postpr_pp_farfield.htm

[35] CST Microwave Studio, [Online]. https://space.mit.edu/RADIO/CST_online/mergedProjects/3D/special_postpr/special_postpr_power_view.htm

[36] K. F. Tong, K. Li, T. Matsui, and M. Izutsu, «Broad-band double-layered coplanar patch antennas with adjustable CPW feeding structure», in *IEEE Transactions on Antennas and Propagation*, vol. 52, no. 11, pp. 3153-3156, Nov. 2004, doi: 10.1109/TAP.2004.834392.

[37] K. Li, C. H. Cheng, T. Matsui, and M. Izutsu, «Coplanar patch antennas: principle, simulation and experiment», *IEEE Antennas and Propagation Society International Symposium*. 2001 Digest. Held in conjunction with: *USNC/URSI National Radio Science Meeting* (Cat. No.01CH37229), 2001, pp. 402-405 vol.3, doi: 10.1109/APS.2001.960119.

[38] S. Ladan, A. B. Guntupalli, and K. Wu, «A High-Efficiency 24 GHz Rectenna Development Towards Millimeter-Wave Energy Harvesting and Wireless Power Transmission», in *IEEE Transactions on Circuits and Systems I: Regular Papers*, vol. 61, no. 12, pp. 3358-3366, Dec. 2014, doi: 10.1109/TCSI.2014.2338616.

[39] H.Visser, S. Keyrouz, and A. Smolders, «Optimized rectenna design». Wireless Power Transfer, 2015, 2(1), pp. 44-50. doi:10.1017/wpt.2014.14.

[40] M. Stoopman, S. Keyrouz, H. J. Visser, K. Philips, and W. A. Serdijn, «Co-Design of a CMOS Rectifier and Small Loop Antenna for Highly Sensitive RF Energy Harvesters», in *IEEE Journal of Solid-State Circuits*, vol. 49, no. 3, pp. 622-634, March 2014, doi:

10.1109/JSSC.2014.2302793.

[41] T. S. Almoneef, «Design of a Rectenna Array Without a Matching Network», in *IEEE Access*, vol. 8, pp. 109071-109079, 2020, doi: 10.1109/ACCESS.2020.3001903.

[42][Online]. http://edadownload.software.keysight.com/eedl/ads/2011_01/pdf/adshbapp.pdf

[43] R. E. Collin, «Limitations of the Thevenin and Norton equivalent circuits for a receiving antenna», *IEEE Antennas Propag. Mag.*, vol. 45, n. 2, pp. 119–124, 2003, doi: 10.1109/MAP.2003.1203128.

[44] A. W. Love, «Comment on the equivalent circuit of a receiving antenna», *IEEE Antennas Propag. Mag.*, vol. 44, n. 5, pp. 124–125, 2002, doi: 10.1109/MAP.2002.1077791.

[45] M. A. C. Niamien, S. Collardey, and K. Mahdjoubi, «A Hybrid Approach for Receiving Antennas: Concepts and Applications», *IEEE Trans. Antennas Propag.*, vol. 62, n. 11, pp. 5462–5473, 2014, doi: 10.1109/TAP.2014.2355852.

[46] H. Li, X. Lin, B. K. Lau, and S. He, «Equivalent Circuit Based Calculation of Signal Correlation in Lossy MIMO Antennas», *IEEE Trans. Antennas Propag.*, vol. 61, n. 10, pp. 5214–5222, 2013, doi: 10.1109/TAP.2013.2273212.

[47] C. A. Balanis, «*Antenna Theory Analysis and Design*», Third Edition. Wiley, 2005.

[48] S. Silver, «*Microwave Antenna Theory and Design*», First edition. McGraw Hill Book Company, 1949.